行政院國家科學委員會專題研究計畫 成果報告

寬頻合作式無線多輸出入通訊系統--子計畫三：合作式多輸出入無線通訊之上行傳收器訊號處理技術研究(2/2)
研究成果報告(完整版)

計 畫 類 別 ： 整合型
計 畫 編 號 ： NSC 99-2219-E-009-010-
執 行 期 間 ： 99 年 08 月 01 日至 100 年 07 月 31 日
執 行 單 位 ： 國立交通大學電子工程學系及電子研究所

計 畫 主 持 人 ： 林大衛

計畫參與人員： 碩士班研究生-兼任助理人員：柯俊言
碩士班研究生-兼任助理人員：張智凱
碩士班研究生-兼任助理人員：陳威宇
碩士班研究生-兼任助理人員：詹曉盈
碩士班研究生-兼任助理人員：余卓翰
碩士班研究生-兼任助理人員：李政憲
碩士班研究生-兼任助理人員：尤基峰
碩士班研究生-兼任助理人員：強丹
博士班研究生-兼任助理人員：王海薇
博士班研究生-兼任助理人員：王柏森

報 告 附 件 ： 出席國際會議研究心得報告及發表論文

處 理 方 式 ： 本計畫涉及專利或其他智慧財產權，2 年後可公開查詢

中 華 民 國 100 年 10 月 14 日

行政院國家科學委員會補助專題研究計畫成果報告

合作式多輸出入無線通訊之上行傳收器訊號處理技術研究(2/2)

Uplink Transceiver Signal Processing Technology for Cooperative MIMO Wireless Communication (2/2)

計畫編號：NSC 99-2219-E-009-010
執行期限：99 年 8 月 1 日至 100 年 7 月 31 日
主持人：林大衛 交通大學電子工程學系 教授
計畫參與人員：王海薇、王柏森、柯俊言、張智凱、余卓翰、陳威宇、詹曉盈
李政憲、尤基峰、Chandan Jha 交通大學電子工程學系 研究生

摘要

本計畫為一整合型計畫之子計畫，研究無線通訊之傳輸訊號處理技術。研究內容分為兩大部份：一為演算法研究，一為數位訊號處理器(DSP)軟體實現研究。其中的研究子題含：雙向中繼傳輸技術研究、IEEE 802.16m 上行測距技術研究、IEEE 802.16m 多輸出入傳收技術研究、IEEE 802.16m 初始下行同步技術之數位訊號處理器軟體實現、以及 IEEE 802.16m 通道估計技術之數位訊號處理器軟體實現。以上前三子題屬演算法研究，後二子題則係數位訊號處理器軟體實現之研究。

在中繼技術方面，我們探討了一種雙向中繼傳輸方法，等效於可以讓較弱的傳送端分享較強之傳送端的傳輸功率。在 IEEE 802.16m 上行測距技術方面，我們研究了其相關規格、演算法與效能。在 IEEE 802.16m 多輸出入傳收技術方面，我們亦研究了其相關規格、演算法與效能。在 IEEE 802.16m 初始下行同步技術以及 IEEE 802.16m 通道估計技術之數位訊號處理器軟體實現方面，則係根據我們過去之演算法研究成果，將其以定點運算方式實現於數位訊號處理器上，並作程式之優化，以利其執行速度。

關鍵詞：正交分頻多重進接、正交分頻多工、中繼、測距、多輸出入、同步、通道估計

Abstract

This project is a subproject of an integrated project. Its does research in transmission signal processing technologies for wireless communication. The research conducted in this project can be divided broadly into two parts: algorithm research and digital signal processor (DSP) software implementation research. The topics addressed include bidirectional relaying techniques, IEEE 802.16 uplink ranging techniques, IEEE 802.16m multi-input multi-output (MIMO) transmission techniques, DSP software implementation of IEEE 802.16m initial downlink synchronization technique, and DSP software implementation of IEEE 802.16m channel estimation technique. Of these topics, the first three pertain to algorithm research and the last two pertain to DSP software implementation research.

Concerning relaying techniques, we study a bidirectional relaying method which can, effectively, let the weaker transmitter share the transmission power of the stronger transmitter. In IEEE 802.16m uplink ranging techniques, we study the corresponding specifications, algorithms, and performance. In IEEE 802.16m MIMO transmission techniques, we also study the corresponding specifications, algorithms, and performance. In DSP software implementation of IEEE 802.16m initial synchronization technique and IEEE 802.16 channel estimation technique, we base the work on our past algorithm research results. The DSP implementation employs fixed-point computation and we also conduct code optimization, both for the benefit of execution speed.

Keywords: Orthogonal Frequency-Division Multiple Access (OFDMA), Orthogonal Frequency-Division Multiplexing (OFDM), Relay, Ranging, Multi-input Multi-output (MIMO), Synchronization, Channel Estimation

目錄 Table of Contents

一、計畫與報告簡介

無線通訊技術本就不斷發展，但自從國際電信聯盟射頻通訊標準部門(ITU-R)於幾年前公布其制定第四代(4G)行動通訊標準 IMT-Advanced 的計畫後，更引發一波相關的研發浪潮。許多公司與機構都意圖在此一標準中取得一席之地。但由於行動通訊系統高度複雜，所以這些公司與機構係透過組成團隊的方式來參與 IMT-Advanced 標準研發。此其中兩個主要的標準團隊就是 IEEE 802.16m 工作團(task group)和第三代行動通訊夥伴計畫(3GPP)先進長程發展(LTE-Advanced)團體。以空氣介面系統而言，幾個主要且被這些團隊所積極發展的技術包括：各型多輸出入(multi-input multi-output, MIMO)傳輸技術、極微細胞(femtocell)系統技術、以及中繼(relay)系統技術。其中底層的調變方式皆基於正交分頻多工(orthogonal frequency-division multiplexing, OFDM)型式的技術，含正交分頻多重進接(orthogonal frequency-division multiple access, OFDMA)和單載波分頻多重進接(single-carrier frequency-division multiple access, SC-FDMA)。

本計畫為一整合型計畫之子計畫，旨在研究無線通訊之傳輸訊號處理技術。其細部研究內容的規劃，係本於一個思維，即：立足近期標準相關之技術，放眼未來可能之發展。說明如下。先參 Fig. 1-1，其中所示係根據目前技術發展趨勢，所設想未來無線傳輸系統之可能環境架構。圖中 BS、RS、與 MS 之間的雙箭頭連線表示無線通道。實際上，視 BS、RS、與 MS 的相對位置，MS 也可以不經 RS 而直接連上 BS(這也就是目前行動通訊系統的一般架構，是故此示意圖可說亦涵蓋目前的行動通訊系統架構)。但一方面這樣的情況比圖中所示者單純，二方面若也顯示直接連接的情況，會使示意圖太複雜。所以我們只顯示 MS 經 RS 連上 BS 的情況。此系統最複雜的運作情境，是各 BS、各 RS、和各 MS 都可以有多支天線，而多個 BS 可以同時向多個 RS 傳送訊號(即 downlink multiuser MIMO 加上 downlink coordinated multi-point [CoMP])或同時接收從多個 RS 傳來的訊號(即 uplink multiuser MIMO 加上 uplink CoMP)，且多個 RS 也可以同時向多個 MS 同時傳送訊號或同時接收從多個 MS 傳來的訊號。若是 RS 具有雙向傳收功能(即 bidirectional RS 或 two-way RS)，則各 BS 和各 MS 又可以同時向各 RS 傳送訊號，而各 RS 也可以同時向各 BS 和各 MS 傳送訊號。然而以上最複雜的運作情境，在目前只是一個長程的研究方向，預期還要不少年以後才會趨於實用。較短期內可以實用化的運作情境，應該比此最複雜的情境要簡單。

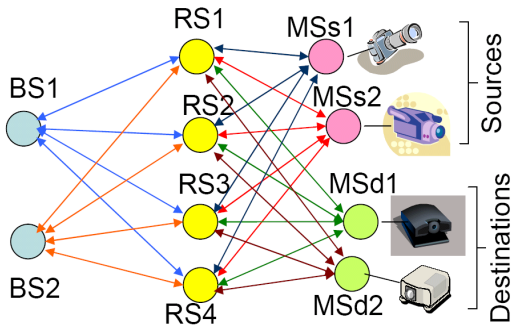

Fig. 1-1. 傳輸環境架構示意圖，其中 BS = base station, RS = relay station, MS = mobile station。

上述具有雙向傳收功能的中繼技術，是最近幾年的新發展，其中有許多可以研發的課題。在本計畫中我們做了些探討。我們發現一項有趣的中繼訊號處理方式，可以讓較弱的傳送端虛擬分享較強的傳送端的傳輸功率。這類技術可說還在初起階段，尚未成為國際標準組織所討論的技術。

在標準相關技術方面，基於過去我們自己在 IEEE 802.16/WiMAX 方面的研究成果，以及近幾年我國在 WiMAX 和後續 IEEE 802.16m/Advanced WiMAX 標準制定方面的大力投入，本計畫以 IEEE 802.16m 為基礎進行研究。其研究內容可分兩大部份：一是演算法研究，一是數位訊號處理器(DSP)軟體實現研究。在演算法方面，本計畫探討了 IEEE 802.16m 的上行測距技術和多輸出入傳收技術，其中我們研究了 IEEE 802.16m 相關於測距和多輸出入傳收的規格，設計了相關演算法，並以計算機模擬語數學分析研究其效能。在數位訊號處理器軟體實現研究方面，我們則進行了 IEEE 802.16m 初始下行同步技術和通道估計技術之數位訊號處理器軟體實現。這些實現係根據我們之前的演算法研究成果，將其以定點運算方式實現於數位訊號處理器上，並作程式之優化，以利其執行速度。

本計畫為一個二年期計畫的第二年，本報告旨在說明第二年計畫之成果。但在此我們且用一小段的篇幅，概述兩年的整體研究方向與技術性成果。整體而言，本計畫較側重上行傳收技術，但亦進行一些下行傳收技術的研究。第一年的研究與成果包括寬頻無線通道模型之探討、峰均功率比(peak-to-average power ratio, PAPR)控制技術研究、分散式中繼網路之功率分配技術研究、及載波間干擾(intercarrier interference, ICI)抑制技術研究等。此外亦開始進行雙向中繼技術研究與上行測距技術研究。第二年(本年)的研究與成果則如前述，包括雙向中繼技術研究、上行測距技術研究、多輸出入傳收技術研究、初始下行同步技術之數位訊號處理器軟體實現研究、及通道估計技術之數位訊號處理器軟體實現研究等。

以下我們分節討論本年度在各技術課題上的研究。第二節討論雙向中繼技術。第三節討論 IEEE 802.16m 上行測距技術。第四節討論 IEEE 802.16m 多輸出入傳收技術。第五節討論IEEE 802.16m初始下行同步技術之數位訊號處理器實現。第六節討論IEEE 802.16m 通道估計技術之數位訊號處理器實現。為行文方便，第二節至第六節主要使用英文。第七節為本報告之參考文獻。第八節為計畫成果自評。

二、雙向中繼技術研究

本節主要內容自下頁起，以學術論文初稿方式呈現。我們將在未來繼續進行相關研究。

Virtual Sharing of Signal Power via Fold-and-Forward Two-Way Relaying

Preliminary Draft

***Abstract*—We consider a two-way relay system where the two terminal nodes may transmit signals to the relay simultaneously. The relay "folds" the received sum signal and broadcasts the result to both terminals for detection. We show that, with asymmetric channel conditions between the two terminal-relay links, the above operation can tip the error performance between the two directions of transmission in a way that can be viewed as effecting virtual sharing of the transmitter power of the better-conditioned terminal by the worse-conditioned. This property also has implication in transmission between terminals that are subject to unequal power constraints.**

***Index Terms*—Amplify-and-forward, physical-layer network coding, two-way relay.**

I. Introduction

There is much recent interest in applying the concept of network coding to relay-assisted wireless communication. Such coding permits simultaneous reception or transmission of multiple signals at the relay, thereby significantly enhancing the bandwidth efficiency. Some overviews can be found in [1], [2]. One typical structure of such systems is illustrated in Fig. 1, where two terminal nodes T0 and T1 (which have no direct link between them) send signals to each other via the help of the relay node R.

Various network coding methods have been proposed for two-way relaying, some operating in the digital signal domain and requiring the relay to perform some sort of demodulation and some operating in the analog signal domain. Of the latter kind, the simplest merely asks the relay to amplify and broadcast the received sum signal [1]–[4]. Each terminal node can then retrieve the signal destined to it by subtracting a copy of its own transmitted signal from the received broadcast signal, an operation to some extent resembling decision-feedback equalization. While being referred to as a kind of physical network coding, this simple amplify-and-forward (AF) approach deviates from the original XOR network coding [1], [2], [5], [6] in one key aspect. That is, the XOR operation in the original network coding keeps the alphabet size binary whereas AF may double the peak signal amplitude (equivalent to doubling the alphabet size in some sense); the latter could mean 3 dB loss in power efficiency [2]. Note that it is the modulo addition nature of XOR that keeps the alphabet size in the original network coding from expansion. However, to generalize this modulo concept to nonbinary modulations and arbitrary channel conditions is highly nonstraightforward. Some studies in related veins are [7]–[10].

This work was supported by the Wireless Broadband Communications Technology and Application Project of the Institute for Information Industry which was subsidized by the Ministry of Economic Affairs of the Republic of China as well as by the National Science Council of R.O.C. under Grant NSC 99-2219-E-009-010.

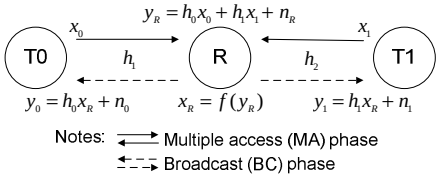

Fig. 1. System structure, where signal transmission between terminal nodes T1 and T2 is carried out in two phases.

A recent work [11] proposes to have the relay forward the absolute value of its received signal after suitable level-shifting and scaling. It is shown that under fixed channels, this can improve the overall error performance. Since taking the absolute value of a signal can be viewed as a way of "folding" the range of possible signal values (which is also what a modulo operation does), we term the technique fold-and-forward (FF) to allow for later generalization. In this letter, we shed new lights on the analysis and design of this relaying technique. In one aspect, we show that, in two-way relaying, FF can tip the error performance in the two directions of transmission in a way that can be viewed as effecting virtual sharing of the transmitter power of the better conditioned terminal by the worse conditioned. This property can have interesting implications when the two terminals are subject to unequal power constraints or asymmetric channel conditions, such as that between a base station and a mobile station.

In what follows, Sec. II introduces the system model. Sec. III discusses the case where both terminals transmit binary signals. Sec. IV considers the case of higher-order modulations. And Sec. V is the conclusion.

II. System Model

Consider the two-way relay system shown in Fig. 1, where x_i $(i = 0, 1)$ is the signal transmitted by Ti, h_i is the channel coefficient between Ti and R, and n_i is the additive receiver noise at Ti. In the multiple access (MA) phase the relay receives the signal

$$y_R = h_0x_0 + h_1x_1 + n_R \tag{1}$$

where n_R is the additive noise at the relay. We assume that both channel coefficients are known to all three nodes.

While the system can handle complex signals and complex channel coefficients, due to space limit we only treat the case of real x_i and h_i here. Hence let x_i be an M_i-PAM signal with $x_i \in \{\pm 1, \pm 3, ..., \pm(M_i - 1)\}$, and we refer to the overall

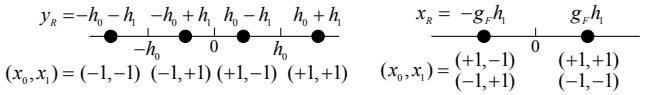

Fig. 2. Noiseless received and transmitted relay signal constellations for (2,2)-PAM and the corresponding source signal pairs.

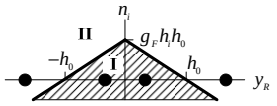

Fig. 3. Effective decision boundaries and error regions for (2,2)-PAM under FF for terminal Ti, $i = 0, 1$.

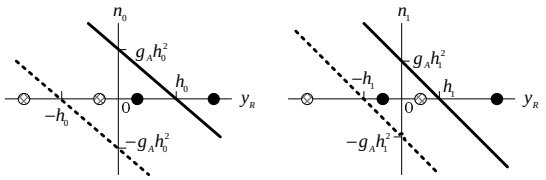

Fig. 4. Effective decision boundaries for (2,2)-PAM under AF at terminals T0 (left) and T1 (right).

modulation as (M_0, M_1)-PAM. Without loss of generality, assume $h_0 \geq h_1 > 0$. And define $h = h_1/h_0$. In the broadcast (BC) phase, relay R broadcasts the folded signal $x_R = f(y_R)$ to T0 and T1. The folding operation and the detection methods at the terminal nodes are described further later.

III. Case with (2,2)-PAM

In the (2,2)-PAM case, we have $x_0, x_1 \in \{+1, -1\}$. In absence of relay noise, the y_R constellation consists of either 3 or 4 points, depending on whether $h = 1$ or $h < 1$. We concentrate on the latter condition as the former can be considered an asymptotic case of it. The four noiseless received signal points at the relay are given by $\pm h_0 \pm h_1$. Let the FF operation be given by (similar to [11])

$$f(y_R) = g_F(|y_R| - h_0) \tag{2}$$

where g_F is a scaling factor to satisfy any transmission power constraint of the relay and the subtraction of h_0 is to make x_R approximately zero-mean. The exact relation between g_F and the relay transmission power will be given later.

The noiseless constellations of y_R and x_R are illustrated in Fig. 2, together with the corresponding source signal pairs (x_0, x_1). The constellation for x_R satisfies the "exclusive law" [8], [9]; that is, given x_0 (resp. x_1), different values of x_1 (resp. x_0) are mapped to different constellation points. Hence both terminals can determine the other party's transmission unambiguously from the received BC signal of the relay, if there is no noise. The detection method (in noise) at terminal Ti ($i = 0, 1$) is given by

$$\hat{x}_{\bar{i}} = \begin{cases} \text{sgn}(y_i), & \text{if } x_i > 0, \\ -\text{sgn}(y_i), & \text{otherwise}, \end{cases} \tag{3}$$

where $\hat{x}_{\bar{i}}$ is the detected signal at Ti, with $\bar{0} = 1$ and $\bar{1} = 0$, and $\text{sgn}(\cdot)$ is the signum function with $\text{sgn}(0) \triangleq 1$.

A. Error Performance

For simplicity, assume that n_0, n_1, and n_R are white Gaussian (AWGN) with equal variance σ_n^2. Because the received signal at either terminal contains two AWGN components, it turns out that the effective decision boundaries and error regions for Ti can be conveniently depicted in a two-dimensional plot as shown in Fig. 3, where the four black dots indicate the noiseless received signal constellation at the relay. In the figure, region I (shaded) applies to the error of having $\hat{x}_{\bar{i}} = -x_i$ when $x_{\bar{i}} = x_i$, and region II that of having $\hat{x}_{\bar{i}} = x_i$ when $x_{\bar{i}} = -x_i$. (The decision boundary is the same for all four signal points.) In contrast, the effective decision boundaries under plain AF are as shown in Fig. 4, where g_A is the relay amplification factor under AF. For either T0 or T1, the thick solid line (resp. dashed line) indicates the boundary when the local transmitter emitted a $+1$ (resp. -1) in the MA phase. For clarity, signal points associated with the solid-line boundaries are indicated using solid dots, whereas those associated with the dashed-line boundaries are indicated using cross-hatched dots.

The qualitative difference in performance between FF and AF can be gleaned without going to detailed mathematics by comparing Figs. 3 and 4. For this, note that, in high signal-to-noise ratio (SNR), the error probability of each signal point is primarily determined by its distance to the nearest decision boundary. For the sake of argument, let $g_F = g_A$ for now. Then, by comparing Fig. 3 with the left plot in Fig. 4, we see that the detection error probabilities at T0 (for signals transmitted from T1) under both forwarding schemes are similar. But they are different at T1 (compare Fig. 3 with the right plot in Fig. 4), with AF claiming advantage over FF because the former has a larger distance between each signal point and its associated decision boundary. However, if the relay is power-limited rather than gain-limited, then we can have $g_F > g_A$ because FF has a smaller relay signal constellation than AF (see Fig. 2). Then the relative performance of FF with respect to AF improves. In particular, FF yields a better performance than AF at T0 by effecting a larger distance between each signal point and its corresponding decision boundary. At T1, the relative performance of FF also improves, but in many conditions (details omitted) still lags that of AF. Compared to AF, therefore, FF may be viewed in some sense as virtually robbing the detection performance of T0 signals (which are detected at T1) in favor of T1 signals (which are detected at T0). Thus the title of this letter.

Employing the formulation proposed in [12], we obtain the bit error rate (BER) under FF at Ti (for signals from T$\bar{i}$) as

$$P_i^F = \frac{1}{2}(P_i^I + P_i^{II}) \tag{4}$$

with

$$P_i^I = \frac{1}{2\pi}\int_0^{\pi-(\phi_i^I-\phi_i)} e^{-\frac{\gamma_i(h_1)}{2\sin^2\theta}}\,d\theta - \frac{1}{2\pi}\int_0^{\pi-(\phi_i^I+\phi_i)} e^{-\frac{\gamma_i(2h_0+h_1)}{2\sin^2\theta}}\,d\theta \tag{5}$$

and

$$P_i^{II} = \frac{1}{2\pi}\int_0^{\pi-(\phi_i-\phi_i^{II})} e^{-\frac{\gamma_i(h_1)}{2\sin^2\theta}}\,d\theta + \frac{1}{2\pi}\int_0^{\pi-(\phi_i+\phi_i^{II})} e^{-\frac{\gamma_i(2h_0-h_1)}{2\sin^2\theta}}\,d\theta, \quad (6)$$

where P_i^I and P_i^{II} stand for, respectively, probability of declaring $x_{\bar{i}} = -x_i$ when $x_{\bar{i}} = x_i$ and that of declaring $x_{\bar{i}} = x_i$ when $x_{\bar{i}} = -x_i$, and

$$\gamma_i(z) = \frac{z^2(g_F h_i)^2}{[1+(g_F h_i)^2]\sigma_n^2},\ \phi_i = \arctan\frac{1}{g_F h_i}, \quad (7)$$

$$\phi_i^I = \arctan\frac{h_0+h_1}{g_F h_i h_0},\ \phi_i^{II} = \arctan\frac{h_0-h_1}{g_F h_i h_0}. \quad (8)$$

From the geometry shown in Fig. 3, we can also see that, in high SNR,

$$P_i^F \approx Q\left(\frac{h_1(g_F h_i)}{\sqrt{1+(g_F h_i)^2}\,\sigma_n}\right) \quad (9)$$

where $Q(\cdot)$ is the Gaussian Q function. In any case, P_i^F is upper-bounded by two times the Q function value above. On the other hand, the BER at Ti under AF is given by

$$P_i^A = Q\left(\frac{h_{\bar{i}}(g_A h_i)}{\sqrt{1+(g_A h_i)^2}\,\sigma_n}\right). \quad (10)$$

Comparing (9) with (10), we see that at T0, it may only take a slightly greater g_F than g_A to make FF perform better than AF. At T1, some algebra will show that, depending on the relation among h_0, h_1, and g_A, it may or may not be possible to make FF perform better than AF. As to the exact values of g_A and g_F, suppose the relay is subject to a transmission power constraint P_R. Then the maximum allowed gains are given by, respectively,

$$g_A = \sqrt{P_R/E[y_R^2]},\quad g_F = \sqrt{P_R/E[(|y_R|-h_0)^2]}. \quad (11)$$

With some algebra, it can be shown that

$$E[y_R^2] = h_0^2 + h_1^2 + \sigma_n^2, \quad (12)$$

$$\begin{aligned} E[(|y_R|-h_0)^2] &= h_1^2+\sigma_n^2 + 2h_0\left[(h_0+h_1)Q\left(\frac{h_0+h_1}{\sigma_n}\right)\right. \\ &\quad \left.+(h_0-h_1)Q\left(\frac{h_0-h_1}{\sigma_n}\right)\right] \\ &\quad -h_0\sigma_n\sqrt{\frac{2}{\pi}}\left[e^{-\frac{(h_0+h_1)^2}{2\sigma_n^2}}+e^{-\frac{(h_0-h_1)^2}{2\sigma_n^2}}\right]. \end{aligned} \quad (13)$$

As a numerical example, consider a case where $h_0 = 1$, $h_1 = 0.5$, and $P_R = 1$. Fig. 5 shows the BER performance. Theory and simulation results agree well. And the results show clearly that, in comparison to AF, FF significantly raises the detection performance of T1 signals (detected at T0) at the expense of the detection performance of T0 signals (detected at T1). Averaged over the two, FF performs slightly better than AF towards the higher-SNR end, in this example.

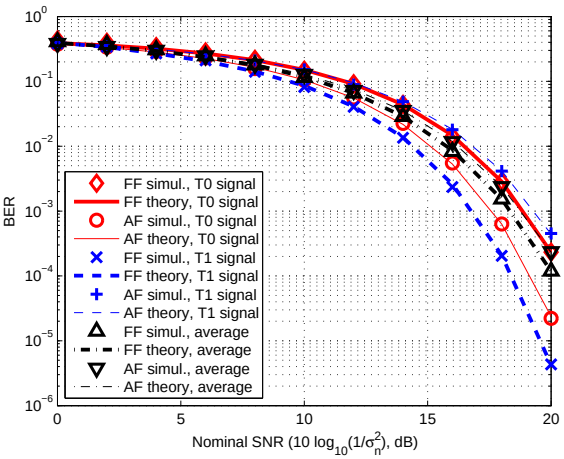

Fig. 5. BER performance with (2,2)-PAM in AWGN at $h_0 = 1$, $h_1 = 0.5$, and $P_R = 1$.

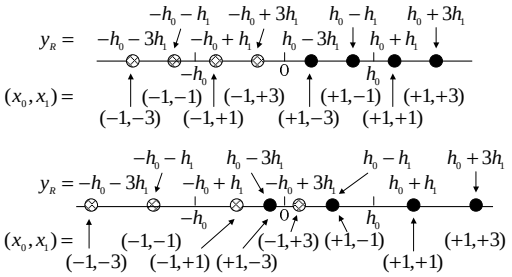

Fig. 6. Two kinds of noiseless relay received signal constellation under (2,4)-PAM. Top: separable; bottom: interwoven.

IV. Case with Higher-Order Modulations

With higher-order modulations, we need to distinguish between two conditions regarding the noiseless received signal constellation at the relay: *separable* and *interwoven*. To see what they are, note that, under (M_0, M_1)-PAM, this noiseless constellation is a "product constellation" of $M_0 M_1$ points. (The points may not be all distinct.) The product constellation may be divided into M_0 subconstellations, each associated with a possible T0 signal value, or M_1 subconstellations, each associated with a possible T1 signal value. Each of the above M_0 (resp. M_1) subconstellations contains signal values in the range $R_k^{(0)} = [kh_0 - (M_1-1)h_1, kh_0 + (M_1-1)h_1]$ (resp. $R_k^{(1)} = [kh_1 - (M_0-1)h_0, kh_1 + (M_0-1)h_0]$), where $k \in \{\pm1, \pm3, \ldots, \pm(M_0-1)\}$ (resp. $k \in \{\pm1, \pm3, \ldots, \pm(M_1-1)\}$). The *separable* case refers to the situation where either any two such $R_k^{(0)}$ have at most one point in common or any two such $R_k^{(1)}$ have at most one point in common. (Such common points, if any, are end points of some ranges.) Otherwise, the constellation is *interwoven*. Fig. 6 illustrates the two conditions for (2,4)-PAM with $h < 1$. For clarity, we distinguish the two M_0 subconstellations in each condition using solid dots and cross-hatched dots.

To address the interwoven condition would take much space. Hence we only treat the separable case, which amounts to assuming that $h \le 1/(M_1-1)$. In this case, we can fold the product constellation into $\max(M_0, M_1)$ points while

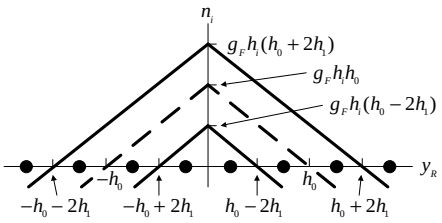

Fig. 7. Effective decision boundaries for (2,4)-PAM under FF at terminals T1 (thick dashed line) and T0 (all three thick solid and dashed lines).

satisfying the exclusive law so that colocated points are associated with uniquely distinguishable signals at the terminals [8], [9]. In fact, more than one workable folding method can be conceived. Space precludes a detailed discussion. However, for $(2, M_1)$-PAM the method in (2) suffices. And the noiseless transmitted signal constellation of the relay is given by $\{kg_F h_1 | k = \pm 1, \pm 3, \ldots, \ldots \pm (M_1 - 1)\}$. The detection method at T1 can be the same as in (3) and that at T0 can be

$$\hat{x}_1 = \begin{cases} \min(-3, \max(3, \hat{x}_1^a)), & \text{if } x_0 > 0, \\ \min(-3, \max(3, -\hat{x}_1^a)), & \text{otherwise,} \end{cases} \tag{14}$$

where

$$\hat{x}_1^a = 2 \cdot \lceil y_1/(2g_F h_1^2) \rceil - 1, \tag{15}$$

with $\lceil\ \rceil$ being the ceiling function.

To illustrate the resulting performance, consider (2,4)-PAM with the FF operation as given in (2). Then the effective decision boundaries under FF are as shown in Fig. 7. Hence, in high SNR, the symbol error rate (SER) at Ti $(i = 0, 1)$ (for signals from T$\bar{i}$) under FF is approximately given by

$$P_i^F = K_i^F\, Q\left(\frac{h_1(g_F h_i)}{\sqrt{1 + (g_F h_i)^2}\,\sigma_n}\right) \tag{16}$$

where $K_0^F = 1.5$ and $K_1^F = 0.5$. In contrast, that under AF is approximately given by

$$P_i^A = K_i^A\, Q\left(\frac{h_{\bar{i}}(g_A h_i)}{\sqrt{1 + (g_A h_i)^2}\,\sigma_n}\right) \tag{17}$$

where $K_0^A = 1.5$ and $K_1^A = 1$. We omit detailed derivation as well as the expressions for the exact SER due to their length. Nevertheless, we note that, for $i = 1$, the equality in (17) is exact because T0 signals are binary.

Fig. 8 shows the SER performance for the condition $h_0 = 1$, $h_1 = 0.33$, and $P_R = 1$. Again, theory and simulation results agree well. And, in comparison to AF, FF again improves significantly the detection performance of T1 signals (detected at T0) at the expense of the detection performance of T0 signals (detected at T1), as discussed.

V. Conclusion

We studied the FF technique for two-way relaying. We showed that, in asymmetric channel conditions, FF could tip the error performance in a way that appeared like letting the worse-conditioned terminal share the transmitter power of the better-conditioned terminal virtually. Similar can be said for the case where the two terminals are subject to unequal transmitter power constraints.

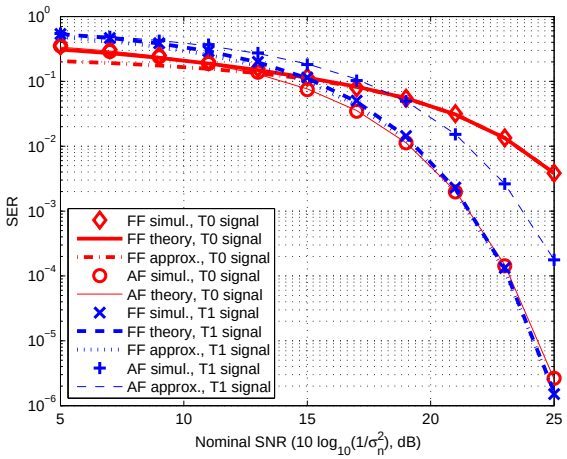

Fig. 8. SER performance with (2,4)-PAM in AWGN at $h_0 = 1$, $h_1 = 0.33$, and $P_R = 1$. Curves marked "theory" give exact theoretical values, although their expressions under FF are omitted in this letter.

References

[1] K. M. Josiam, Y.-H. Nam, and F. Khan, "Intelligent coding in relays," *IEEE Veh. Tech. Mag.*, vol. 4, no. 1, pp. 27–33, Mar. 2009.

[2] F. Rosetto and M. Zorzi, "Mixing network coding and cooperation for reliable wireless communications," *IEEE Wirel. Commun.*, vol. 18, no. 1, pp. 15–21, Feb. 2011.

[3] S. Zhang, S. C. Liew, and P. P. Lam, "Hot topic: physical-layer network coding," in *Proc. 12th Annual Int. Conf. Mobile Comput. Network. ACM*, 2006, pp. 358–365.

[4] P. Popovski and H. Yomo, "Physical network coding in two-way wireless relay channels," in *IEEE Int. Conf. Commun.*, 2007, pp. 707–712.

[5] R. Ahlswede, N. Cai, S.-Y. R. Li, and R. W. Yeung, "Network information flow," *IEEE Trans. Inf. Theory*, vol. 46, no. 4, pp. 1204-1216, July 2000.

[6] S. Katti, H. Rahul, W. Hu, D. Katabi, M. Médard, and J. Crowcroft, "XORs in the air: practical wireless network coding," *IEEE/ACM Trans. Network.*, vol. 16, no. 3, pp. 497–501, June 2008.

[7] I.-J. Baik and S.-Y. Chung, "Network coding for two-way relay channels using lattices," in *IEEE Int. Conf. Commun.*, 2008, pp. 3898–3902.

[8] T. Koike-Akino, P. Popovski, and V. Tarokh, "Optimized constellations for two-way wireless relaying with physical network coding," *IEEE J. Sel. Areas Commun.*, vol. 27, no. 5, pp. 773–787, June 2009.

[9] T. Uricar and J. Sykora, "Design criteria for hierarchical exclusive code with parameter-invariant decision regions for wireless 2-way relay channel," *EURASIP J. Wirel. Commun. Network.*, vol. 2010, pp. 1–13, Jan. 2010.

[10] W. Chen, L. Hanzo, and Z. Cao, "Network coded modulation for two-way relaying," in *Proc. IEEE Wirel. Commun. Netowrk. Conf.*, 2011, pp. 1765–1770.

[11] T. Cui, T. Ho, and J. Kliewer, "Memoryless relay strategies for two-way relay channels," *IEEE Trans. Commun.*, vol. 57, nos. 10, pp. 3132–3143, Oct. 2009.

[12] J. W. Craig, "A new simple and exact result for calculating the probability of error for two-dimensional signal constellations," in *IEEE Military Commun. Conf.*, Nov. 1991, pp. 571–575.

三、IEEE 802.16m 上行測距技術研究

本節主要內容自下頁起，以學術論文初稿方式呈現。這些結果預定將包括在一篇尚未完成的碩士論文中。

Study in Initial Ranging for IEEE 802.16m

Preliminary Draft

***Abstract*—We consider the uplink ranging specifications in IEEE 802.16m and we study the associated uplink ranging method. Simulations are conducted to evaluate the detection performance.**

I. Introduction

Initial ranging is the procedure where a mobile station (MS) expresses desire to connect to a base station (BS). This procedure is variously named in different systems. Whereas it is termed initial ranging in IEEE 802.16m, such a procedure is termed random access in the 3GPP cellular communication systems.

During initial ranging, an MS transmits a ranging signal according to the format and the opportunity provided by the BS. However, due to motion and other reasons, it is likely that the signal arrives at the BS with a time offset, a frequency offset, or a power offset that is outside the allowed range of operation. Upon detection of a ranging signal, the BS may have to initiate a procedure for communicating with the ranging MS to adjust these parameters and to acquire further identity information regarding the MS.

The present study is concerned with the detection of initial ranging signals. In what follows, Sec. II introduces the ranging signal specifications of IEEE 802.16m. Sec. III presents the proposed ranging signal detection method which also obtains the timing of the detected signal. It will also present some simulation results. Sec. IV considers carrier frequency offset (CFO) estimation following detection of the ranging signals. And Sec. V is the conclusion.

II. Ranging Signal in IEEE 802.16m

The ranging channel in IEEE 802.16m can be classified into ranging channel for synchronized and non-synchronized MSs, where the former is for so-called "periodic ranging" and the latter is for initial access and handover. We consider the latter only.

According to IEEE 802.16m, a physical ranging channel for non-synchronized MSs consists of the ranging preamble (RP) with length of T_{RP} depending on the ranging subcarrier spacing $\triangle f_{RP}$, and the ranging cyclic prefix (RCP) with length of T_{RCP} in the time domain, where T_{RP}, $\triangle f_{RP}$, and T_{RCP} are some parameters. A ranging channel occupies a bandwidth of one subband. The ranging channel has two formats as described in Table I, where T_b, T_g, and $\triangle f$ are some other paramters, $k_1 = (N_{sym}+1)/2$ and $k_2 = (N_{sym}-4)/2$, with N_{sym} being the number of OFDMA symbols in a so-called "advanced air interface" (AAI) subframe. In our work, for simplicity, we let $T_b = 1024$, $T_g = 128$, $\triangle f = 10.9375$ kHz, and $N_{sym} = 6$, which are a proper set of values under IEEE 802.16m.

TABLE I
Ranging Channel Formats and Parameters

Format No.	T_{RCP}	T_{RP}	$\triangle f_{RP}$
0	$k_1 \times T_g + k_2 \times T_b$	$2 \times T_b$	$\triangle f/2$
1	$3.5 \times T_g + 7 \times T_b$	$8 \times T_b$	$\triangle f/8$

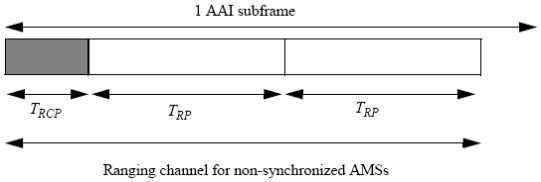

Fig. 1. Ranging channel allocation in AAI subframe [1, Fig. 570(a)].

Ranging channel for non-synchronized AMSs is allocated in one or three uplink (UL) AAI subframes for format 0 or format 1, respectively. Format 0 has a repeated structure as shown in Fig. 1. The transmission start time of the ranging channel is aligned with the UL AAI subframe start time at the AMS. The remaining time duration of the AAI subframes is reserved to prevent interference between the adjacent AAI subframes.

For initial ranging, each MS randomly chooses one of the ranging preamble codes from the available set of ranging preamble codes specified by the BS. These codes are Zadoff-Chu sequences. The pth ranging preamble code $x_p(k)$ is given by

$$x_p(k) = \exp(-j \cdot \pi \cdot \frac{r_p \cdot k(k+1) + 2 \cdot k \cdot s_p \cdot N_{CS}}{N_{RP}}), \quad (1)$$

where N_{RP}, r_p, s_p, and N_{CS} are some parameters. Based on the IEEE 802.16m specifications, we have $N_{RP} = 139$. For a detailed definition of the other parameters, we refer to [1].

III. Ranging Signal Detection and Timing Estimation

Fig. 2 shows the overall UL transmitter and receiver system. W assume that there may be more than one user transmitting ranging signals at the same time. The receiver at the BS will collect 4096 samples of the received signal located in the middle of a subframe as shown in Fig. 3. We add the first 2048 points to the latter 2048 points together to get $r(n)$. This is because the ranging signal has a two-times repetition structure as shown in Fig. 1. After the timing offset estimation and ranging code detection blocks, the output contains the information of detected codes and estimated timing offsets. Details of these blocks are described below.

We assume that the BS allocates u possible ranging codes, where $u = 8$. So the BS has to correlate each of these codes with $R(k)$ to determine if any of them is present and, for each

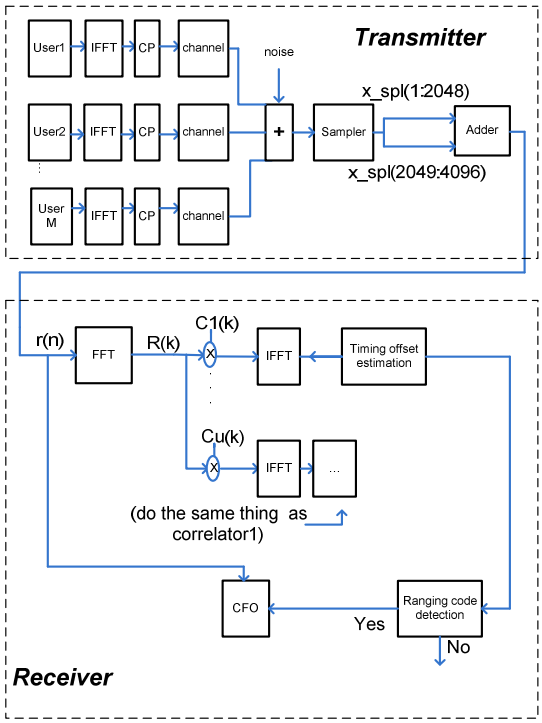

Fig. 2. Uplink transmitter and receiver system.

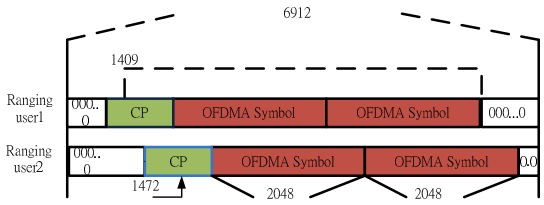

Fig. 3. Typical locations of received ranging signals in a subframe and the location of the 4096 samples taken by the BS receiver.

code that is present, its timing. This correlation is performed in the frequency domain for equivalent performance with a reduced complexity than time-domain correlation [2]. In this, we first perform 2048-point FFT on $r(n)$ to get $R(k)$. It is then multiplied point-wise with each of the u possible frequency-domain sequences $C_i(k)$ $(i = 1, 2, \ldots, u)$ constructed from the usable ranging codes. Recall that a ranging code is a 139-sample sequence. Therefore, each 2048-point sequence $C_i(k)$ contains 139 nonzero points that hold one Zadoff-Chu ranging code at the subcarriers specified by the BS for ranging use. The remaining 1909 subcarriers are all zero. Each of the 2048-point product is subject to a 2048-point IFFT. The results after IFFT, denoted $U_i(m)$, consist of 2048 complex values each. In a noiseless and interference-free situation, each $U_i(m)$ for which code i is present would be a bandpassed version of the wireless channel response. Otherwise, it would be null. In noise and interference (particularly that due to nonorthogonality between the ranging codes), the above conditions will not hold. But we can nonetheless use $U_i(m)$ for code and timing detection. Specifically, the norm operation (i.e., taking the absolute value) is performed on each point of $U_i(m)$. The norm values are used for code detection and timing offset estimation.

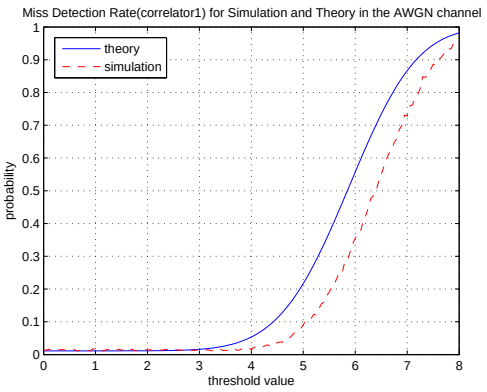

Fig. 4. Simulated miss detection probability in AWGN versus theory.

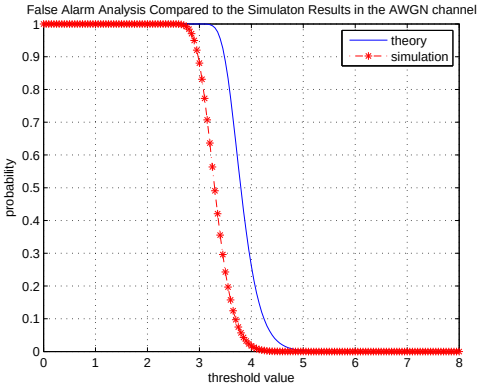

Fig. 5. Simulated false alarm probability in AWGN versus theory.

We detect the presence/absence of a code by comparing $|U_i(m)|$ to a threshold. The threshold has to be chosen according to the desired performance in miss detection probability and false alarm probability. The setting of such a desired performance has to do with overall wireless system design and is outside the scope of the present study. Suffice it to say that a higher detection threshold results in a higher miss detection probability but a lower false alarm probability. The contrary holds for a lower detection threshold.

We conducted some analysis on the relation between the detection threshold and the two probabilities based on the assumption that the inter-ranging code interference is Gaussian. The detailed analysis is not reproduced here. Figs. 4 and 5 show some simulated results on miss detection probability and false alarm probability in additive white Gaussian noise (AWGN) and compare them with theory. We see that the theoretical results provide a rather conservative prediction of the detection performance due to the Gaussian assumption on interference, which is an inexact model of the actual situation. Nevertheless, the shapes of the theoretical and simulated performance curves are quite similar and they appear to be horizontal translations of each other.

We now turn to look at the performance in timing estimation of the ranging signals. Figs. 6 and 7 show some simulation results with different number of ranging signals from different users occupying the same ranging channel, with

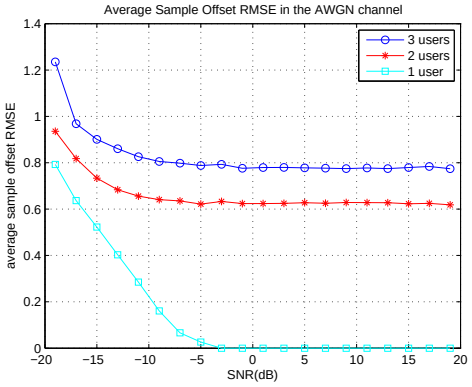

Fig. 6. Timing estimation accuracy in AWGN with different number of ranging signals occupying the same ranging channel.

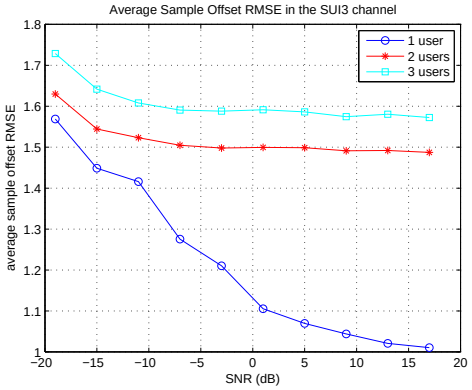

Fig. 7. Timing estimation accuracy in SUI3 channel with different number of ranging signals occupying the same ranging channel.

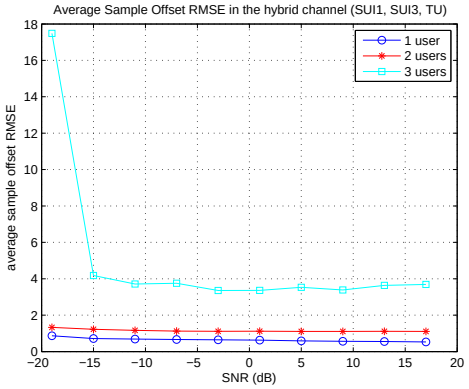

Fig. 8. Timing estimation accuracy with different number of ranging signals occupying the same ranging channel. The ranging signals experience different multipath wireless channels.

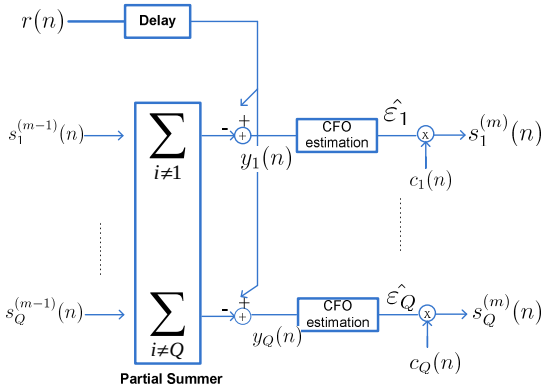

Fig. 9. Proposed multiple CFO estimation method.

all users' wireless channels being AWGN or SUI3 [3]. (The SUI wireless channels were originally developed for fixed wireless access studies. But they have been used for mobile radio studies by imposing a greater Doppler spread on their channel multipaths.) The performance in different wireless channel conditions show similar general trends, although they are different in details. We see that, even with three ranging users in one ranging channel, the root-mean-square (RMS) timing error is still under two sample, which appears accurate enough for practical application.

Now consider a case where there may be one, two, or three users transmitting ranging signals in the same ranging channel, but the multipath wireless channels of the users are different. Fig. 8 shows some results, where TU stands for the 6-path typical urban channel [4, ch. 2]. In this case, the performance is worse than in the previous two cases. But the maximum RMS timing error (which occurs with three users transmitting ranging signals in the same ranging channel) is still under four samples down to approximately -15 dB of signal-to-noise ratio (SNR), which appears sufficiently good for application.

IV. Carrier Frequency Offset Estimation

After detection of the ranging signals and estimation of their timing, we proceed to estimate their CFOs. This is so that the BS may feed this information back to the MSs for carrier frequency adjustment. As there may be more than one ranging signals occupying the same ranging channel, we propose an iterative method for CFO estimation based on parallel interference cancellation. The method is illustrated in Fig. 9. It is motivated by [5].

Note that, in the UL, we expect the ranging signals are only subject to fractional CFO (where the CFO normalized to the subcarrier spacing is a fractional number). This is because before the MS attempts ranging, it has to have already executed an initial downlink (DL) synchronization procedure to acquire the ability to receive DL signals from the BS.

In Fig. 9, $s_i^{(m)}(n)$ denotes the interference-cancelled version of the ith ranging signal after the mth iteration. In each iteration, the CFO of the ith ranging signal is estimated as

$$\hat{\varepsilon}_i = \frac{1}{-2\pi} \angle \sum_n y_i(n) \cdot y_i^*(n+N), \quad i = 1, 2, ..., Q, \qquad (2)$$

where Q is the number of ranging signals and $y_i(n)$ is the interference-cancelled received signal.

Fig. 10 shows some results of the estimation performance with all ranging signals in AWGN. The MSEs for all three ranging signals (users) decrease linearly with increasing SNR, which appears intuitively reasonable. Fig. 11 shows some results with the ranging signals experiencing different wireless channels. The performance becomes worse than that in AWGN (which may be intuitively expected) and channel-dependent

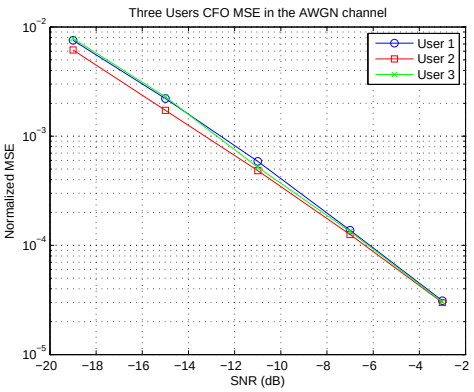

Fig. 10. MSE of CFO estimation where the ranging signals from different users experience different wireless channels.

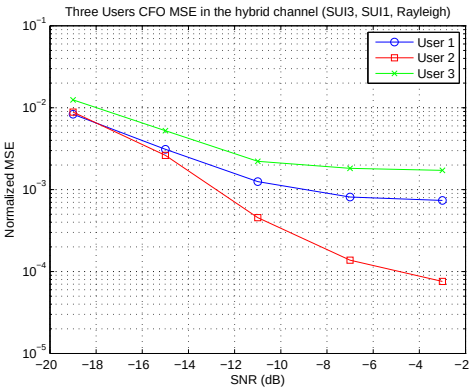

Fig. 11. MSE of CFO estimation in AWGN, where normalization is with respect to subcarrier spacing.

(which may also be intuitively expected). In any case, the MSE can be smaller than 1% of the subcarrier spacing (i.e., its square root being smaller than 10% of the subcarrier spacing) even with a very low SNR.

Concerning the convergence speed of the iterative estimation method, simulations show that it converges in several iterations. Fig. 12 shows one set of results for a very low SNR (-19 dB). In a higher SNR, the convergence can be even faster.

V. Conclusion

We have studied the ranging specifications of IEEE 802.16m. We proposed a ranging signal detection method which can also detect the timing of the received ranging signals. In addition, we proposed a method for estimating the carrier frequency offsets of the received ranging signals. The performance of these methods has been investigated with computer simulation. It was shown that we could still attain a reasonable level of performance even if multiple ranging signals were transmitted in the same ranging channel.

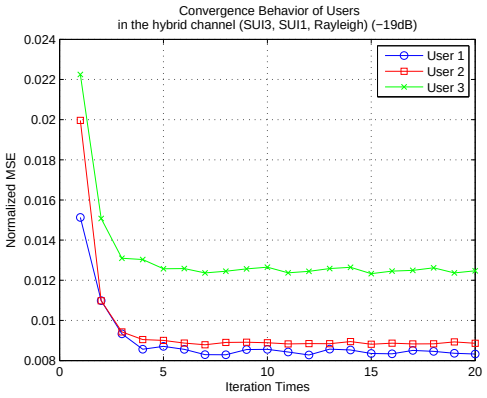

Fig. 12. Convergence behavior of iterative CFO estimation with multiple ranging signals occupying the same ranging channel with the signals experiencing different wireless channels.

References

[1] IEEE P802.16m/D12, *Draft Amendment for IEEE Standard for Local and Metropolitan Area Networks — Part 16: Air Interface for Fixed and Mobile Broadband Wireless Access Systems — Advanced Air Interface*. New York: IEEE, Feb. 2011.

[2] Soon Seng Teo, "IEEE 802.16e OFDMA TDD ranging process and uplink transceiver integration on DSP platform with real-time operating system," M.S. thesis, Industrial Technology R&D Master Program on Communication Engineering, National Chiao Tung University, Jan. 2008.

[3] V. Erceg *et al.*, "Channel models for fixed wireless applications," IEEE 802.16.3c-01/29c4, July 2001.

[4] G. L. Stüber, *Principles of Mobile Communication, 2nd ed.* Kluwer Academic, 2001.

[5] J. G. Andrews, "Interference cancellation for cellular systems: a contemporary overview," *IEEE Wireless Commun. Mag.*, vol. 12, no. 2, pp. 19–29, Apr. 2005.

四、IEEE 802.16m 多輸出入傳收技術研究

本節主要內容自下頁起，以學術論文初稿方式呈現。這些結果係摘自參考文獻[1]。

Study on Precoding and Equalization for the Spatial Multiplexing Mode of IEEE 802.16m

Preliminary Draft

***Abstract*—We focus on precoding and equalization for the spatial multiplexing mode of IEEE 802.16m closed-loop MIMO. In IEEE 802.16m MIMO systems, the precoding matrix is computed at the receiver, and then fed back to the transmitter. To reduce the fed back datas, only preferred matrix index is fed back. The preferred matrix index is selected from a subset of precoder called codebook defined by IEEE 802.16m. We based on zero-forcing (ZF) and minimum mean square error (MMSE) equalizer to design the selection method to select the best precoder. We proposed MMSE-Based and MaxminSNR-Based method. MMSE-Based method finds the precoder has the minimum mean square error. MaxminSNR-Based method finds the precoder that maximizes the minimum SNR of the two antennas. This method has to calculate each precoders antenna SNR. Then, we select the appropriate one to transmit back. We will compare with SVD-based and optimal precoder.**

I. Introduction

Orthogonal frequency division multiple access (OFDMA) has emerged as one of the prime multiple access schemes for broadband wireless networks. Some major examples are IEEE 802.16 Mobile WiMAX, IEEE 802.20 and 3GPP LTE. As a special case of multicarrier multiple access schemes, OFDMA exclusively assigns each subchannel to only one user, eliminating intra-cell interference. In frequency selective channels, an intrinsic advantage of OFDMA is its capability to exploit the so-called multiuser diversity provided by multipath channels. Other advantages of OFDMA include finer granularity and better link budget [12]. OFDMA can be easily generated using an inverse fast Fourier transform (IFFT) and received using a fast Fourier transform (FFT).

The IEEE 802.16 standard committee has developed a group of standards for wireless metropolitan area networks (MANs). OFDMA is used in the 2 to 11 GHz systems. The IEEE Standard 802.16-2004 was for broadband wireless access systems that provide a variety of wireless access services to fixed outdoor and indoor users. The 802.16e was designed to support terminal mobility with a speed up to 120 km/h [15]. The last two standards have now been combined in IEEE 802.16-2009.

In response to International Telecommunication Union Radiocommunication Section (ITU-R)'s plan for the fourth-generation mobile communication standard IMT-Advanced, the IEEE 802.16 standards group has set up the 802.16m (i.e., Advanced WiMAX) task group. The new frame structure developed by IEEE 802.16m can be compatible with IEEE 802.16e, reduce communication latency, support relay, and coexist with other radio access techniques (in particular, LTE). In the IEEE 802.16m working group, the high-level system description and evaluation methodology are captured in [9]. MIMO technologies again play an essential role in achieving the ambitious target set, which requires the 802.16m system to deliver twice the performance gain over a baseline 802.16e system in various measures, including sector throughput, average user throughput, and peak data rate, as well as cell-edge performance. Several new MIMO ingredients are proposed. Noticeable ones are transformed codebook for beamforming feedback, differential beamforming feedback, open-loop multiuser MIMO, and collaborative multicell MIMO [13]. We study the MIMO architecture and signal processing technology for 802.16m. In particular, we consider the zero-forcing (ZF) equalizer and minimum mean-square error (MMSE) equalizer approach wherein we employ the technique proposed in [2]. We follow [2] to introduce the ZF and MMSE equalizer with channel feedback selection problem.

This paper focuses on the precoding and equalization for the spatial multiplexing mode of IEEE 802.16m closed-loop (CL) multi-input multi-output (MIMO) systems. A problem associated with precoding is that the channel state information must be known at the transmitter. This may be difficult since the bandwidth of the feedback channel is usually limited. Thus, a codebook-based limited feedback precoding scheme is generally used. The main idea is to quantize the precoding matrix and feedback the index of the optimum precoder. We propose two methods to select the best precoder from a finite set of precoding matrices and we will compare with two other methods.

II. Introduction to IEEE 802.16m

We introduce the IEEE 802.16m basic frame structure and MIMO transmission mechanism. Much of the material is taken from [10].

A. Frame Structure

The AAI basic frame structure is illustrated in Fig. 1. Each 20 ms superframe is divided into four 5-ms radio frames. When using the same OFDMA parameters with channel bandwidth of 5, 10, or 20 MHz, each 5-ms radio frame further consists of eight subframes for $G = 1/8$ and 1/16. There are four types of subframes:

- Type-1 subframe consists of six OFDMA symbols.
- Type-2 subframe consists of seven OFDMA symbols.
- Type-3 subframe consists of five OFDMA symbols.
- Type-4 subframe consists of nine OFDMA symbols. This type shall be applied only to UL subframe for the 8.75 MHz channel bandwidth when supporting the WirelessMAN-OFDMA frames.

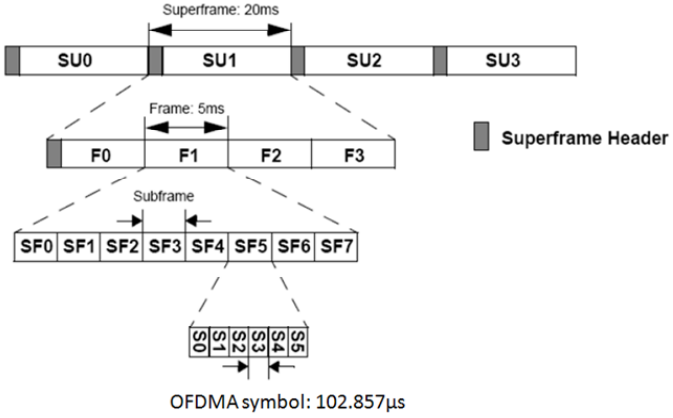

Fig. 1. Basic frame structure for 5, 10 and 20 MHz channel bandwidths (Fig.466 in [10]).

The basic frame structure is applied to FDD and TDD duplexing schemes, including H-FDD MS operation. The number of switching points in each radio frame in TDD systems shall be two, where a switching point is defined as a change of directionality, i.e., from DL to UL or from UL to DL.

B. Downlink MIMO Architecture and Data Processing

The architecture of downlink MIMO at the transmitter side is shown in Fig. 2. The MIMO encoder block maps L MIMO layers $(L \geq 1)$ onto M_t MIMO streams $(M_t \geq L)$, which are fed to the precoder block. For the spatial multiplexing modes in SU-MIMO, "rank" is defined as the number of MIMO streams to be used for the user allocated to the Resource Unit (RU). For SU-MIMO, only one user is scheduled in one RU, and only one forward error correction (FEC) block exists at the input of the MIMO encoder (vertical MIMO encoding at transmit side). For MU-MIMO, multiple users can be scheduled in one RU, and multiple FEC blocks exist at the input of the MIMO encoder (horizontal MIMO encoding or combination of vertical and horizontal MIMO encoding at transmit side, which is called multi-layer encoding). The precoder block maps MIMO stream(s) to antennas by generating the antenna-specific data symbols according to the selected MIMO mode. The subcarrier mapper blocks map antenna-specific data to the OFDM symbol.

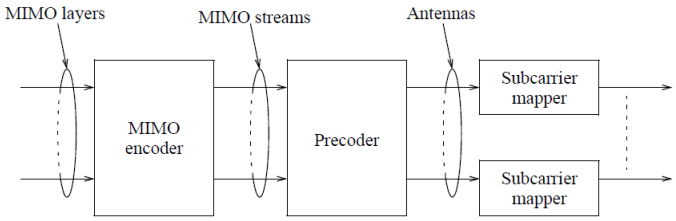

Fig. 2. DL MIMO architecture (Fig.537 in [10]).

C. MIMO Layer to MIMO Stream Mapping

MIMO layer to MIMO stream mapping is performed by the MIMO encoder. The MIMO encoder is a batch processor that operates on M input symbols at a time. The input to the MIMO encoder is represented by an $M \times 1$ vector as

$$\mathbf{s} = \begin{bmatrix} s_1 \\ s_2 \\ \vdots \\ s_M \end{bmatrix} \tag{1}$$

where s_i is the ith input symbol within a batch. In MU-MIMO transmissions, the M symbols belong to different AMSs. Two consecutive symbols may belong to a single MIMO layer. One AMS shall have at most one MIMO layer. MIMO layer to MIMO stream mapping of the input symbols is done in the space dimension first. The output of the MIMO encoder is an $M_t \times N_F$ MIMO STC matrix as,

$$\mathbf{x} = S(\mathbf{s}), \tag{2}$$

which serves as the input to the precoder, where M_t is the number of MIMO streams, N_F is the number of subcarriers occupied, $\mathbf{x}$ is the output of the MIMO encoder, $\mathbf{s}$ is the input MIMO layer vector, and $S()$ is a function that maps an input MIMO layer vector to an STC matrix which will be further defined specifically for various cases below. There are four MIMO encoder formats (MEF): SFBC, vertical encoding (VE), multi-layer encoding (ME), and conjugate data repetition (CDR). For SU-MIMO transmissions, the STC rate is defined as $R = \dfrac{M}{N_F}$

For MU-MIMO transmissions, the STC rate per user (R) is equal to 1 or 2.

1) SFBC Encoding: The input to the MIMO encoder is a 2×1 vector

$$\mathbf{s} = \begin{bmatrix} s_1 \\ s_2 \end{bmatrix}, \tag{3}$$

and the MIMO encoder generates the 2×2 SFBC matrix

$$\mathbf{x} = \begin{bmatrix} s_1 & -s_2^* \\ s_2 & s_1^* \end{bmatrix}. \tag{4}$$

Where $\mathbf{x}$ is a 2×2 matrix The matrix $\mathbf{x}$ occupies two consecutive subcarriers.

2) Vertical Encoding (VE): The input and the output of MIMO encoder are both the same $M \times 1$ vector as

$$\mathbf{x} = \mathbf{s} = \begin{bmatrix} s_1 \\ s_2 \\ \vdots \\ s_M \end{bmatrix} \tag{5}$$

where s_i, $1 \leq i \leq M$, belong to the same MIMO layer. The encoder is an identity operation.

3) Multi-layer Encoding (ME): The input and the output of MIMO encoder are again the same $M \times 1$ vector

$$\mathbf{x} = \mathbf{s} = \begin{bmatrix} s_1 \\ s_2 \\ \vdots \\ s_M \end{bmatrix}, \tag{6}$$

Mode index	Description	MIMO encoding format (MEF)	MIMO precoding
Mode 0	OL SU-MIMO (Tx diversity)	SFBC	Non-adaptive
Mode 1	OL SU-MIMO (SM)	VE	Non-adaptive
Mode 2	CL SU-MIMO (SM)	VE	Adaptive
Mode 3	OL MU-MIMO (SM)	ME	Non-adaptive
Mode 4	CL MU-MIMO (SM)	ME	Adaptive
Mode 5	OL SU-MIMO (Tx diversity)	CDR	Non-adaptive

Fig. 3. Downlink MIMO modes (from [10, Table 844]).

but now s_i, $1 \leq i \leq M$ belong to different MIMO layers, where two consecutive symbols may belong to a single MIMO layer. Multi-layer encoding is only used for MU-MIMO mode. The encoder is an identity operation.

4) Conjugate Data Repetition (CDR) Encoding: The input to the MIMO encoder is a 1×1 vector

$$s = s_1, \tag{7}$$

yielding

$$\mathbf{x} = [s_1 \quad s_1^*], \tag{8}$$

The CDR matrix $\mathbf{x}$ occupies two consecutive subcarriers.

D. Downlink MIMO Modes [10]

There are six MIMO transmission modes for unicast DL MIMO transmission as listed in Fig. 3 and 4. The allowed values of the parameters for each DL MIMO mode are shown in Figure 4.

E. Feedback Mechanisms and Operation [10]

1) MIMO Feedback Mode Selection: An AMS may send an unsolicited event-driven report to indicate its preferred MIMO feedback mode to the ABS. Event-driven reports for MIMO feedback mode selection may be sent on the P-FBCH during any allowed transmission interval for the allocated P-FBCH. The MIMO feedback mode are shown in Fig.5.

III. System Model

We consider a system as shown in Fig. 6.

Information bits for subcarrier k are first passed through the modulator and sent into the encoder. There are four different types of encoder, but we will not discuss them. After passing through the encoder, there are M streams. Let $\mathbf{s}$ be the symbol vector at the encoder output as

$$\mathbf{s}_k = [s_{k,1} s_{k,2} \dots s_{k,M}]^T. \tag{9}$$

For convenience, we assume that the M data streams are equally-powered and independent to each other. That is, $E[\mathbf{s}_k \mathbf{s}_k^*] = \mathbf{I}_M$ which $\mathbf{A}^*$ denotes complex-conjugate of matrix $\mathbf{A}$. We denote the precoder by $\mathbf{F}$. $\mathbf{F}$ is an $N_t \times M$ matrix. There are several precoder codebook sets. The signal after precoding can be expressed as

$$\mathbf{x}_k = \mathbf{F}\mathbf{s}_k. \tag{10}$$

	Number of transmit antennas	STC rate per MIMO layer	Number of MIMO streams	Number of subcarriers	Number of MIMO layers
	N_t	R	M_t	N_F	L
MIMO mode 0	2	1	2	2	1
	4	1	2	2	1
	8	1	2	2	1
MIMO mode 1 and MIMO mode 2	2	1	1	1	1
	2	2	2	1	1
	4	1	1	1	1
	4	2	2	1	1
	4	3	3	1	1
	4	4	4	1	1
	8	1	1	1	1
	8	2	2	1	1
	8	3	3	1	1
	8	4	4	1	1
	8	5	5	1	1
	8	6	6	1	1
	8	7	7	1	1
	8	8	8	1	1
MIMO mode 3 and MIMO mode 4	2	1	2	1	2
	4	1	2	1	2
	4	1	3	1	3
	4	1	4	1	4
	8	1	2	1	2
	8	1	3	1	3
	8	1	4	1	4

Fig. 4. DL MIMO parameters (from [10, Table 845]).

where $\mathbf{x}_k$ is a length N_t vector and N_t is the number of transmit antennas. We assume that $N_t > M$. Then we transform the signal vector to the time domain using IDFT and add CP. Let the number of the receive antenna be N_r. We consider a multipath channel, whose input-output relation in the frequency domain can be written as

$$\mathbf{y}_k = \mathbf{H}\mathbf{F}\mathbf{x}_k + \mathbf{n}_k. \tag{11}$$

where $\mathbf{y}_k$ is the received symbol vector, $\mathbf{H}$ is the $N_t \times N_r$ channel matrix and $\mathbf{n}_k$ is the $N_r \times 1$ noise vector. We assume that the entries of $\mathbf{H}$ are independent and identically distributed (i.i.d.) and their distributions are complex normal with zero mean and unit variance, denoted by $CN(0,1)$. Similarly, the entries of $\mathbf{n}_k$ are also i.i.d. and the distribution is $CN(0, N_0)$. After passing the signal over the channel, we remove the CP and transform the result back to frequency domain. We consider two different kinds of equalizer, ZF and MMSE. Let $\mathbf{G}$ be the $M \times N_r$ equalizer matrix.

We set each symbol has the same precoder so the optimum equalizer for the MMSE equalizer is given by

$$\mathbf{G} = (\mathbf{H}\mathbf{F}\mathbf{F}^H\mathbf{H}^H + \mathbf{R}_n)^{-1}\mathbf{H}\mathbf{F}. \tag{12}$$

On the other hand, the ZF equalizer can be derived as

$$\mathbf{G} = (\mathbf{H}\mathbf{F})^\dagger. \tag{13}$$

In either case, the signal vector at the equalizer output is given by

$$\hat{\mathbf{x}} = \mathbf{G}\mathbf{H}\mathbf{F}\mathbf{x} + \mathbf{G}\mathbf{n}. \tag{14}$$

MIMO Feedback Mode	Description and Type of RU	Feedback Content	Support MIMO Mode Outside the OL region	Support MIMO Mode Inside the OL region
0	OL SU MIMO SFBC/SM (Diversity: DLRU, NLRU) Sounding based CL SU and MU MIMO	1. STC rate 2. Wideband CQI	MIMO mode 0 and MIMO mode 1 Flexible adaptation between the two modes STC rate=1:SFBC CQI 2<=STC rate<=4:SM CQI In DLRU: M_t=2 for SM In NLRU: M_t>=2 for SM For sounding based CL SU MU MIMO, STC rate =1:SFBC CQI	MIMO mode 0 and MIMO mode 1 Flexible adaptation between the two modes STC rate=1:SFBC CQI STC rate=2:SM CQI In DLRU only
1	OL SU MIMO SM (Diversity: NLRU)	1. Wideband CQI	n.a	MIMO mode 5 STC rate = 1/2
2	OL SU MIMO SM (localized: SLRU)	1. STC rate 2. Subband CQI 3. Subband selection	MIMO Mode 1 1<=STC rate<=8	MIMO mode 5 STC rate = 1/2
3	CL SU MIMO (localized: SLRU)	1. STC rate 2. Subband CQI 3. Subband PMI 4. Subband selection 5. Wideband correlation matrix	MIMO mode 2 1<=STC rate<=8	n.a
4	CL SU MIMO (Diversity: NLRU)	1. Wideband CQI 2. Wideband PMI 3. Wideband correlation matrix	MIMO mode 2 ($M_t \leq 4$)	n.a
5	OL MU MIMO (localized: SLRU)	1. Subband CQI 2. Subband selection 3. MIMO stream indicator	MIMO mode 3	MIMO mode 3
6	CL MU MIMO (localized: SLRU)	1. Subband CQI 2. Subband PMI 3. Subband selection 4. Wideband correlation matrix	MIMO mode 4	n.a
7	CL MU MIMO (Diversity: NLRU)	1. Wideband CQI 2. Wideband PMI 3. Wideband correlation	MIMO mode 4	n.a

Fig. 5. MIMO feedback modes (from [10, Table 849]).

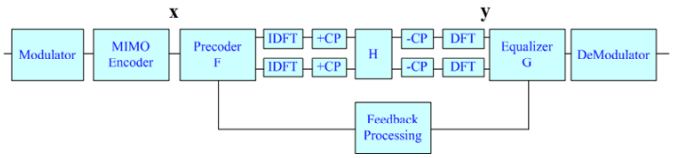

Fig. 6. System structure.

IV. Proposed Feedback Selection Schemes

In this section, we derive two feedback selection schemes max minSNR-based search method and MMSE-based exhaustive search method that can greatly reduce the complexity.

A. MaxminSNR-Based Search Method

In this method, We maximize the minimum SNR at the receiver antennas under MMSE or ZF equalization. It can be thought as minimize the maximum symbol error rate (SER) at the receive antennas. The signal power per receive antenna can be expressed as

$$| \mathbf{g}_k^T \mathbf{H} \mathbf{F}_i \mathbf{x} |^2 . \tag{15}$$

The noise power is

$$\sigma_n^2 | \mathbf{g}_k^T \mathbf{g}_k | . \tag{16}$$

The optimum precoding matrix $\mathbf{F}$ selected from the codebook $\mathbf{C}$ maximizes the minimum SNR of at the receive antennas as

$$\begin{aligned} \mathbf{F} &= \arg \max_{\mathbf{F}_i} \min_{k|\mathbf{F}_i} \mathrm{SNR}_k \\ &= \arg \max_{\mathbf{F}_i} \min_{k|\mathbf{F}_i} \frac{| \mathbf{g}_k^T \mathbf{H} \mathbf{F}_i \mathbf{x} |^2}{\sigma_n^2 | \mathbf{g}_k^T \mathbf{g}_k |} \end{aligned} \tag{17}$$

where k is the index of the receive antennas, i is the index of the precoder, and $\mathbf{g}_k$ is the equalizer for kth receive antenna.

B. MMSE-Based Exhaustive Search Method

In this method, we minimize the mean square error (MSE) between $\hat{\mathbf{X}}$ and $\mathbf{X}$ under the ZF or the MMSE equalizer. We compare all possible precoders to find the best one in the source that

$$\min MSE = \arg \min_{F_i} \|\hat{\mathbf{X}} - \mathbf{X}\|^2. \tag{18}$$

For ZF equalizer, therefore,

$$\min MSE = \arg \min_{F_i} \|(\mathbf{H}\mathbf{F}_i)^\dagger \mathbf{H}\mathbf{F}_i \mathbf{X} + (\mathbf{H}\mathbf{F}_i)^\dagger \mathbf{n} - \mathbf{X}\|^2, \tag{19}$$

and for the MMSE equalizer,

$$\begin{aligned} \min MSE = \arg \min_{F_i} \|&(\mathbf{H}\mathbf{F}_i \mathbf{F}_i^H \mathbf{H}^H + \mathbf{R}_n^{-1}) \mathbf{H}\mathbf{F}_i \mathbf{H}\mathbf{F}_i \mathbf{X} \\ &+ (\mathbf{H}\mathbf{F}_i \mathbf{F}_i^H \mathbf{H}^H + \mathbf{R}_n^{-1}) \mathbf{H}\mathbf{F}_i \mathbf{n} - \mathbf{X}\|^2. \end{aligned} \tag{20}$$

Then we will transmit the precoder index i back to the transmitter. The transmitter will use this precoder to allocate the power. In this method, the computation of complexity is high, because we have to evaluate all the precoders.

V. Simulation Results

In the simulation, we consider both additive white Gaussian noise (AWGN) channels.

A. System Parameter and Channel Model

Channel models for evaluation of IMT-Advanced candidate radio interface technologies [6]. We use the Suburban macrocell model. The parameter are in Fig. 7. The root-mean-square (RMS) delay spread of Suburban macrocell channel is 75.7485 ns. Table I gives the primitive and derived parameters used in our simulation work. The results are averages over 10,000,000 channel realizations.

B. Two Transmit Antennas and Two Receive Antennas with Rank Two

For comparison, we consider a no feedback system with feedback system.

First, consider the case of AWGN channels. Fig. 8 shows the symbol-error-rate (SER) performance of the systems. There is no difference between theory, MMSE equalizer with feedback and MMSE equalizer without feedback.

TABLE I
OFDMA DOWNLINK PARAMETERS

Parameters	Values
Bandwidth	10 MHz
Central frequency	3.5 GHz
N_{used}	865
Sampling factor n	28/25
G	1/8
N_{FFT}	1024
Sampling frequency	11.2 MHz
Subcarrier spacing	10.94 kHz
Useful symbol time	91.43 μs
CP time	11.43 μs
OFDMA symbol time	102.86 μs
Sampling time	44.65 ns

Cluster #	Delay [ns]			Power [dB]			AoD [°]	AoA [°]	Ray power [dB]
1	0	5	10	-3.0	-5.2	-7.0	0	0	-13.0
2	25			-7.5			13	-71	-20.5
3	35			-10.5			-15	-84	-23.5
4	35			-3.2			-8	46	-16.2
5	45	50	55	-6.1	-8.3	-10.1	-12	-66	-16.1
6	65			-14.0			-17	-97	-27.0
7	65			-6.4			12	-66	-19.4
8	75			-3.1			-8	-46	-16.1
9	145			-4.6			-10	-56	-17.6
10	160			-80			-13	73	-21.0
11	195			-7.2			12	70	-20.2
12	200			-3.1			8	-46	-16.1
13	205			-9.5			14	-80	-22.5
14	770			-22.4			22	123	-35.4
Cluster AS_{BS} = 2°									
Cluster AS_{MS} = 10°									

Fig. 7. Suburban macrocell channel model [9].

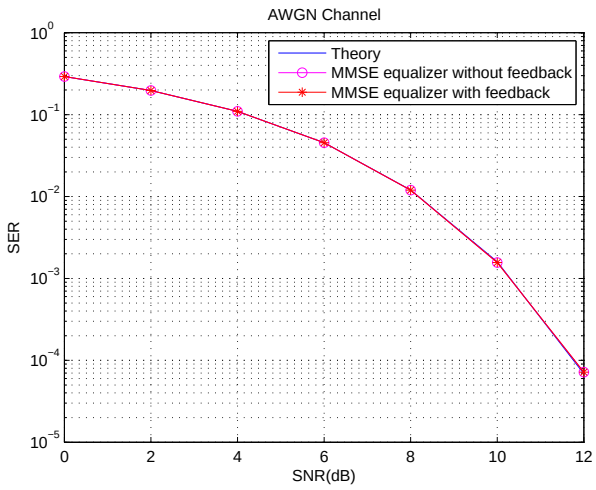

Fig. 8. SER performance in AWGN.

Second, we consider the case of suburban macrocell channel with 2 transmit antennas and 2 receive antennas transmiting two streams. Figs. 9–12 show the performance of different feedback methods at velocities of 30 and 120 km/h. We can see that both MSE and SER have the same curve. This is because the MMSE equalizer is finding the minimum mean square error and it also can be seem worked in SER. The optimum precoder method leads all the methods because it use the sounding method to transmit back the best precoder. Also both ZF and MMSE equalizer can achieve diversity one. We also compare all the methods in ZF and MMSE equalizer. MMSE equalizer leads the ZF equalizer both in MSE and SER. This is because ZF equalizer has the noise enhancement problem. We can see that there is almost no gain with precoding and no precoding.

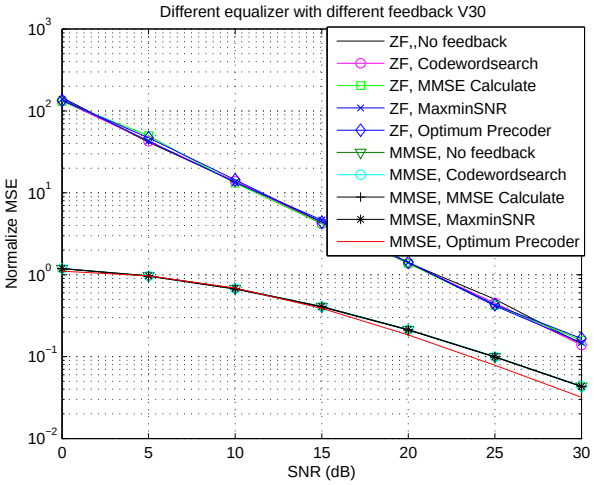

Fig. 9. MSE for QPSK using ZF and MMSE equalizer with different feedback methods at 30 km/h in multipath Suburban channel.

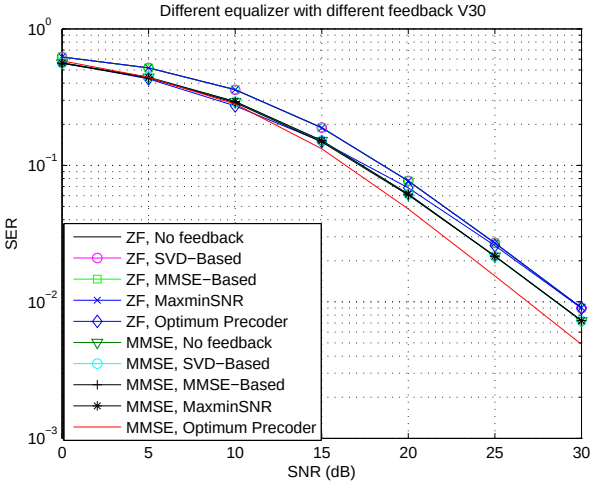

Fig. 10. SER for QPSK using ZF and MMSE equalizer with different feedback methods at 30 km/h in multipath Suburban channel.

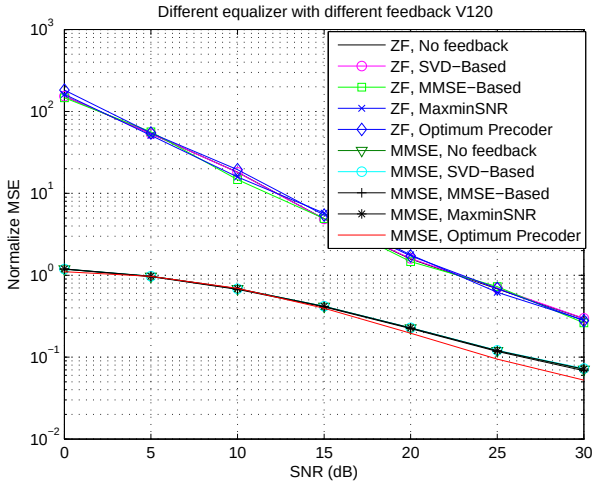

Fig. 11. MSE for QPSK using ZF and MMSE equalizer with different feedback methods at 120 km/h in multipath Suburban channel.

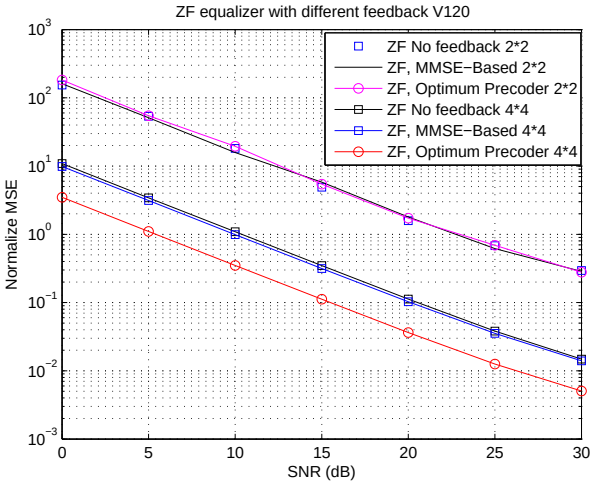

Fig. 13. MSE for QPSK using ZF equalizer with different feedback methods and different antennas at 120 km/h in multipath Suburban channel.

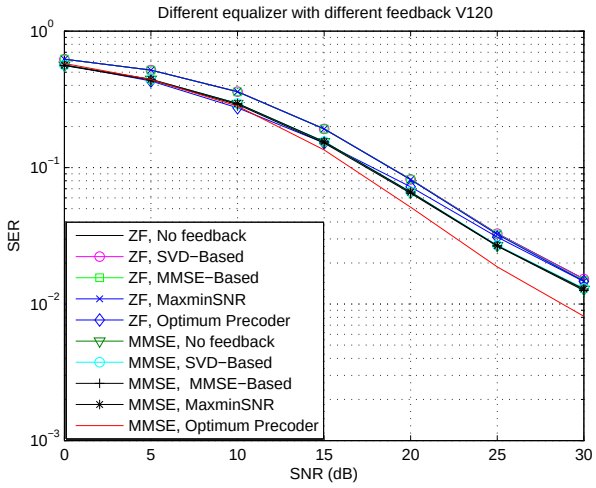

Fig. 12. SER for QPSK using ZF and MMSE equalizer with different feedback methods at 120 km/h in multipath Suburban channel.

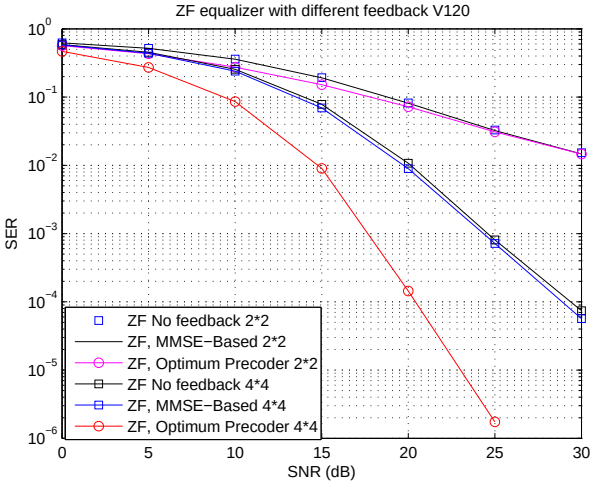

Fig. 14. SER for QPSK using ZF equalizer with different feedback methods and different antennas at 120 km/h in multipath Suburban channel.

C. Four Transmit Antennas and Four Receive Antennas with Rank Two

In the last part, we consider the case of suburban macrocell channel with 4 transmit antennas and 4 receive antennas transmiting two streams. Figs. 13–12 show that there is a 1dB gain with precoding and no precoding.

D. Computation Complexity

In the design of signal processing algorithms, an analysis of the required number of flops is often derivable. Where a flop means a floating point operation. In this regard, a dot product of length n vectors is considered to require $2n$ flops because there are n multiplications and n adds. We derive the expressions for the number of needed flops that the equalization in the CL MIMO requires. [16] gives the flop counts of some common matrix operations.

In an order of magnitude study, we often throw away the lower order terms since their inclusion does not contribute to the overall flop count. But if the n is small, we have to keep the all the terms. This happens to be our case. We list the total flop counts per subcarrier in Fig. 15.

We can see that optimum precoder performs well in complexity because it does not have a complex computation flow. Also we can see that ZF equalizer is much easier than MMSE equalizer. SVD-based and $\max\min$SNR-based search method have less complexity in high order matrix. We can have a conclusion that if the matrix size is low, we can use the MMSE-based search method. When the matrix size is high, we use SVD-based and $\max\min$SNR-based search method.

VI. Conclusion

We considered joint design at both end of the links and introduced two classes of linear equalization: Zero-forcing

	Total flop per subcarrier	Total flop (n=2)	Total flop (n=4)	Total flop (n=8)
ZF	$8n^3/3$	64/3	512/3	4096/3
ZF, SVD-Based	$116n^3/3+4n^2$	976/3	7616/3	60160/3
ZF, MMSE-Based	$136n^3/3+8n^2$	1300/3	9088/3	71168/3
ZF, MaxminSNR	$128n^3/3+16n^2+24n+32$	1456/3	9344/3	69280/3
ZF, Optimum precoder	$44n^3/3+n^2$	364/3	2864/3	22720/3
MMSE	$20n^3/3+n^2$	172/3	1328/3	10432/3
MMSE, SVD-Based	$128n^3/3+5n^2$	1084/3	8432/3	66496/3
MMSE, MMSE-Based	$196n^3/3+13n^2$	1724/3	13168/3	102848/3
MMSE, MaxminSNR	$176n^3/3+20n^2+24n+32$	1888/3	12608/3	94624/3
MMSE, Optimum precoder	$50n^3/3+9n^2$	508/3	3632/3	27328/3

Fig. 15. Number of flops per subcarrier of each method.

equalizer and Minimum-mean-square-error equalizer. Then proposed two methods for closed-loop MIMO precoder selection and compared with other two methods in singlepath and multipath. We also considered the complexity of each methods.

REFERENCES

[1] A. Barg and D. Y. Nogin, "Bounds on packings of spheres in the Grassmann manifold," *IEEE Trans. Inf. Theory*, vol. 48, no. 9, pp. 2450–2454, Sep. 2002.

[2] Glen Ballou, "Filters and equalizers," in Handbook for *Sound Engineers*, 4th ed. Focal Press, 2008.

[3] Che-Chen Chou, Hsi-Chei Chen and Jen-Ming Wu, "A low complexity channel decomposition and feedback strategy for MIMO precoder design," in *Proc. IEEE Int. Conf. Acoustics Speech Signal Processing,*, Apr. 2009, pp. 2705–2707.

[4] John H. Conway, Ronald H. Hardin, and Neil J. A. Sloane, "Packing lines, planes, etc.: packings in Granssmannian spaces," *Exper. Math.*, vol. 5, pp. 139–159, 1996.

[5] V. Erceg *et al.*, "Channel models for fixed wireless applications," IEEE 802.16.3c-01/29r4, July 2001.

[6] "Guidelines for evaluation of radio interface technologies for IMT-Advanced (Doc ITU-R 5/69)," Draft New Report ITU-R M.[IMT.EVAL], October 2008.

[7] J. W. Huang, E. K. S. Au, and V. K. N. Lau, "Linear precoder and equalizer design for uplink multiuser MIMO systems with imperfect channel state information," in *Proc. IEEE Wireless Commun. Network. Conf.*, Mar. 2007, pp. 1296–1301.

[8] K.-C. Hung and D. W. Lin, "Pilot-based LMMSE channel estimation for OFDM systems with power-delay profile approximation,"*IEEE Trans. Veh. Technology*, vol. 59, no. 1, pp. 150–159, Jan. 2010.

[9] IEEE P802.16m, "Project 802.16m evaluation methodology document (EMD)," IEEE 802.16m-08/004r5, Jan. 2009.

[10] IEEE 802.16 Task Group m, *Part 16: Air Interface for Fixed and Mobile Broadband Wireless Access Systems — Advanced Air Interface (working document)*. Doc. no. IEEE 802.16m/D4, Feb. 3, 2010.

[11] S. M. Kay, "Fundamentals of Statistical Signal Processing:Vol. I-Estimation Theory.", Englewood Cliffs, NJ: Prentice-Hall, 1993.

[12] Hongxiang Li and Hui Liu, "An analysis on uplink OFDMA optimality," in *Proc. IEEE Veh. Technol. Conf.*, vol. 3, 2006, pp. 1339–1343.

[13] Qinghua Li, Xintian Lin, Jianzhong Zhang and Wonil Roh, "Advancement of MIMO technology in WiMAX: from IEEE 802.16d/e/j to 802.16m," *IEEE Communication Magazine*, vol. 47, no. 6, pp. 100–107, June 2009.

[14] David J. Love and Robert W. Heath. Jr., "Limited feedback precoding for spatial multiplexing systems using linear receivers," *IEEE Trans. Inf. Theory*, vol. 51, no. 8, pp. 2967–2976, Aug. 2005.

[15] Liangshan Ma and Dongyan Jia, "The competition and cooperation of WiMAX, WLAN and 3G," in *Int. Conf. Applica. Sys. Mobile Tech.*, Nov. 2005, pp. 1–5.

[16] Gene H. Golub and Charles F. Van Loan, *Matrix Computations, 2nd ed.* Johns Hopkins University Press, 1990.

[17] D. Palomar, John M. Cioffi, and Miguel Angel Lagunas, "Joint Tx-Rx beamforming design for multicarrier MIMO channels: a unified framework for convex optimization," *IEEE Trans. Signal Processing*, vol. 51, no. 9, Sep. 2003, pp. 2381–2401.

[18] A. Scaglione, P. Stoica, S. Barbarossa, G. B. Giannakis, and H. Sampath, "Optimal sesigns for space-time linear precoders and decoders," *IEEE Trans. Signal Process.*, vol. 50, no. 5, pp. 1051–1064, May 2002.

[19] H. Stark and J. W. Woods, *Probability and Random Processes, 3rd ed.* Upper Saddle River, New Jersey: Prentice-Hall, 2002.

[20] R. van Nee and R. Prasad, *OFDM for Wireless Multimedia Communications.* Boston: Artech House, 2000.

[21] Yi-Ling Wang, "Research in and DSP implementation of channel estimation techniques for IEEE 802.16e OFDMA uplink and downlink," M.S. thesis, Dept. Electronics Eng. and Institute of Electronics, National Chiao Tung Unversity, Hsinchu, Taiwan, R.O.C., June 2007.

[22] L. Wilhelmsson, B. Bernhardsson, and L. Andersson, "Channel estimation by adaptive interpolation," U.S. patent 7,433,433, Oct. 7, 2008.

[23] W.-R. Wu and T.-H. Hsu, "A low-complexity precoder searching algorithm for MIMO-OFDM systems," in *Proc. IEEE Personal Indoor Mobile Radio Communications Conf.*, Sep. 2009, pp. 2021–2024.

五、IEEE 802.16m 初始下行同步技術之數位訊號處理器軟體實現研究

本節主要內容自下頁起，以學術論文初稿方式呈現。這些結果係摘自參考文獻[2]。本項成果係衍伸之前在演算法方面的研究成果[3]。

Digital Signal Processor Software Implementation of Initial Downlink Synchronization Method for IEEE 802.16m

Preliminary Draft

ABSTRACT

In this paper, the research focus on initial downlink synchronization of IEEE 802.16m, and discuss the implementation issue of DSP. We use the initial downlink (DL) synchronization algorithms in [1], [2] of IEEE 802.16m, and implement it on DSP. DL synchronization includes the estimation of symbol timing, carrier frequency offset, and preamble index identification. In terms of simulations, above all, In order to compare the performance, we implement the algorithm into the floating-point and fixed-point version. In the end, we modified the fixed-point version on the digital signal processor platform, and optimize the speed of our programs to reduce operation complexity. Although the performance is degraded because of fixed-point modification, the results still can be accepted.

1. INTRODUCTION

ITU-R defined the criterion of the fourth-generation (4G) mobile communication standard IMT-Advanced formally in June 2003, that the data rate need be higher than 100 Mbps in the environment with the high mobility and 1 Gbps in the static environment. Therefore, IEEE 802.16m Task Group (TGm) has set up the 802.16m (i.e., Advanced WiMAX or WiMAX 2) since December 2006 in order to compete for the fourth-generation standard. The new frame structure developed by IEEE 802.16m is such that it can be compatible with IEEE 802.16e, reduce communication latency, support relay and coexist with other radio access techniques, so that it can become one of the promising candidates of 4G.

In this work, we study the digital signal processor (DSP) software implementation of a previously developed initial downlink synchronization method for IEEE 802.16m system with a time division duplex (TDD) mode [1], [2]. The initial downlink synchronization involves frequency offset correction, timing recovery and bandwidth detection. In the procedure that we have developed, channel estimation is also obtained simultaneously.

Our DSP implementation uses Texas Instrument (TI) fixed-point DSP platform. We accelerate the execution speed of the programs and utilize difference optimization techniques to reduce the computational complexity.

The contributions of this work are as follows:

- We modify the program from Matlab code to C code.
- We modify the fixed-point implementation on DSP.
- We employ various optimization techniques to accelerate the execution speed of the programs in the DSP implementation.

This thesis is organized as follows. We first introduce the IEEE 802.16m standard in chapter 2. In chapter 3, we present the synchronization algorithm. Chapter 4 introduces the DSP implementation platform. We discuss the DSP optimization methods and presents the optimization results in chapter 5. Finally, the conclusion is given in chapter 6, where we also point out some potential future work.

2. SIGNAL MODEL AND SYSTEM PARAMETERS

One feature of the IEEE 802.16m is the selectable FFT size, from 512 to 2048 in multiples of 2. Also, the cyclic prefix sizes (1/4, 1/8, 1/16 and 1/32) have been defined in IEEE 802.16m. In this paper, we consider a TDD, CP 1/8 signal model, and focus on the PA-Preamble structure. The location of the A-Preamble symbol is specified as the first symbol of frame. PA-Preamble is located at the first symbol of second frame in a superframe while SA-Preamble is located at the first symbol of remaining three frames. Fig. 1 depicts the location of A-Preamble symbols and an example of IEEE 802.16m frame structure. Each frame in the DL transmission begins with a preamble followed by a DL transmission and an UL transmission period. The DL/UL subframes and UL/DL subframes are separated by transmit/receive transition gap (TTG) and receive/transmit transition gap (RTG) respectively.

There are three possible PA-preamble series, as shown in Fig. 2. Because the PA-Pramble series are known, we utilize this knowledge to derive the initial downlink synchronization algorithm. Although there are three different PA-Preambles with different bandwidth, 5-MHz, 10-MHz, and 20-MHz, but the intercommunity is all the three PA-Preamble, which length is all 216-point, locate on the middle part of their own bandwidth. Therefore, when the MS receives the signal, it can only observe 5-MHz bandwidth because there is not any information out of 5MHz at all, whatever the system bandwidth is. In the other words, we do downsampling from the 10-MHz and 20-MHz to the 5MHz without losing any information.

Fig. 3 depicts a model about the 576-points power sum with the window sliding. We know the information of TTG + RTG =165 μs in [5], so it is reasonable to suppose RTG is 45 μs , about 256 sampling periods, and CP factor is 1/8 in our study. We can also know the power of PA-Preamble is larger than the common data symbol because the amplitude of PA-Preamble

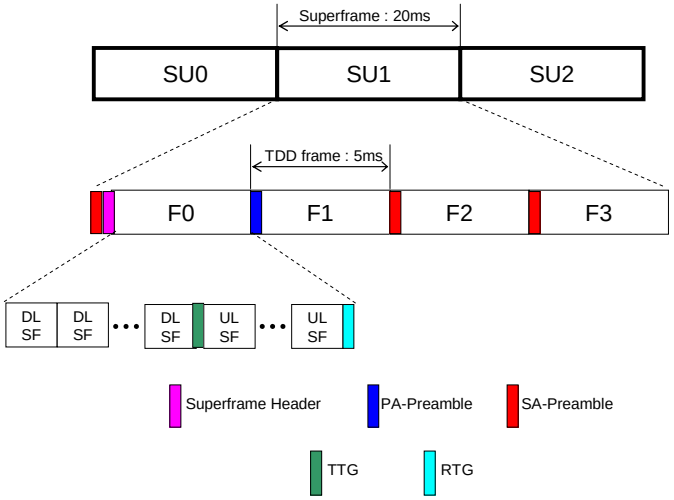

Fig. 1. Location of the A-Preamble symbol (re-arranged from Fig. 500 in [5]).

Index	Carrier	BW	Series to modulate
0	Fully configured	5 MHz	6DB4F3B16BCE59166C9CEF7C3C8CA5EDFC16A9D1DC01F2AE6AA08F
1		7,8.75,10 MHz	1799628F3B9F8F3B22C1BA19EAF94FEC4D37DEE97E027750D298AC
2		20 MHz	92161C7C19BB2FC0ADE5CEF3543AC1B6CE6BE1C8DCABDDD319EAF7
3		reserved	6DE116E665C395ADC70A89716908620868A60340BF35ED547F8281
4		reserved	BCFDF60DFAD6B027E4C39DB20D783C9F467155179CBA31115E2D04
5		reserved	7EF1379553F9641EE6ECDBF5F144287E329606C616292A3C77F928
6		reserved	8A9CA262B8B3D37E3158A3B17BFA4C9FCFF4D396D2A93DE65A0E7C
7		reserved	DA8CE648727E4282780384AB53CEEBD1CBF79E0C5DA7BA85DD3749
8		reserved	3A65D1E6042E8B8AADC701E210B5B4B650B6AB31F7A918893FB04A
9		reserved	D46CF86FE51B56B2CAA84F26F6F204428C1BD23F3D888737A0851C
10	Partially configured	N/A	640267A0C0DF11E475066F1610954B5AE55E189EA7E72EFD57240F

Fig. 2. PA-Preamble Series (Table 780 in [5]).

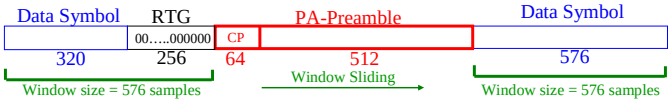

Fig. 3. Window sliding structure [1].

is boosted before transmitting, and the detail parameter refer to [5].

Other parameter values are specified in Table I.

3. Initial Downlink Synchronization Algorithm for IEEE 802.16m

The downlink synchronization can be divided into two type: initial synchronization and normal synchronization. When the advance mobile station (AMS) receiver enters the network for the first time, it need to perform initial DL synchronization. Afterward, the AMS needs to keep trading the carrier frequency, and the timing, and the power level, which constitutes the work of normal DL synchronization. In this thesis, our study focuses on initial DL synchronization; so we discuss the initial DL synchronization problem of the IEEE 802.16m TDD system and introduce the initial DL synchronization algorithm of [1], [2].

TABLE I

System Parameters Used in Our Study

Parameters	Values		
System Channel Bandwidth (MHz)	5	10	20
Sampling Frequency (MHz)	5.6	11.2	22.4
FFT Size	512	1024	2048
Subcarrier Spacing (kHz)	10.94	10.94	10.94
Useful Symbol Time (μsec)	91.4	91.4	91.4
Guard Time (μsec)	11.4	11.4	11.4
OFDMA Symbol Time (μsec)	102.9	102.9	102.9

1. *The Initial Synchronization Problems*

In the DL, due to potentially large tolerance in the free-running oscillator frequency of the MS, and due to the motion-induced Doppler spread, there may be large CFO in the received signal. The large CFO can be partitioned into the fractional part of "normalized CFO" (where normalization is with respect to the subcarrier spacing) and integral part of "normalized CFO". We call them "fractional CFO" and "integer CFO" respectively in this paper.

2. *Initial DL Synchronization*

1) Coarse Timing Synchronization: Fig. 3 depicts a model about the 576-points power sum with the window sliding. We know the information of TTG + RTG =165 μs in [5], so it is reasonable to suppose RTG is 45 μs, about 256 sampling periods, and CP factor is 1/8 in our study. We can also know the power of PA-Preamble is larger than the common data symbol because the amplitude of PA-Preamble is boosted before transmitting [5].

When the MS receives the PA-Preamble signal subject to delay, multipath propagation, and additive noise, the first task is to estimate the coarse timing to facilitate later work. Refer to Fig. 3. We consider summing the signal power in a 576-point window. With the window sliding, we can decide the coarse timing as the point with the maximum power sum. This technique can actually be interpreted as quasi-maximum likelihood (ML) noncoherent detection of the preamble timing.

According to [1], [2], Figs. 4 and 5 show the results of power sum with the window sliding in 0 dB of signal-to-noise ratio (SNR), under the AWGN channel and the SUI-5 channel with mobility 350 km/h. The rayleighchan, a Matlab function, leads to an initial delay of the generated channel, even if we set the delay of the direct path zero. Figs. 7 depict this phenomenon and we must compensate it in [1].

Note that the PA-Preamble timing we get by the above method has an offset to the real PA-Preamble timing due to multipath and noise effects. We will handle these problems in fine timing synchronization.

2) Estimation of Fractional Carrier Frequency Offset: We attempt an ML estimation of δ from it. It turns out that a truly ML estimation is quite complex because $\mathbf{T}_{576}$ is not circulant. However, if the coarse timing lands us in the CP and if we sacrifice the available signal power in the CP, then

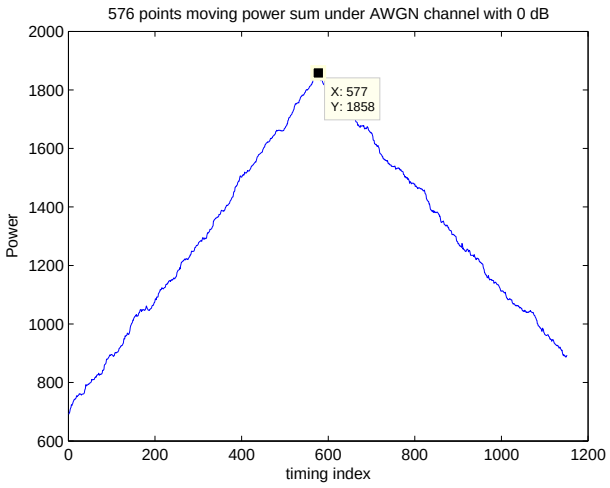

Fig. 4. 576 points power sum under AWGN in 0 dB [1].

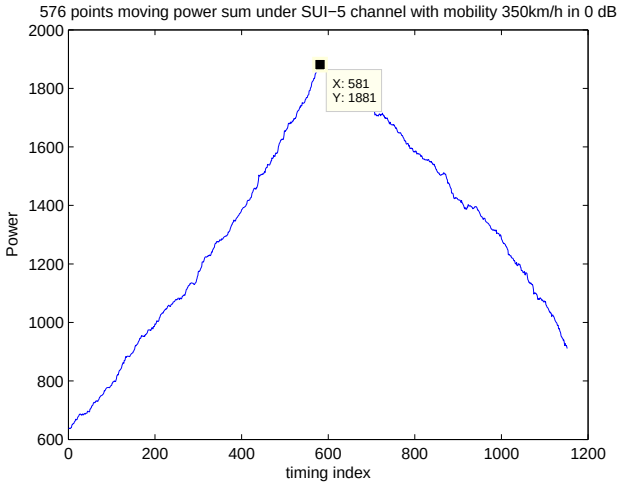

Fig. 5. 576 points power sum under SUI-5 at mobility 350 km/h in 0 dB [1].

we can obtain a reduced-complexity solution. Let $\mathbf{y}_{512}$ denote the received PA-Preamble symbol after removal of the CP. It is given by

$$\mathbf{y}_{512} = \mathbf{\Gamma}(\delta) \cdot \mathbf{T}_{x_n} \cdot \mathbf{h} + \eta, \tag{1}$$

where $\mathbf{x}_n = [x_0, x_1, ..., x_{511}]'$ (the transmitted PA-Preamble symbol), $\mathbf{T}_{x_n}$ is a 512×512 circulant matrix given by

$$\mathbf{T}_{x_n} = \begin{bmatrix} x_0 & x_{511} & x_{510} & x_{509} & . & . & . & x_2 & x_1 \\ x_1 & x_0 & x_{511} & x_{510} & . & . & . & x_3 & x_2 \\ . & x_1 & x_0 & x_{511} & . & . & . & x_3 & x_2 \\ x_{63} & . & x_1 & . & . & . & . & . & . \\ . & x_{63} & . & . & . & . & . & . & . \\ . & . & . & . & . & . & . & x_{510} & . \\ x_{509} & . & . & . & . & . & . & x_{511} & x_{510} \\ x_{510} & x_{509} & . & . & x_{63} & . & . & x_0 & x_{511} \\ x_{511} & x_{510} & x_{509} & . & . & x_{63} & . & x_1 & x_0 \end{bmatrix}, \tag{2}$$

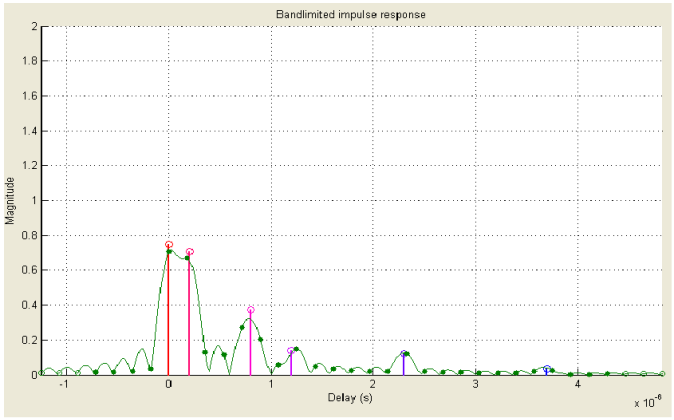

Fig. 6. Channel impulse response of PB channel [1].

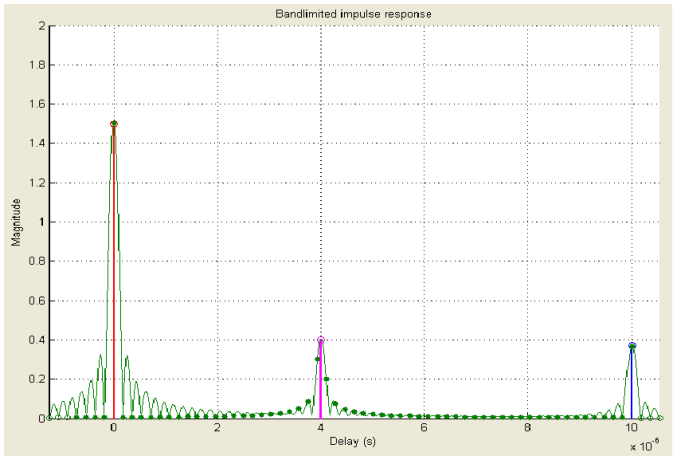

Fig. 7. Channel impulse response of SUI-5 channel [1].

$\mathbf{h}$ is the channel impulse response vector,

$$\mathbf{\Gamma}(\delta) = \begin{bmatrix} e^{-j\cdot\frac{2\pi}{512}\cdot\delta\cdot 0} & & & & 0 \\ & e^{-j\cdot\frac{2\pi}{512}\cdot\delta\cdot 1} & & & \\ & & . & & \\ & & & . & \\ 0 & & & & e^{-j\cdot\frac{2\pi}{512}\cdot\delta\cdot 511} \end{bmatrix}, \tag{3}$$

and η is an AWGN vector. Due to possibly incorrect identification of the PA-Preamble starting time from the coarse timing synchronization, there may be a circular shift of the elements in the $\mathbf{h}$ vector from their original positions.

Eq. (1) can then be rewritten as:

$$\begin{aligned} \mathbf{y}_{512} &= \mathbf{\Gamma}(\delta) \cdot \mathbf{F}^H \cdot \mathbf{F} \cdot \mathbf{T}_{x_n} \cdot \mathbf{F}^H \cdot \mathbf{F} \cdot \mathbf{h} + \eta & (4) \\ &= \mathbf{\Gamma}(\delta) \cdot \mathbf{F}^H \cdot (\mathbf{F} \cdot \mathbf{T}_{x_n} \cdot \mathbf{F}^H) \cdot (\mathbf{F} \cdot \mathbf{h}) + \eta & (5) \\ &= \mathbf{\Gamma}(\delta) \cdot \mathbf{F}^H \cdot \mathbf{D}_k \cdot \mathbf{H} + \eta, & (6) \end{aligned}$$

where $\mathbf{F}$ is the normalized 512×512 FFT matrix, $\mathbf{F}^H$ is the corresponding normalized IFFT matrix, $\mathbf{H}$ is the channel frequency response vector, and $\mathbf{D}_k$ is a diagonal matrix of the PA-Preamble sequence in the frequency domain, with k being the PA-Preamble index.

The likelihood function of $\mathbf{y}_{512}$ can be written as:

$$p(\mathbf{y}_{512}|\delta,\mathbf{H},k)=\frac{1}{(2\pi\sigma_\eta^2)^{512}}\cdot\exp(-\frac{1}{2\sigma_\eta^2}\|\mathbf{y}_{512}-\mathbf{\Gamma}(\delta)\cdot\mathbf{F}^H\cdot\mathbf{D}_k\cdot\mathbf{H}\|^2 \tag{7}$$

in the likelihood function, there are three unknowns, namely δ, $\mathbf{H}$ and k. The ML estimation is thus given by

$$\begin{aligned}
&\arg\max_{\delta,\mathbf{H},k} p(\mathbf{y}_{512}|\delta,\mathbf{H},k) && (8)\\
&= \arg\min_{\delta,\mathbf{H},k} \|\mathbf{y}_{512}-\mathbf{\Gamma}(\delta)\cdot\mathbf{F}^H\cdot\mathbf{D}_k\cdot\mathbf{H}\|^2 && (9)\\
&= \arg\min_{\delta,k}\min_{\mathbf{H}|\delta,k} \|\mathbf{y}_{512}-\mathbf{\Gamma}(\delta)\cdot\mathbf{F}^H\cdot\mathbf{D}_k\cdot\mathbf{H}\|^2 && (10)\\
&\Rightarrow \arg\min_{\delta,k} \|\mathbf{y}_{512}-\mathbf{\Gamma}(\delta)\cdot\mathbf{F}^H\cdot\mathbf{D}_k\cdot\mathbf{D}_k^H\cdot\mathbf{F}\cdot\mathbf{\Gamma}^H(\delta)\cdot\mathbf{y}_{512}\|^2 && (11)
\end{aligned}$$

Note that (11) arises because the inner minimization of (10) is achieved with $\mathbf{H}=\mathbf{D}_k^H\cdot\mathbf{F}\cdot\mathbf{\Gamma}^H(\delta)\cdot\mathbf{y}_{512}$ as can be obtained via standard least-square estimation technique. Since $\mathbf{D}_k\cdot\mathbf{D}_k^H$ is the same whatever for add k, we cannot solve for the optimal k from (3.14), but must find it through above other means, In addition, the minimization target in (3.14) is a function of δ only. Thus it is equivalent to:

$$\begin{aligned}
&\arg\min_{\delta} \|\mathbf{y}_{512}-\mathbf{\Gamma}(\delta)\cdot\mathbf{F}^H\cdot\mathbf{D}_k\cdot\mathbf{D}_k^H\cdot\mathbf{F}\cdot\mathbf{\Gamma}^H(\delta)\cdot\mathbf{y}_{512}\|^2 && (12)\\
&= \arg\min_{\delta} \|[I-\mathbf{\Gamma}(\delta)\cdot\mathbf{F}^H\cdot\mathbf{D}_k\cdot\mathbf{D}_k^H\cdot\mathbf{F}\cdot\mathbf{\Gamma}^H(\delta)]\cdot\mathbf{y}_{512}\|^2 && (13)\\
&= \arg\min_{\delta} \mathbf{y}_{512}^H\cdot[I-\mathbf{\Gamma}(\delta)\cdot\mathbf{F}^H\cdot\mathbf{D}_k\cdot\mathbf{D}_k^H\cdot\mathbf{F}\cdot\mathbf{\Gamma}^H(\delta)]^2\cdot\mathbf{y}_{512} && (14)\\
&= \arg\max_{\delta} \mathbf{y}_{512}^H\cdot\mathbf{\Gamma}(\delta)\cdot\mathbf{F}^H\cdot\mathbf{D}_k\cdot\mathbf{D}_k^H\cdot\mathbf{F}\cdot\mathbf{\Gamma}^H(\delta)\cdot\mathbf{y}_{512} && (15)\\
&= \arg\max_{\delta} \gamma^{\mathbf{H}}(\delta)\cdot[\mathbf{Y}^{\mathbf{H}}\cdot\mathbf{F}^{\mathbf{H}}\cdot\mathbf{D}_{\mathbf{k}}\cdot\mathbf{D}_{\mathbf{k}}^{\mathbf{H}}\cdot\mathbf{F}\cdot\mathbf{Y}]\cdot\gamma(\delta) && (16)
\end{aligned}$$

where $\gamma(\delta)=[\exp(-\mathbf{j}\cdot\frac{\mathbf{2\pi}}{\mathbf{512}}\cdot\delta\cdot\mathbf{0}),\exp(-\mathbf{j}\cdot\frac{\mathbf{2\pi}}{\mathbf{512}}\cdot\delta\cdot\mathbf{1}),...,\exp(-\mathbf{j}\cdot\frac{\mathbf{2\pi}}{\mathbf{512}}\cdot\delta\cdot\mathbf{511})]^T$, and $\mathbf{Y}$ is a diagonal matrix whose ith diagonal element is the ith element in $\mathbf{y}_{512}$.

Note that since $\mathbf{D}_k\cdot\mathbf{D}_k^H$ is diagonal, $\mathbf{W}\triangleq\mathbf{F}^H\cdot\mathbf{D}_k\cdot\mathbf{D}_k^H\cdot\mathbf{F}$ is a circulant matrix. Indeed, because $\mathbf{D}_k\cdot\mathbf{D}_k^H$ is nearly periodic (with mostly every other element equal to 1 while others equal to zero) along the diagonal, $\mathbf{W}$ is nearly tri-diagonal and so is $\mathbf{M}$. The three diagonal sums are given by

$$\begin{aligned}
M_0 &= \sum_{i=0}^{511} w_{i,i}\cdot|y_{i,i}|^2, && (17)\\
M_{-256} &= \sum_{i=256}^{511} y_{i,i}^H\cdot w_{i,i-256}\cdot y_{i-256,i-256}, && (18)\\
M_{256} &= \sum_{i=256}^{511} y_{i-256,i-256}^H\cdot w_{i-256,i}\cdot y_{i,i}, && (19)
\end{aligned}$$

where $y_{i,i}$ is the ith diagonal element of $\mathbf{Y}$, and $w_{i,i}$ is the ith diagonal of $\mathbf{W}$. We utilize the mathematic format of FFT of these three dominant terms to estimate fractional carrier frequency (FCFO) by finding the peak value and derive as $\delta=-\frac{1}{\pi}\arctan\frac{\Im\{M_{256}\}}{\Re\{M_{256}\}}$.

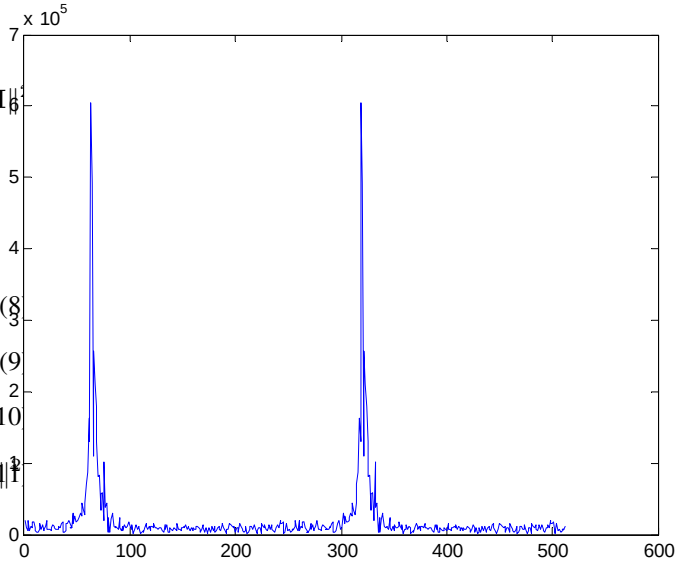

Fig. 8. The estimated CIR with accurate ICFO, 8, compensating and correct PA-Preamble index, 1, under PB channel with 120 km/h, 0dB in SNR.

3) Joint Estimation of Integral CFO, PA-Preamble Index, Channel Estimation and Fine Timing Offset: CFO is separated into two parts, FCFO and integral carrier frequency offset (ICFO), and the former have been estimation in the previous subsection. We can expect that the power of channel impulse response (CIR), the inverse fourier transform of $\mathbf{H}$ as obtained in (11), will be more concentrated if we compensate with the accurate CFO and use the correct one of the three possible PA-Preamble symbols. For example, Figs. 8 and 9 depict two CIRs obtained from using a combination of correct CFO and correct PA-Preamble index and from using a combination of incorrect values. The simulation environment we choose in Figs. 8 and 9 is PB channel, 120 km/h, 0 dB in SNR, the correct ICFO 8, the correct PID 1 (10-MHz), the wrong ICFO 6, and the wrong PID 0 (5-MHz). We consider there are 21 possible ICFO explained in the Eq. (20), 3 PA-Preamble symbols and 256 timing locations in CIR, therefore, $21\times3\times64=16128$ candidates in total. The method we use here is to do 64 points sum of squared CIR for these candidates and find out one which has the maximum of power sum. The reason why we choose the searching range of ICFO from -20 to 20 is that we assume a maximum mismatch of the local oscillator frequency of ±80 ppm, so that a wireless system with carrier frequency 2.5 GHz ±18.28 subcarriers of offset at the 10.9375 kHz subcarrier spacing of IEEE 802.16m, as given by

$$\frac{2.5G\cdot80ppm}{10.94K}\approx18.28. \tag{20}$$

For the fine timing, since it is reasonable to assume that the CIR is mostly concentrated over a length not exceeding the CP length, we decide the ICFO, the PA-Preamble index and the fine timing offset by finding which one of all candidates has the maximum power sum over the CP length.

4) Overall Block Diagram: In summary, Fig. 10 shows the resulting overall block diagram of the derived initial DL synchronization method.

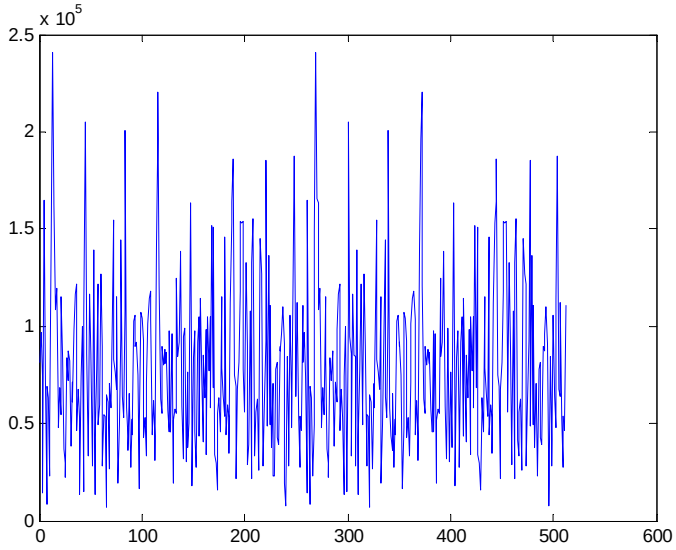

Fig. 9. The CIR with the inaccurate ICFO, 6, compensating and incorrect PA-Preamble index, 0, under PB channel with 120 km/h, 0dB in SNR.

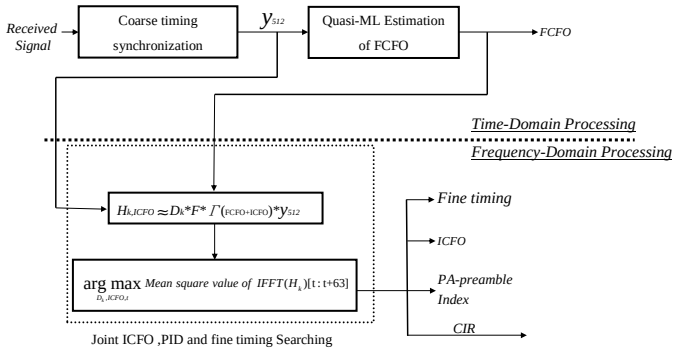

Fig. 10. Block diagram of algorithm for initial DL synchronization [1].

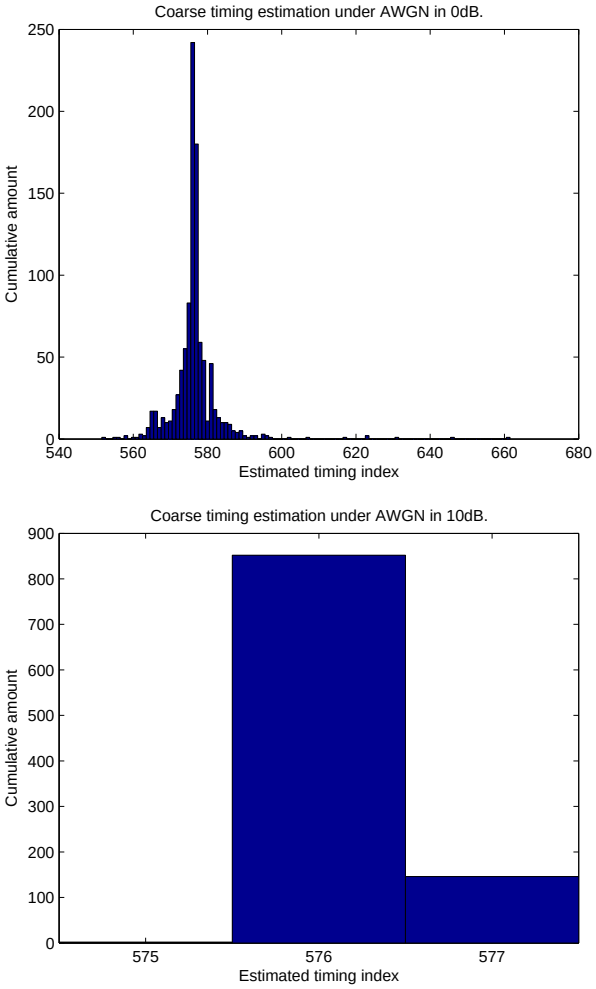

Fig. 11. Histograms of coarse timing estimation under AWGN channel in different SNR.

4. Fixed-Point Implementation of Initial Downlink Synchronization

1. Floating-Point Simulation Results

In this section, we present the floating-point simulation results for C program, the system parameters for our simulation are defined in Table I, and we modify the C code form Matlab code to do simulation under different channel environments and velocities. The power delay profiles (PDPs) used include Standford University Interim (SUI) [17] and Pedestrian B (PB) [9]. Our SNR values are from 0 to 20 dB, which is the ratio of the variance of PA-Preamble samples to that of the noise samples. The mobile velocity is from 0 to 120 km/h, and the carrier frequency offset (CFO) is 8.42884 subcarrier spacings, so the integral carrier frequency offset (ICFO) is 8 subcarrier spacings and fractional carrier frequency offset (FCFO) is 0.42884 subcarrier spacings. The simulation results are obtained with runs of simulation for each difference SNR.

1) Coarse Timing Estimation: The target of coarse timing estimation is to find a staring timing sample for PA-Preamble, and the correct PA-Preamble time index is 576 in our simulation. Figs. 11 shows the histograms of coarse timing samples under AWGN channel at 0 dB and 10 dB, and it is clear that the higher SNR gives a better performance. It is seen that SNR affect the performance more than the velocity, Figs. 12 and 13 illustrate the histograms under PB at similar SNR values and velocities. The correct timing index under SUI-1 and PB channel is 583, where the 6 samples difference with AWGN is due to the property of the Matlab function for simulating the multipath channel as discussed in chapter 3. The accuracy of coarse timing estimation affect MSE of FCFO estimation.

2) Fractional CFO Estimation: Figs. 14 to 16 show the mean square error of fractional carrier frequency offset estimation under AWGN, SUI-1, SUI-3 and PB channel at different mobile velocities. The simulation results perform similar to results of reference [2], because our SNR definition is the same with [2].

3) Joint Estimation of Integral Carrier Frequency ORset, PID and Fine Timing: In this subsection, we present the simulation of ICFO estimation results in Figs. 17 to 18. The simulation parameters are:

- ICFO: 8 subcarrier spacings.
- PA-Preamble index (PID): 1 (10MHz).
- Channel models: AWGN, SUI1, PB.
- Mobile velocities: 10 km/h, 90 km/h.

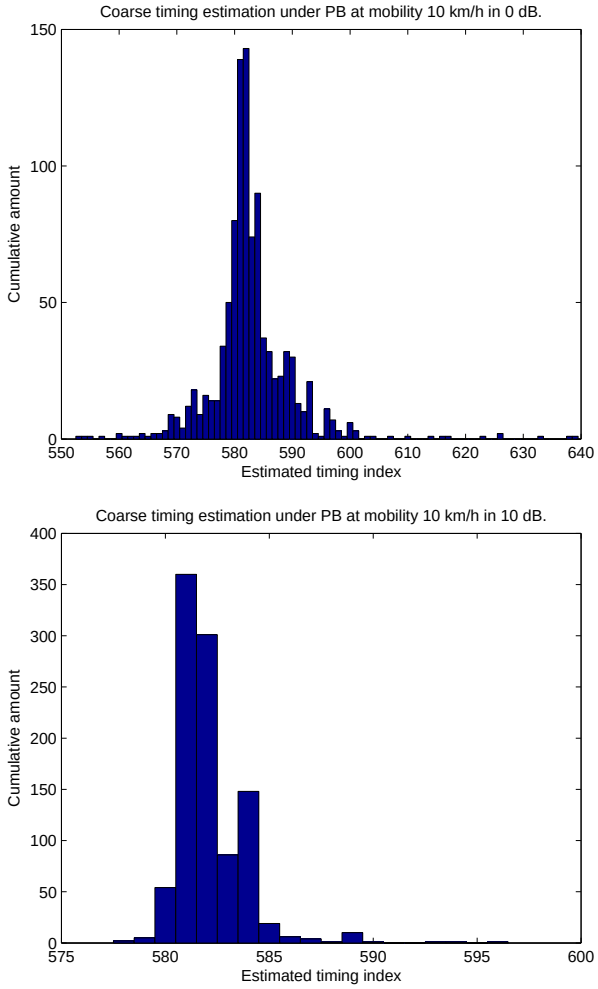

Fig. 12. Histograms of coarse timing estimation under PB channel in different SNR value for a velocity of km/h.

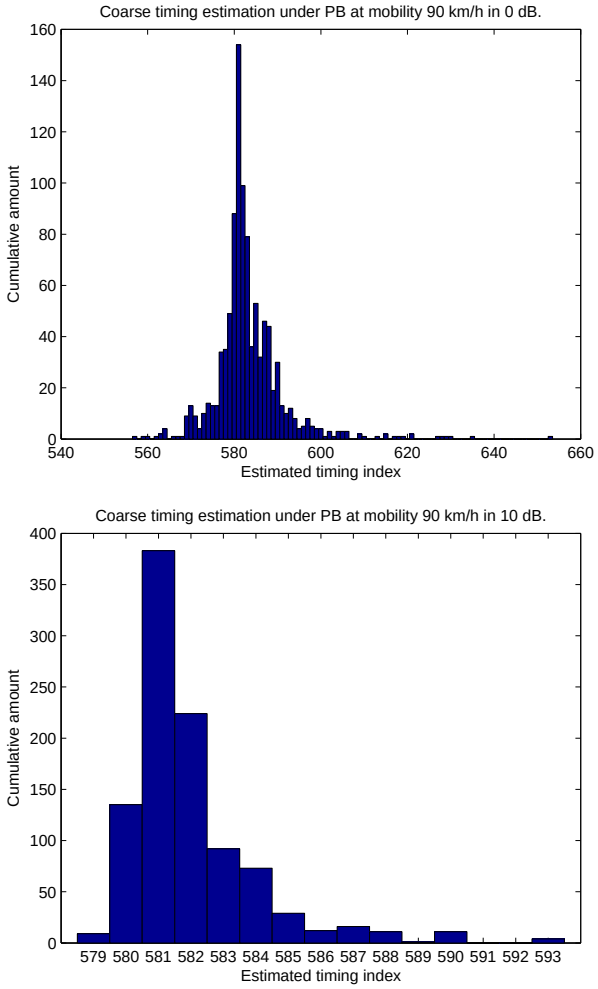

Fig. 13. Histograms of coarse timing estimation under PB channel in different SNR value for a velocity of 90 km/h.

TABLE II

THE ERROR RATE OF TIMING ESTIMATION.

	AWGN	PB_10km	PB_90km	SUI1_10km	SUI1_90km
0 dB	0.013	0.113	0.118	0.011	0.021
10 dB	0	0.001	0.005	0	0
20 dB	0	0	0	0	0

- SNR value: 0 dB, 10 dB.

They illustrates the histograms under AWGN and SUI-1 channels at SNR values of 0 and 10dB and velocities 10 and 90 km/h, respectively. Figs. 19 to 20 show the histograms of PID detection under AWGN and SUI-1 channels at similar SNR and velocity setting. They show that the ICFO and PID estimation are quite accurate at different SNR and channel condition. Figs. 21 illustrates the performance of fine timing estimation under AWGN, SUI-1 and PB channels in 0 dB, 10 dB, and 20 dB of SNR at speeds 10 km/h and 90 km/h, respectively. We define "error" is that the estimated timing index does not locate between the boundary of delay spread and the right end of CP, then we can calculate the error rate, show in Table II. The simulation results of overall timing estimation is similar with reference [1].

2. *Fixed-Point Implementation*

Usually, we use floating-point processing to verity the performance of the algorithms. But fixed-point processing improves power efficiency, speed and hardware cost. Hance large-volume practical implementation normally employ fixed-point processing. In this section, we present the initial down-link synchronization algorithm implementation in fixed-point processing using TI's TMS320C6416T DSP. We also try to utilize coding style and intrinsic functions to reduce cycle counts on DSP.

Fig. 22 shows the fixed-point data formats used in the different places in our algorithm, where Qx.y means there are x bits before the binary points and y bits after. In our case, x+y = 15 because the sign takes 1 bit. We choose Q7.8 to be the data format at many places, because coarse timing estimation needs to accumulate the squared norm of data. The Q7.8 format can avoid overflow in coarse timing estimation. In fact, we find that the Q7.8 data format has enough accuracy for our experiment. In the following subsections, we discuss the details of the blocks in the algorithm.

1) Coarse Timing Estimation and Removal of Cycle Prefix: The first step in the procedure is coarse timing estimation to

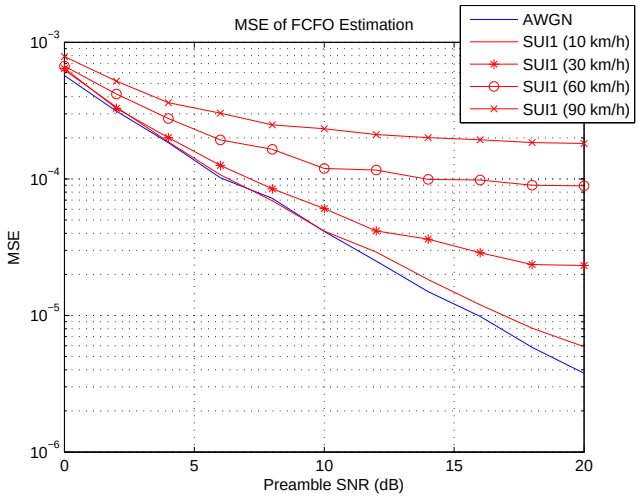

Fig. 14. Mean square error of FCFO estimation under SUI-1 and AWGN channels.

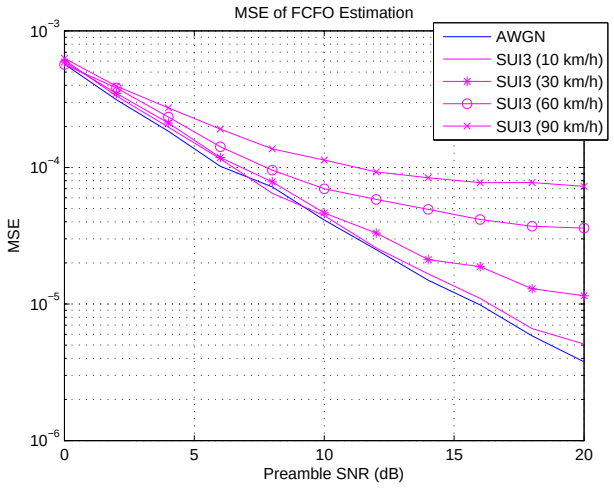

Fig. 15. Mean square error of FCFO estimation under SUI-3 and AWGN channels.

find the approximate location of PA-Preamble. Figs. 3 shows our signal structure, where we compute the signal power in a finite window size and slide the window. According to the IEEE 802.16m standard, the PA-Preamble magnitude is boosted by a factor of 1.9216, 2.6731 or 4.6511 compared to regular data signal. To the maximum power position should be a good indicator of what the PA-Preamble is. After coarse timing estimation, we remove the CP from the 576 points starting at the estimated point to get 512 points of data. Actually, because the estimated point by coarse timing estimation may be located within the CP, what we in fact do is to take the first 512 points starting from the coarse timing point, which is equivalent to discard the last 64 point of the 576 points, because it is more probable to get a complete PA-Preamble this way.

2) Fractional Carrier Frequency Offset Estimation and Compensation: FCFO estimation is the second step in the procedure. Fig. 23 shows that we correlate the first 256 points and the last 256 points of PA-Preamble to calculate the FCFO,

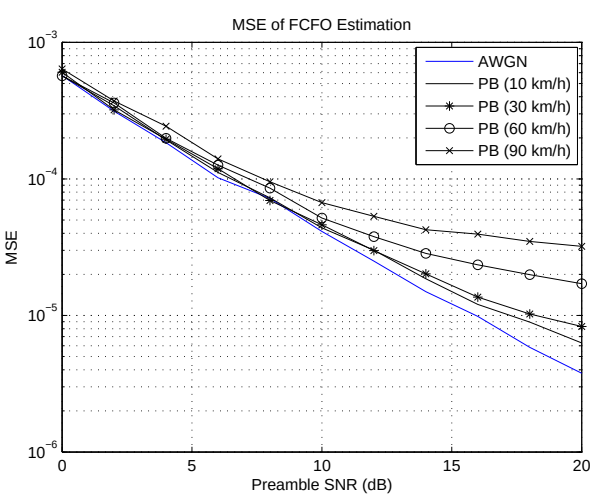

Fig. 16. Mean square error of FCFO estimation under PB and AWGN channels.

which is obtained as the arc-tangent of the correlation. For efficiency in DSP implementation, we use a lookup table to implement the $\arctan()$ function. For dynamic range, we create a table for the $\arcsin()$ function to estimate the FCFO in place of a table of the $\arctan()$ function. The table contains 2048 entries uniformly spanning the range $[\sin 0, \sin 0.25\pi)$, and the table entries are normalized with respect π so that they span the range $[0, 0.25)$.

In frequency offset compensation, we create two lookup tables for the $\sin()$ and the $\cos()$ functions, each containing 2048 entries uniformly spanning the range $[0, \pi \div 2)$. Since the values of $\sin()$ and $\cos()$ are from -1 to 1, we choose Q.15 as the data format. Hence, when the FCFO is compensated, the data format becomes Q7.24. Then we change the data format from Q7.24 to Q7.8 in order to avoid overflow in ICFO estimation.

3) Integer Carrier Frequency Offset Estimation and PID Detection: The last step of the procedure is ICFO estimation and PID detection. For this, we operate in the frequency domain. Since ICFO is just a shift in the subcarrier indexes in the frequency domain, it is relatively simple to implement in C program. According to (11), we calculate the channel frequency response and transform it to the time domain. Since the CIR length is supposed be not exceeding 64 points, we can assume that the correct choice of ICFO and PID should yield the maximum squared value, sum for the resulting CIR. The flow chart is shown in Fig. 24.

3. Fixed-Point Simulation Results

In this section, we show the fixed-point simulation results and compare them with the floating-point simulation results under different channel models. All simulation parameters and environments are the same as those given in previous section.

1) Coarse Timing Estimation: Fig. 25 shows the histograms of coarse timing samples under AWGN channel with 0 and 10 dB of SNR. In Figs. 26 and 27, we show the histograms under PB channel at SNR values of 0 and 10 dB and velocities of

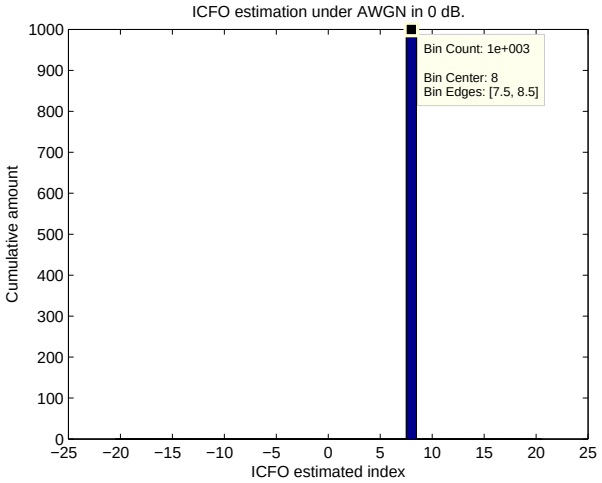

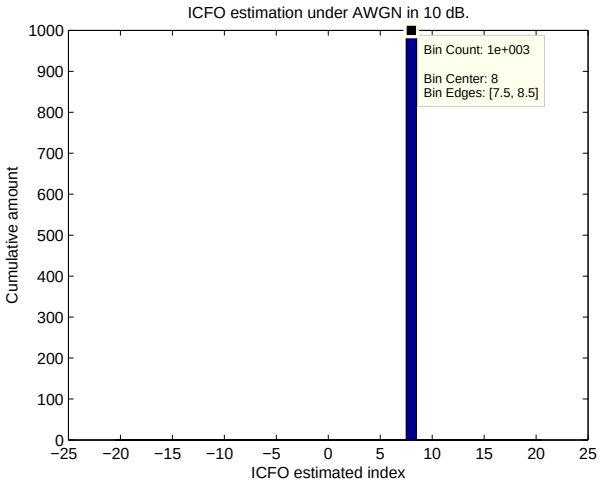

Fig. 17. Histograms of integer CFO estimation under AWGN channel in different SNR values.

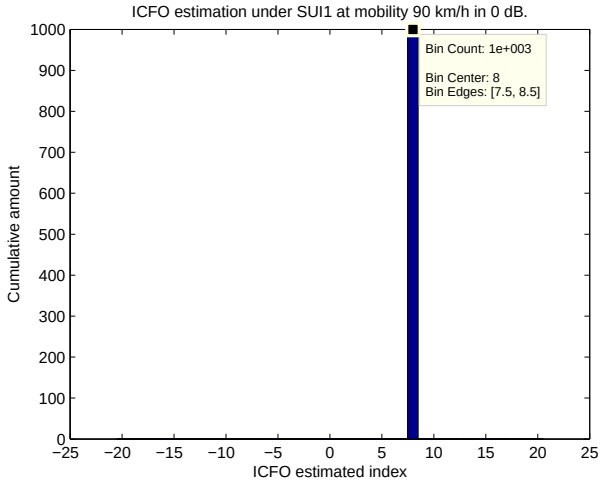

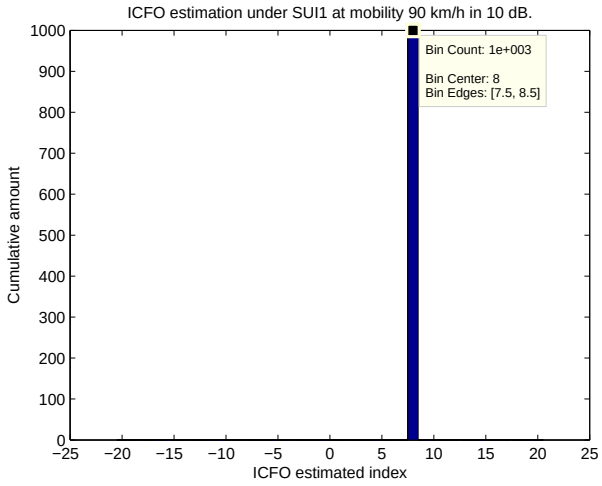

Fig. 18. Histograms of integer CFO estimation under SUI-1 channel in different SNR values at a velocity of 90 km/h.

10 and 90 km/h, respectively. Note that the simulation results are almost the same with the floating-point results shown in Figs. 11 to 13.

2) Fractional CFO Estimation: Figs. 28 to 30 show the MSE of fractional CFO estimation in SUI-1, SUI-3, PB and AWGN channels at speeds 10, 30, 60 and 90 km/h with fixed-point and floating-point computation. From the simulation results, we can see that the performance curves for floating-point and fixed-point computation are only a little different.

3) Joint Estimation of Integral Carrier Frequency Offset, PID and Fine Timing: Figs. 31 shows the estimation performance of integer CFO under AWGN channel at SNR of 0 and 10 dB, respectively, and Figs. 32 shows the estimation performance of PID under AWGN channel at SNR of 0 and 10 dB. Table III shows the error rate of timing estimation. We can see that floating-point and fixed-point implementation have the same results shown in Figs. 17 to 32, in all cases simulated.

TABLE III

THE ERROR RATE OF TIMING ESTIMATION.

	AWGN	PB_10km	PB_90km	SUI1_10km	SUI1_90km
0 dB	0.017	0.121	0.155	0.031	0.025
10 dB	0	0.002	0.001	0	0
20 dB	0	0	0	0	0

4. Speeding Up of DSP Implementation

In this section, we discuss how to reduce cycle counts in DSP implementation. The optimization techniques used include compiler option, intrinsic functions and DSP library function. We set the level of optimization of compiler option to -o3, which performs software pipelining and loop optimizations, and we do not perform loop unrolling ourselves. In the following, we concentrate the discussion on the use of intrinsic functions and DSP library functions in the function blocks.

1) Speeding Up of Coarse Timing Estimation: Calculating the magnitude-square of a complex number needs two multiplication, so accumulating 576 magnitude-squares for 1152 time position would require $576 \times 2 \times 1152 = 1,327,104$ multiplications. However, most of accumulated quantities appear repeatedly across successive time positions as shown in Fig. 33. Using this fact, we may compute the sum of magnitude-squares as

$$Power(N+1) = Power(N) - R(N) + R(N+576), \quad (21)$$

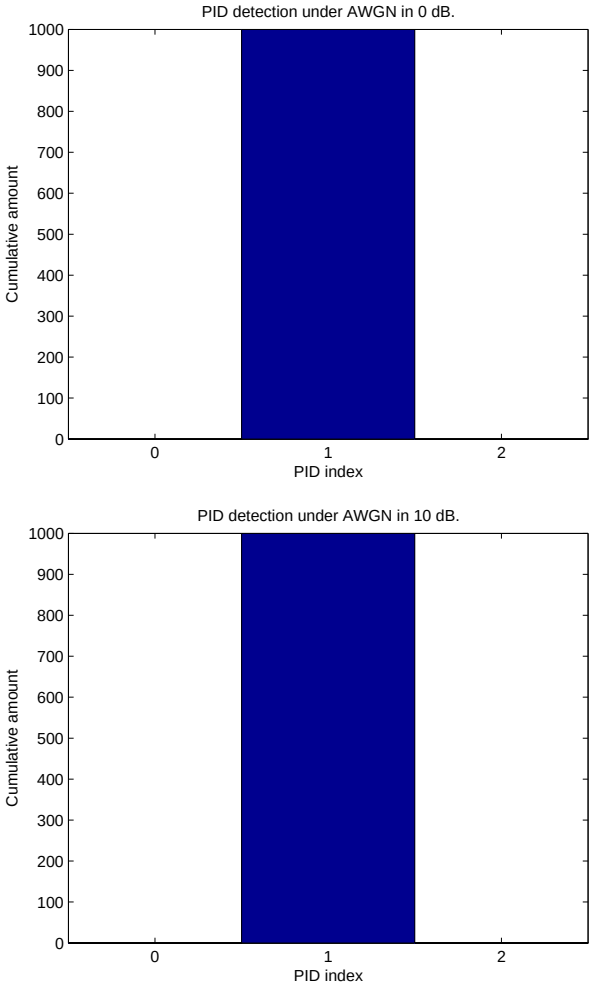

Fig. 19. Histograms of PID detection under AWGN channel in different SNR values.

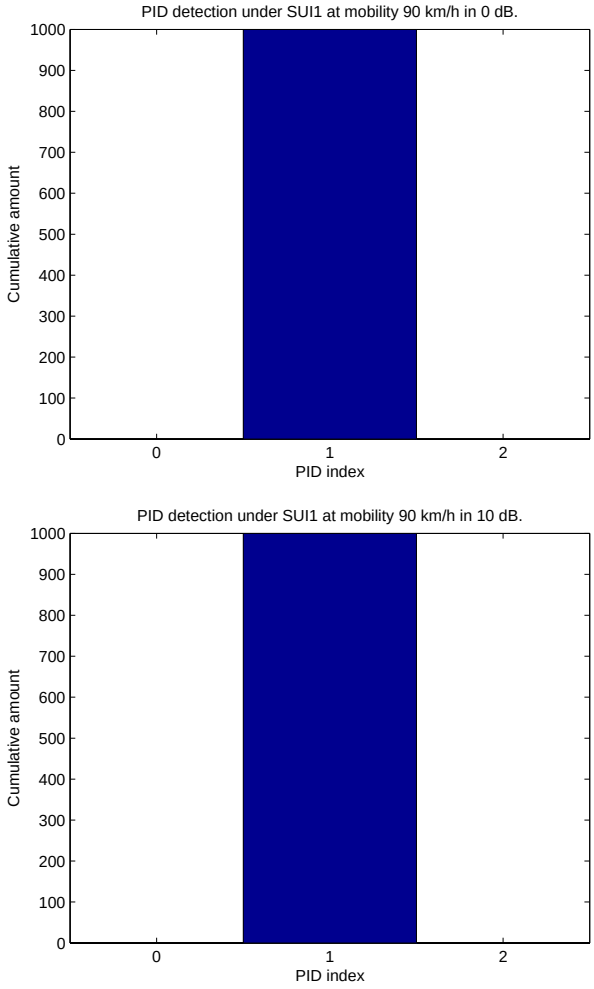

Fig. 20. Histograms of PID detection under SUI-1 channel in different SNR values at a velocity of 90 km/h.

$$Power(0) = \sum_{n=0}^{575} R(n), \tag{22}$$

where $R(N)$ is the magnitude-squares of the received signal sample at time N and $Power(N)$ is the sum as indicated in Fig. 33.

The compiler automatically utilizes the assembly instruction **MPY2** that computes two 16×16 multiplication in parallel. Hence, the coarse timing estimation needs about $576 \times 2 + 1152 \times 4 = 5760$ multiplications. According to Table IV, the efficiency of the coarse timing estimation is $(5760 \div 4 \div 7861) \times 100 = 18.3\%$, and Table V shows the cycle counts for compiler option of optimization level 1, the efficiency is $(5760 \div 2 \div 57588) \times 100 = 5\%$. The exection time of optimization level 1 is worse than optimization level 3 since the optimization level 1 does not performs loop unrolling, software-pipleining and call assembly instruction **MPY2**.

TABLE IV
COARSE TIMING ESTIMATION RESULTS FOR OPTIMIZATION LEVEL 3

Functions	Avg. Clock Cycles
Main Loop	7722
Initial Loop	139
Maximum PowerLevel	4756

TABLE V
COARSE TIMING ESTIMATION RESULTS FOR OPTIMIZATION LEVEL 1

Functions	Avg. Clock Cycles
Main Loop	41448
Initial Loop	16140
Maximum PowerLevel	37026

2) Using DSP Library Function for FFT and IFFT [18]: TI supplies a DSP library that contains the FFT/IFFT function `DSP_fft16x16r()` that implements a cache-optimized complex forward mixed radix FFT with scaling, rounding and digit reversal. The input data x[], output data y[] and coefficients w[] are 16-bit numbers. The output is returned in the array y[] in normal order. Each complex value is stored as interleaved 16-bit real and imaginary parts. The code uses a special ordering of FFT coefficients (also called twiddle factors). This DSP library function takes $\lceil \log_4(nx) - 1 \rceil \times (\frac{5}{4} \times nx + 25) + \frac{5}{4} \times nx + 26$ cycles and the codesize is 868 bytes, where nx is FFT size.

3) Speeding Up of ICFO, PID, Fine Timing Estimation: In integer CFO estimation, we utilize the signal structure

TABLE VI

ICFO, PID, FINE TIMING ESTIMATION RESULTS FOR OPTIMIZATION LEVEL 3

Functions	Avg. Clock Cycles
Sum of CIR	75411
CIR Computation	33705
MaxFixed	33453
Others	6042

TABLE VII

ICFO, PID, FINE TIMING ESTIMATION RESULTS FOR OPTIMIZATION LEVEL 1

Functions	Avg. Clock Cycles
Sum of CIR	406602
CIR Computation	326970
MaxFixed	547848
Others	340204

in the frequency domain, hence we need not compute the CIR the corresponding with PA-Preamble subcarrier is 0. Furthermore, we use the same method with coarse timing estimation to calculate the sum of CIR. Therefore, it is needs $216 \times 2 \times 3 \times 21 = 27,216$ multiplications to compute the CIR and $(64 \times 2 + 256 \times 4) \times 3 \times 21 = 72,576$ multiplications to compute the sum of CIR.

According to Table VI, the efficiency of sum of CIR is $(72576 \div 4 \div 75411) \times 100 = 24.1\%$ and the efficiency of CIR computation is $(27216 \div 2 \div 33705) \times 100 = 40.4\%$. Table VII shows the cycle counts for compiler option of optimization level 1, the efficiency of sum of CIR is $(72576 \div 2 \div 406602) \times 100 = 8.9\%$, and the efficiency of CIR computation is $(27216 \div 2 \div 326970) \times 100 = 4.16\%$.

5. DSP Optimization Results

Table VIII shows the number of clock for each function used in the initial DL synchronization procedures, and number of clock cycles does not including TI library in this table. Obviously, IFFT function takes the most percentage of total cycles, because number of IFFT times is the 21 (ICFO candidates)$\times$3 (bandwidth) = 63 times, and IFFT function time positions would require about 14,000 cycles per time. The `DSP_fft16x16r()` function is already highly optimized. Table IX shows the number of clock cycles including and excluding memory access. Table X shows the code size of the program for different optimization levels. In our system, the clock frequency of TMS320C6416T DSP is 1 GHz, so the total execution time of initial DL synchronization procedures is 1.181 ms.

5. CONCLUSION

In this thesis, we first presented the overall procedure of initial DL synchronization of the IEEE 802.16m TDD system, and verified them through floating-point computation. Second, we implemented the initial DL synchronization to fixed-point computation and compared the performance with floating-point computation. Finally, we optimized procedure of initial DL synchronization on TI's C6416T digital signal processor.

TABLE VIII

DSP OPTIMIZATION RESULTS

Functions	Avg. Clock Cycles	Percent Total Cycles
Coarse Timing Estimation	10239	0.96
FCFO Estimation	5911	0.554
Compensation	2141	0.2
FFT	14046	1.318
IFFT	884394	82.963
ICFO Estimation	148611	13.941
Remove CP	668	0.063
Total cycles	1066010	100

TABLE IX

DSP OPTIMIZATION RESULTS WITH INCLUSION AND EXCLUSION OF MEMORY ACCESS

Total Cycles	Avg. Clock Cycles
Exclude Memory Access	1066010
Include Memory Access	1168531

TABLE X

CODE SIZE RESULTS

Program	Memory
Optimization Level 3 Program Code Size (-o3)	448.613 KB
Optimization Level 1 Program Code Size (-o1)	439.781 KB
Data Memory Size	327.68KB

In the procedure of initial DL synchronization, we used coarse timing estimation to estimate the PA-Preamble location, thus, we obtained the FCFO from the quasi-ML estimation. In the end, we utilized the characteristic of the power centralization of CIR to estimate the ICFO, PID and fine timing offset.

For DSP implementation, we chosen Q7.8 to be our data format, and verified the performance through simulation results is close to the floating-point computation. We used optimization techniques that including preamble character, intrinsic functions and DSP library function to reduce the computation time. According to Table VIII, if the clock frequency of TMS320C6416T DSP is 1 GHz, execution time of initial DL synchronization procedures is 1.181 ms.

REFERENCES

[1] Kai-Wei Lu, "Initial downlink synchronization for IEEE 802.16m," M.S. thesis, National Chiao Tung University, Hsinchu, Taiwan, R.O.C., February 2010.

[2] P. S. Wang, K. W. Lu, D. W. Lin, and P. Ting, "Quasi-maximum likelihood initial downlink synchronization for IEEE 802.16m," in *Proc. IEEE Int. Workshop Signal Processing Advanes Wirel. Commun.,* June 2011, pp. 506–510.

[3] Man-On Pun, Michele Morelli, and C.-C. Jay Kuo, "Maximum-likelihood synchronization and channel estimation for OFDMA uplink transmissions," *IEEE Trans. Commun.*, vol. 54, no. 4, pp. 726–736, Apr. 2006.

[4] Lior Eldar, M. R. Raghavendra, S. Bhashyam, Ron Bercovich, and K. Giridhar, "Parametric channel estimation for pseudo-random user-allocation in uplink OFDMA," in *IEEE Int. Conf. Commun.*, 2006, vol. 7, pp. 3035–3039.

[5] IEEE 802.16 Task Group m Draft 9, *Part 16: Air Interface for Fixed and Mobile Broadband Wireless Access Systems — Advanced Air Interface (working document)*. IEEE 802.16m, Oct. 6, 2010.

[6] K.-C. Hung and D. W. Lin, "Joint detection of integral carrier frequency offset and preamble index in OFDMA WiMAX downlink synchronization," in *Proc. IEEE Wireless Commun. Networking Conf.,* Mar. 2007, pp. 1959–1964.

[7] R. van Nee and R. Prasad, *OFDM for Wireless Multimedia Communications.* Boston: Artech House, 2000.

[8] P.H. Moose, "A technique for orthogonal frequency division multiplexing frequency offset correction," *IEEE Trans. Commun.,* vol. 42, no. 10, pp. 2908–2914, Oct. 1994.

[9] Y. Chunxuan, A. Reznik, G. Sternberg, Y. Shah, "On the secrecy capabilities of ITU Channels," in *IEEE Vehicular Technology Conference,* Oct. 2007, pp. 2030–2034.

[10] Sundance home page: http://www.sundance.com

[11] Texas Instruments, *TMS320C6000 CPU and Instruction Set Reference Guide.* Literature no. SPRU189F, Oct. 2000.

[12] Texas Instruments, *TMS320C6414T, TMS320C6415T, TMS320C6416T Fixed-Point Digital Signal Processors.* Literature no. SPRS226A, Mar. 2004.

[13] Texas Instruments, *Code Composer Studio User's Guide.* Literature no. SPRU328B, Feb. 2000.

[14] Texas Instruments, *TMS320C6000 Code Composer Studio Tutorial.* Literature no. SPRU301CI, Feb. 2000.

[15] Texas Instruments, *TMS320C6000 Programmer's Guide.* Literature no. SPRU198J, Apr. 2010.

[16] Texas Instrument, *TMS320C6000 Optimizing Compiler User Guide.* Literature no. SPRU187S, Mar. 2011.

[17] V. Erceg *et al*., "Channel models for fixed wireless applications," IEEE standards contribution no. IEEE 802.16.3c-01/29r4, July 2001.

[18] Texas Instrument, *TMS320C64x DSP Library Programmer's Reference.* Literature no. SPRU565B, Oct. 2003.

[19] J. J. van de Beek *et al.*, "ML estimation of time and frequency offset in OFDM systems," *IEEE Trans. Signal Processing,* vol. 45, no. 7, pp. 1800–1805, July 1997.

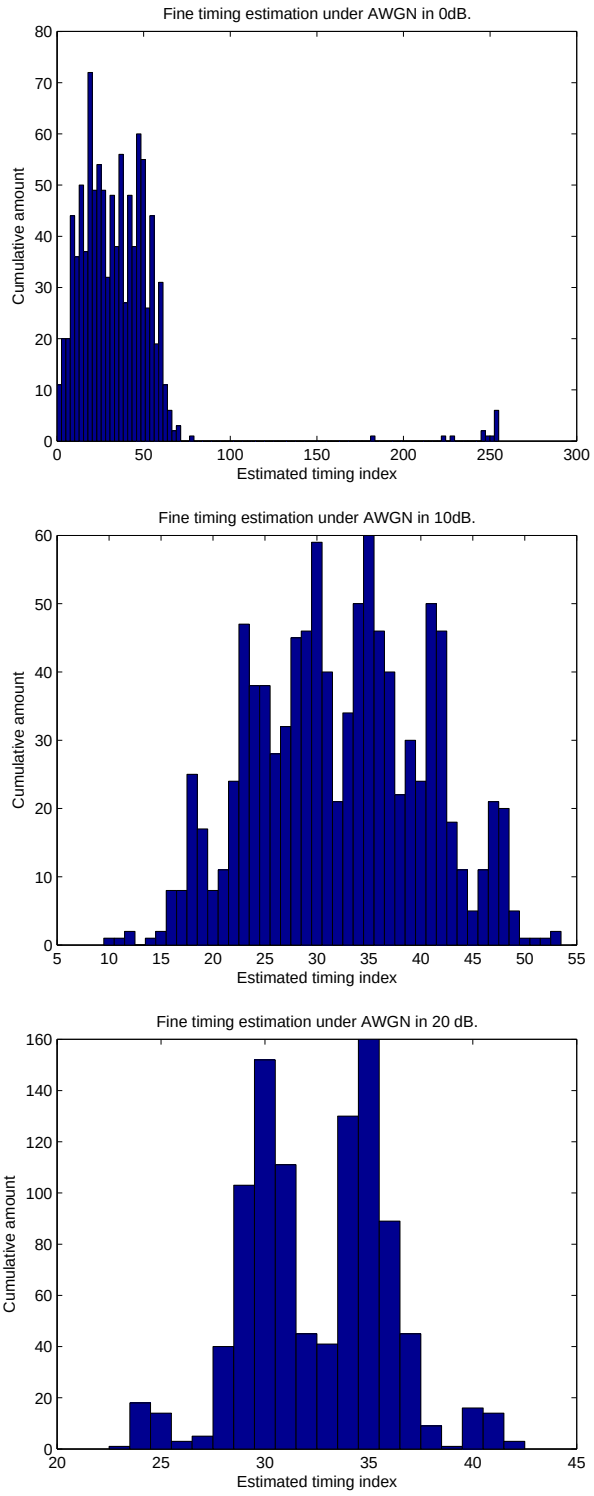

Fig. 21. Histograms of fine timing estimation under AWGN channel in the different SNR values.

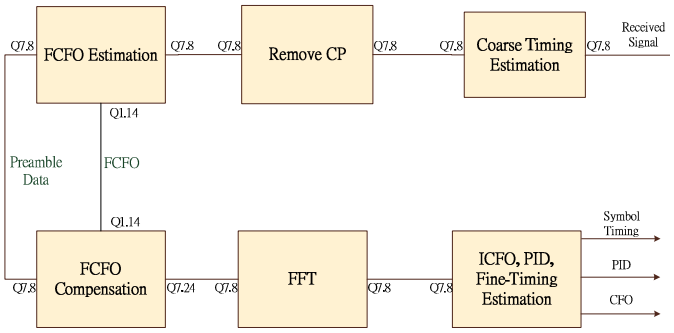

Fig. 22. Fixed-point data formats used in DSP implementation.

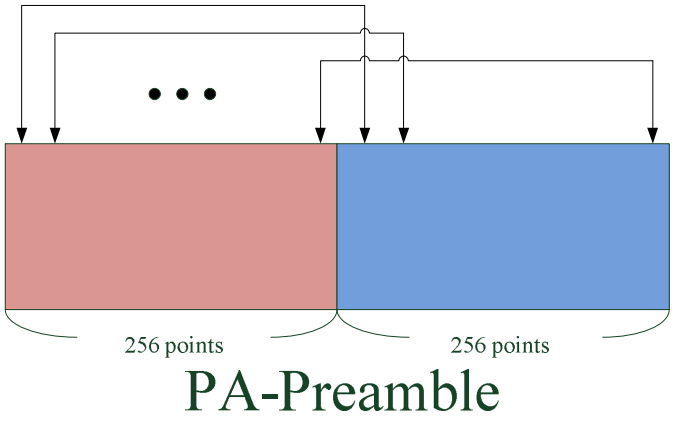

Fig. 23. Calculating the correlation in received PA-Preamble.

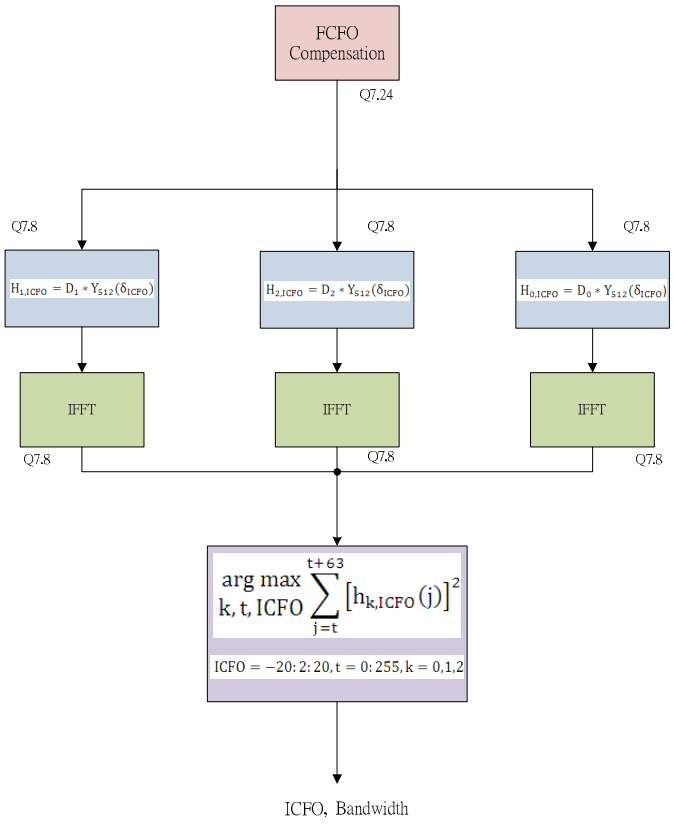

Fig. 24. ICFO estimation and PID detection flow chart.

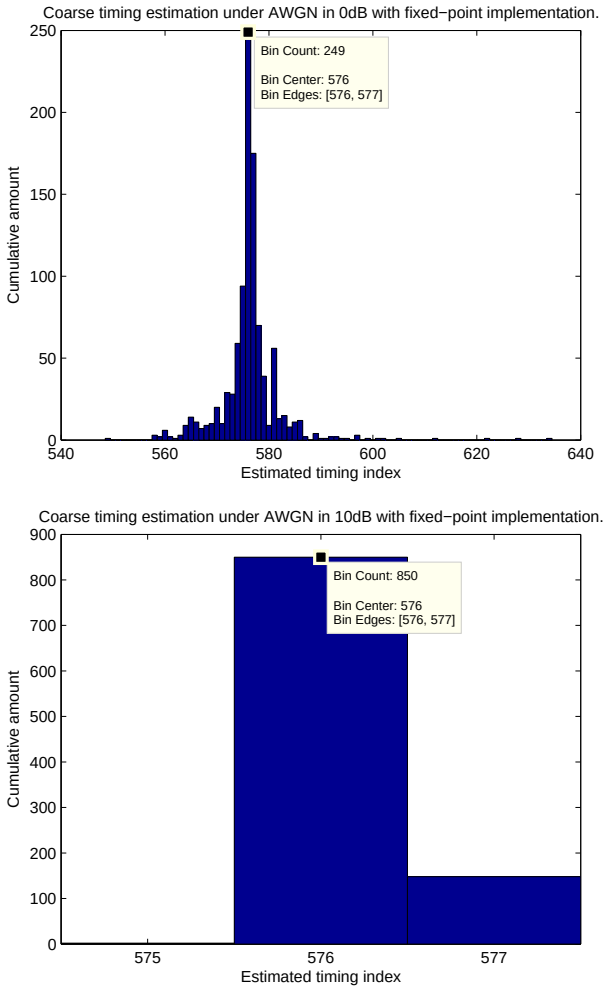

Fig. 25. Histograms of coarse timing estimation under AWGN channel in different SNR values.

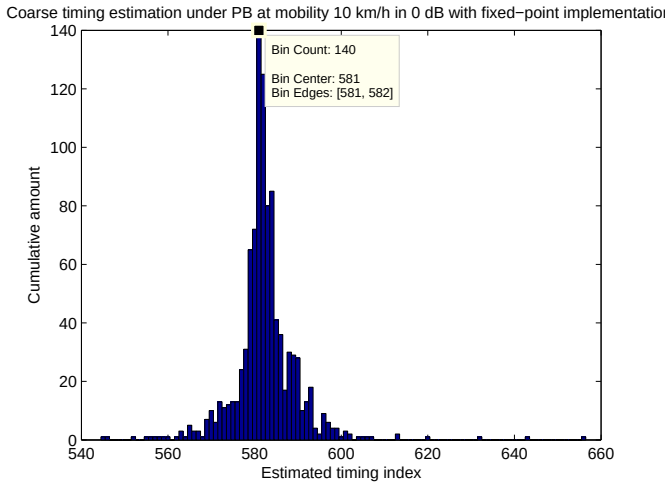

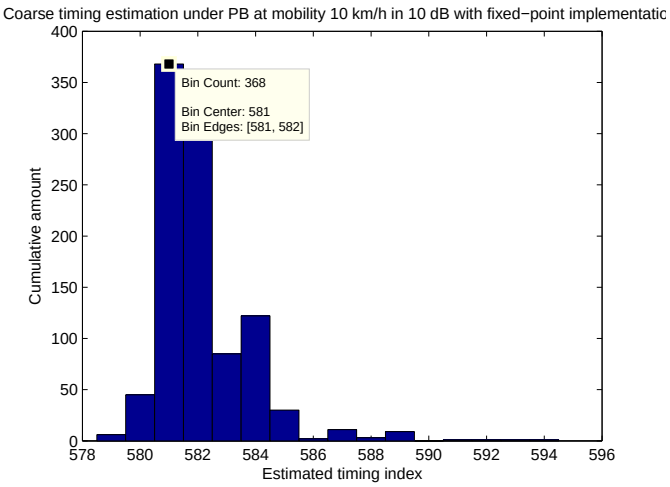

Fig. 26. Histograms of coarse timing estimation under PB channel in different SNR values at a velocity of 10 km/h.

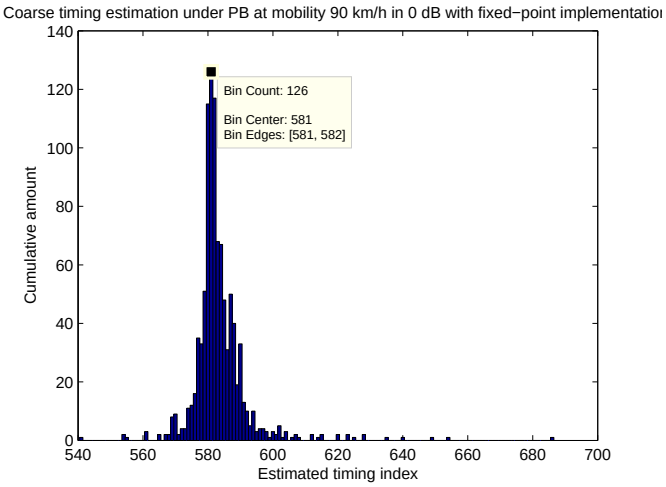

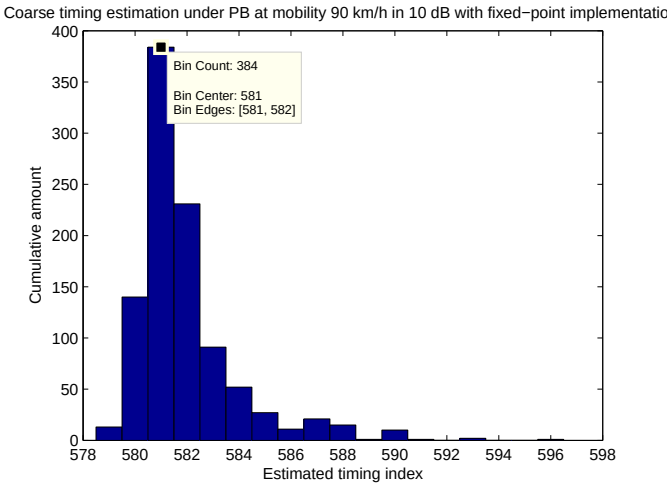

Fig. 27. Histograms of coarse timing estimation under PB channel in different SNR values at a velocity of 90 km/h.

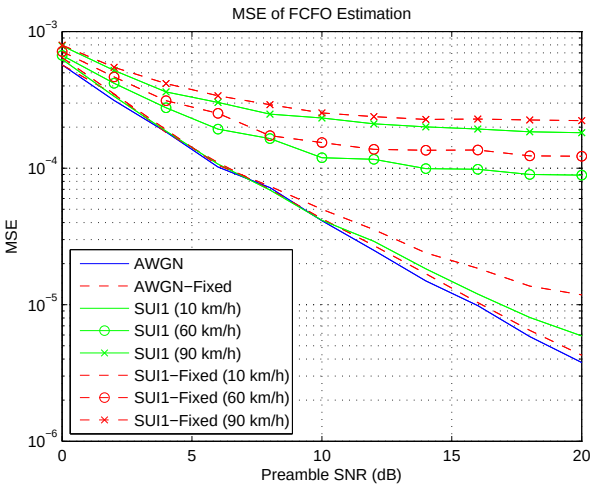

Fig. 28. Mean square error of FCFO estimation under SUI-1 and AWGN channels with fixed-point and floating-point computation.

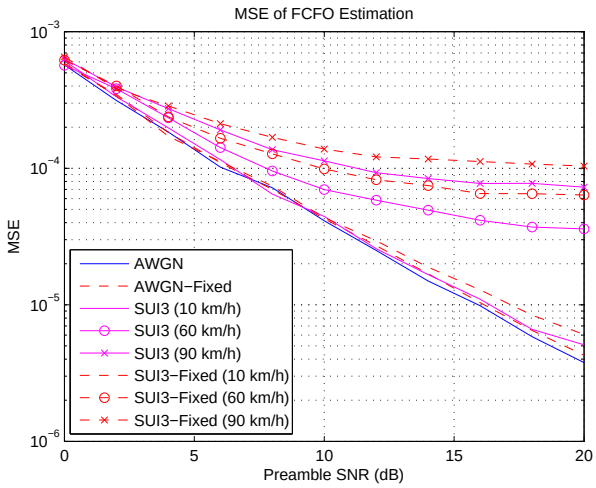

Fig. 29. Mean square error of FCFO estimation under SUI-3 and AWGN channels with fixed-point and floating-point computation.

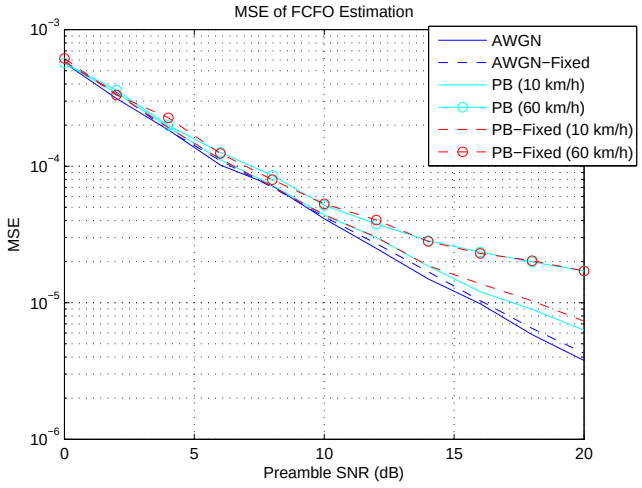

Fig. 30. Mean square error of FCFO estimation under PB and AWGN channels with fixed-point and floating-point computation.

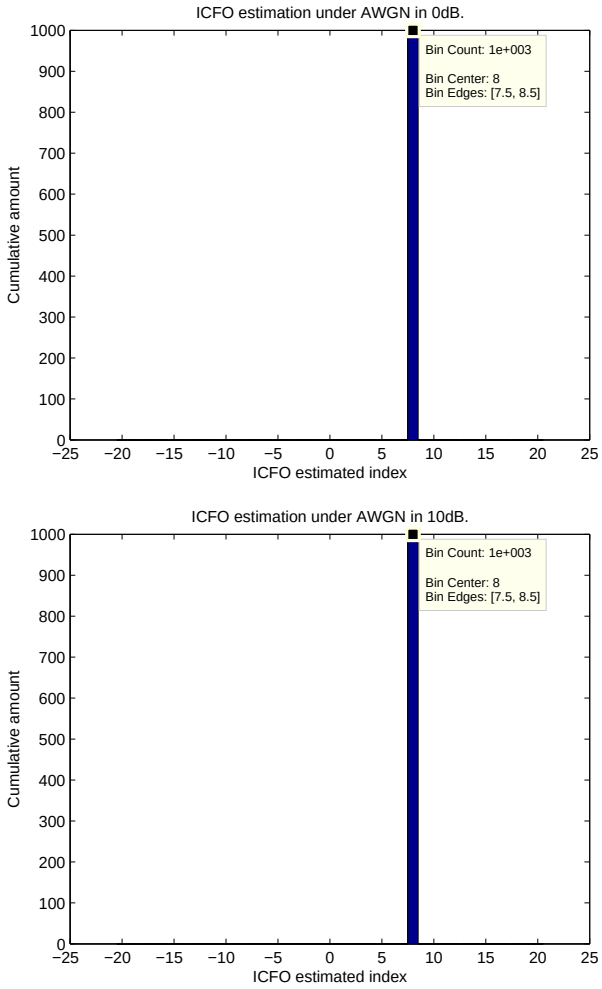

Fig. 31. Histograms of integer CFO estimation under AWGN channel in different SNR values with fixed-point implementation.

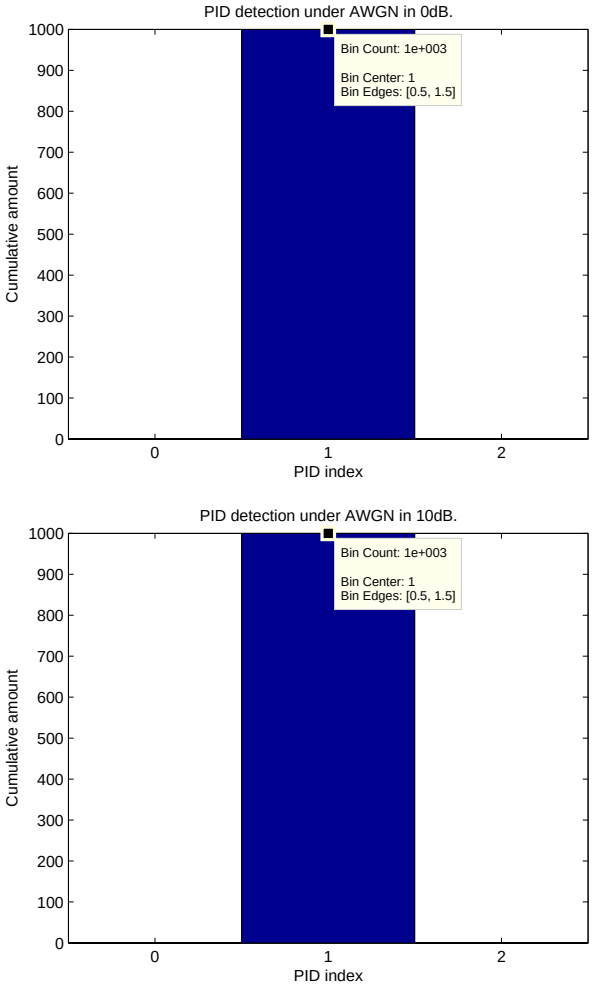

Fig. 32. Histograms of PID detection estimation under AWGN channel in different SNR values with fixed-point implementation.

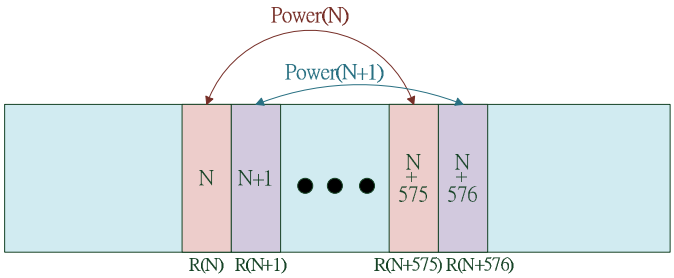

Fig. 33. Summation of magnitude-squares for coarse timing estimation.

六、IEEE 802.16m 通道估計技術之數位訊號處理器軟體實現研究

本節主要內容自下頁起，以學術論文初稿方式呈現。這些結果係摘自參考文獻[4]。本項成果係衍伸之前在演算法方面的研究成果[5]。

Digital Signal Processor Software Implementation of LMMSE Channel Estimation Method for IEEE 802.16m

Preliminary Draft

ABSTRACT

In this paper, we discuss about IEEE 802.16m OFDMA downlink channel estimation and adopt SFBC (special frequency block code) technique to resistant the channel fading. After that we use DSP fixed-point operation to analysis the performance. We present LMMSE channel estimation method in this thesis. First, we use LS estimator on pilot subcarrier to get the channel response. And then we use linear interpolation method to get channel response on other pilot position. After that we estimate the delay parameters and find correlation function associate exponential PDP. Finally base on this correlation function, do LMMSE filtering to estimate the data subcarrier response. This paper can be separated into four parts. First we introduce relevant IEEE 802.16m specification. Second, we introduce LMMSE algorithm. Third, we introduce DSP implementation environment and modify the floating-point C code to fixed-point. And then we against the fixed-point C code to accelerate and optimization. Finally we do the simulation on AWGN and SUI multipath channel to analysis the performance.

1. INTRODUCTION

Pilot-aided channel estimation is widely employed in today's coherent wireless orthogonal frequency-division multiplexing (OFDM) systems. The subcarriers that carry pilot signals are usually dispersed in frequency and in time. The LMMSE technique is also known as Wiener filtering. Given some initial channel estimates at the pilot subcarriers, the LMMSE channel estimate at any subcarrier d is given by [3], [4]

$$\hat{h}_d = \mathbf{w}_d^H \mathbf{h}_p \tag{1}$$

with

$$\mathbf{w}_d = (\mathbf{R}_{pp} + \sigma_n^2 \mathbf{I})^{-1} \mathbf{r}_{dp} \tag{2}$$

where h_d is the desired channel estimate; $\mathbf{w}_d$ is the Wiener filter; superscript H denotes Hermitian transpose; $\mathbf{h}_p$ is the vector of given initial channel estimates; $\mathbf{R}_{pp} = E(\mathbf{h}_p \mathbf{h}_p^H)$, with E denoting expectation and $\mathbf{h}_p$ being the vector of true channel responses at pilot carriers; $\mathbf{r}_{dp} = E(\mathbf{h}_p \mathbf{h}_d^H)$ with $\mathbf{h}_d$ being the true channel response at subcarrier d; σ_n^2 is the variance of additive noise in $\mathbf{h}_p$, assumed white Gaussian (i.e., AWGN); and $\mathbf{I}$ denotes an identity matrix. A usual method to estimate pilot response is called least-square (LS) method, which divides the received signal at each pilot carrier by the known pilot value there to obtain the pilot response.

To carry out the LMMSE estimation, we should know $\mathbf{R}_{pp}$, $\mathbf{r}_{dp}$, and σ_n^2. The estimation of σ_n^2 can be achieved by measuring the received power at the null subcarriers but the values of $\mathbf{R}_{pp}$ and $\mathbf{r}_{dp}$ need more work. One aspect of the problem has to do with the fact that an accurate estimate requires averaging over sufficiently many samples. But when the channel is time-varying, there may not be enough data point within a coherence time to facilitate this, especially if the system only transmits a small number of pilots. Another aspect of the problem of estimating $\mathbf{r}_{dp}$ is that usually requires interpolation (which implies approximation) in addition to averaging. The problem in estimating $\mathbf{R}_{pp}$ and $\mathbf{r}_{dp}$ makes strict-sense LMMSE channel estimation impractical in many cases.

To sidestep the above problem, reference [2] proposed a method to estimate the power-delay profile (PDP). Taking the Fourier transform of the PDP give the correlation function in frequency domain as.

$$\mathbf{R}_{Hf}(f) \triangleq \mathcal{F}[P_h(\tau)]. \tag{3}$$

For simplicity, we can employ a simple model for the channel PDP. One such choice is the exponential model [5]–[7], for which the entire second-order channel statistics are defined by the mean delay τ_μ and the root-mean-square (RMS) delay spread τ_{rms}. Given τ_μ and τ_{rms} as well as σ_n^2, one can calculate $\mathbf{R}_{pp}$ and $\mathbf{r}_{dp}$ and then calculate the Wiener filter $\mathbf{w}_d$. The price paid is that the PDP model employed may be an oversimplification of the actual situation, which results in modeling error. But [2] shows that the exponential PDP can yield good performance for LMMSE channel estimation and is suitable for various pilot-transmitting OFDM signal structures.

In this paper, we use the method of above-mentioned for downlink (DL) channel estimation in IEEE 802.16m and implement on digital signal processor (DSP) platform. In section 2, we introduce the IEEE 802.16m OFDMA downlink specification. In section 3, we introduce the channel estimation methods. In section 4, we introduce fixed point implementation and optimization methods. In section 5, we discuss the performance of channel estimation methods by fixed point implementation for downlink. At last, we give the conclusion and discuss some potential future work in section 6.

2. INTRODUCTION TO IEEE 802.16M OFDMA

1. Basic OFDMA Symbol Structure in IEEE 802.16m [10]

The Advanced Air Interface uses OFDMA as the multiple access scheme in the downlink. The material of this is taken

TABLE I

PRU STRUCTURE FOR DIFFERENT TYPES OF SUBFRAMES

Subframe Type	Number of Subcarriers	Number of Symbols
Type-1	18	6
Type-2	18	7
Type-3	18	5

from [10].

1) OFDMA Basic Terms: We introduce some basic terms appeared in the OFDMA physical layer (PHY) of IEEE 802.16m. These definitions help us understand the concepts of subcarrier allocation and transmission in IEEE 802.16m OFDMA.

- Physical and logical resource unit: A physical resource unit (PRU) is the basic physical unit for resource allocation. It comprises P_{sc} consecutive subcarriers by N_{sym} consecutive OFDMA symbols. P_{sc} is 18 subcarriers and N_{sym} is 6 OFDMA symbols for type-1 subframes, 7 OFDM symbols for type-2 subframes, and 5 OFDMA symbols for type-3 subframes. A logical resource unit (LRU) is the basic logical unit for distributed and localized resource allocations. An LRU is $P_{sc} \cdot N_{sym}$ subcarriers for type-1, type-2, and type-3 subframes. The LRU includes the pilots that are used in a PRU. The effective number of subcarriers in an LRU depends on the number of allocated pilots.
- Distributed resource unit: A distributed resource unit (DRU) contains a group of subcarriers which are spread across the distributed resource allocations within a frequency partition. The size of DRU equals the size of PRU, i.e., P_{sc} subcarriers by N_{sym} OFDMA symbols.
- Contiguous resource unit: The localized resource unit, also known as contiguous resource unit (CRU), contains a group of subcarriers which are contiguous across the localized resource allocations. The size of CRU equals the size of PRU, i.e., P_{sc} subcarriers by N_{sym} OFDMA symbols.

2) Frame Structure: The advanced air interface basic frame structure is illustrated in Fig. 1. Each 20 ms superframe is divided into four 5-ms radio frames. When using the same OFDMA parameters as in Figs. II and III with channel bandwidth of 5, 10, or 20 MHz, each 5-ms radio frame further consists of eight subframes for $G = 1/8$ and 1/16. With channel bandwidth of 8.75 or 7 MHz, each 5-ms radio frame further consists of seven and six subframes, respectively for $G = 1/8$ and 1/16. In the case of $G = 1/4$, the number of subframes per frame is one less than that of other CP lengths for each bandwidth case. A subframe shall be assigned for either downlink (DL) or uplink (UL) transmission. There are four types of subframes:

- Type-1 subframe consists of six OFDMA symbols.
- Type-2 subframe consists of seven OFDMA symbols.
- Type-3 subframe consists of five OFDMA symbols.
- Type-4 subframe consists of nine OFDMA symbols. This type shall be applied only to UL subframe for the 8.75 MHz channel bandwidth when supporting the WirelessMAN-OFDMA frames.

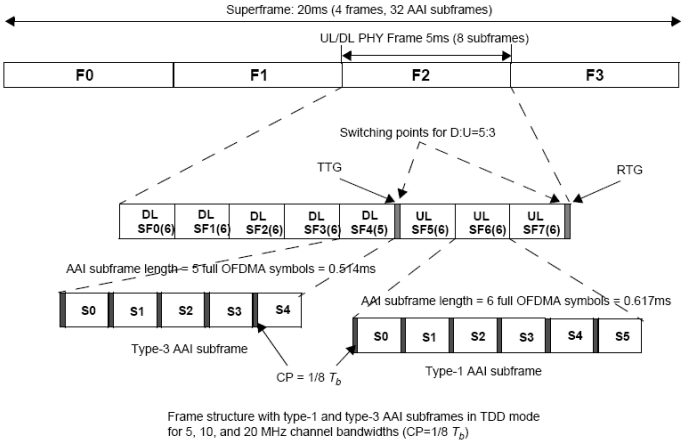

Frame structure with type-1 and type-3 AAI subframes in TDD mode for 5, 10, and 20 MHz channel bandwidths (CP=1/8 T_b)

Fig. 1. Frame structure for 5, 10 and 20 MHz modes (Fig. 484 in [10]).

TABLE II

OFDMA PARAMETERS (TABLE 794 IN [10])

The nominal channel bandwidth, BW (MHz)			5	7	8.75	10	20
Sampling factor, n			28/25	8/7	8/7	28/25	28/25
Sampling frequency, F_s (MHz)			5.6	8	10	11.2	22.4
FFT size, N_{FFT}			512	1024	1024	1024	2048
Subcarrier spacing, Δf (kHz)			10.94	7.81	9.77	10.94	10.94
Useful symbol time, T_b (μs)			91.4	128	102.4	91.4	91.4
CP ratio, G = 1/8	OFDMA symbol time, T_s (μs)		102.857	144	115.2	102.857	102.857
	FDD	Number of OFDMA symbols per 5ms frame	48	34	43	48	48
		Idle time (μs)	62.857	104	46.40	62.857	62.857
	TDD	Number of OFDMA symbols per 5ms frame	47	33	42	47	47
		TTG + RTG (μs)	165.714	248	161.6	165.714	165.714
CP ratio, G = 1/16	OFDMA symbol time, T_s (μs)		97.143	136	108.8	97.143	97.143
	FDD	Number of OFDMA symbols per 5ms frame	51	36	45	51	51
		Idle time (μs)	45.71	104	104	45.71	45.71
	TDD	Number of OFDMA symbols per 5ms frame	50	35	44	50	50
		TTG + RTG (μs)	142.853	240	212.8	142.853	142.853
CP ratio, G = 1/4	OFDMA symbol time, T_s (μs)		114.286	160	128	114.286	114.286
	FDD	Number of OFDMA symbols per 5ms frame	43	31	39	43	43
		Idle time (μs)	85.694	40	8	85.694	85.694
	TDD	Number of OFDMA symbols per 5ms frame	42	30	37	42	42
		TTG + RTG (μs)	199.98	200	264	199.98	199.98

TABLE III

ADDITIONAL OFDMA PARAMETERS (TABLE 795 IN [10])

The nominal channel bandwidth, BW (MHz)		5	7	8.75	10	20
Number of guard sub-carriers	Left	40	80	80	80	160
	Right	39	79	79	79	159
Number of used sub-carriers		433	865	865	865	1729
Number of physical resource unit (18x6) in a type-1 AAI subframe.		24	48	48	48	96

The basic frame structure is applied to FDD and TDD duplexing schemes, including H-FDD MS operation. The number of switching points in each radio frame in TDD systems shall be two, where a switching point is defined as a change of directionality, i.e., from DL to UL or from UL to DL.

2. Downlink Transmission in IEEE 802.16m OFDMA[10]

Again this section is mainly taken from [10]. Each DL subframe is divided into 4 or fewer frequency partitions; each partition consists of a set of physical resource units across the total number of OFDMA symbols available in the subframe. Each frequency partition can include contiguous (localized) and/or non-contiguous (distributed) physical resource units. Each frequency partition can be used for different purposes such as fractional frequency reuse (FFR) or multicast and broadcast services (MBS).

1) Subband Partitioning: The PRUs are first subdivided into subbands and minibands where a subband comprises N_1 adjacent PRUs and a miniband comprises N_2 adjacent PRUs, where $N_1 = 4$ and $N_2 = 1$. Subbands are suitable for frequency selective allocations as they provide a contiguous allocation of PRUs in frequency. Minibands are suitable for frequency diverse allocation and are permuted in frequency.

2) Miniband Partitioning: The miniband permutation maps the PRU_{MB}s to Permuted PRU_{MB}s ($PPRU_{MB}$s) to ensure that frequency diverse PRUs are allocated to each frequency partition.

3) Frequency Partitioning: The PRU_{SB} and $PPRU_{MB}$ are allocated to one or more frequency partitions.

3. Cell-Specific Resource Mapping[10]

The content of this section is mainly taken from [10]. PRU_{FPi}s are mapped to LRUs. All further PRU and subcarrier permutation are constrained to the PRUs of a frequency partition.

1) CRU/DRU Allocation: The partition between CRUs and DRUs is done on a sector specific basis. A 4 or 3-bit Downlink subband-based CRU Allocation Size ($DCAS_{SBi}$) field is sent in the SFH for each allocated frequency partition. $DCAS_{SBi}$ indicates the number of allocated CRUs for partition FP_i in unit of subband size.

2) Subcarrier Permutation: The subcarrier permutation defined for the DL distributed resource allocations within a frequency partition spreads the subcarriers of the DRU across the whole distributed resource allocations. The granularity of the subcarrier permutation is equal to a pair of subcarriers.

After mapping all pilots, the remainders of the used subcarriers are used to define the distributed LRUs. To allocate the LRUs, the remaining subcarriers are paired into contiguous tone-pairs. Each LRU consists of a group of tone-pairs.

4. Pilot Structure

1) Pilot patterns: Pilot patterns are specified within a PRU. Base pilot patterns used for DL data transmission with one data stream in dedicated and common pilot scenarios are shown in Figure 3, with the subcarrier index increasing from top to bottom and the OFDM symbol index increasing from left to right. Figs. 3(a) and 3(b) show the pilot locations for stream sets 0 and 1, respectively. The base pilot patterns used for two DL data streams in dedicated and common pilot scenarios are shown in Figure 4, where the subcarriers are indexed similarly to Figs. 3. Figs. 4(a) and 4(b) show the pilot locations for pilot streams 1 and 2 in a PRU, respectively. The number on

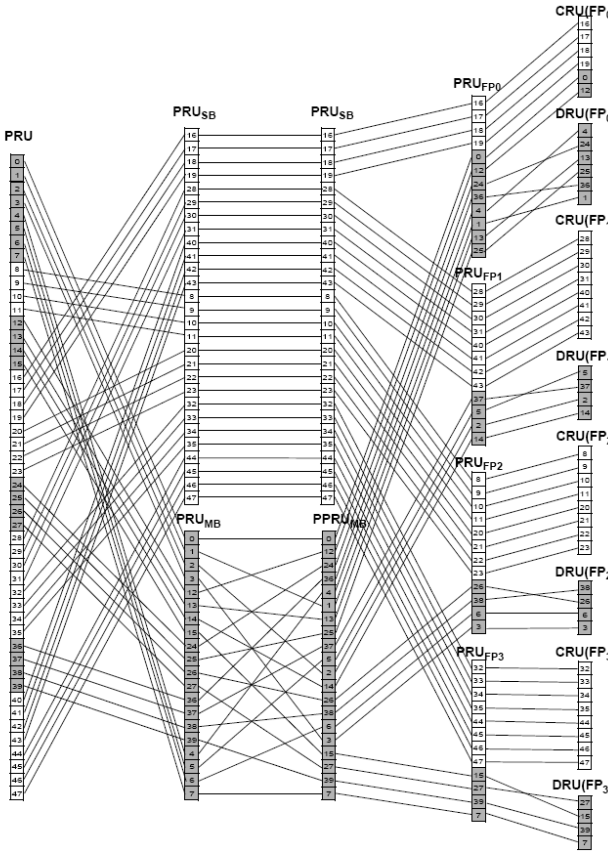

Fig. 2. Frequency partition for BW=10MHz, $K_{SB} = 7$, $FPCT = 4$, $FPCT = 4$, $FPS_0 = FPS_i = 12$, $DFPSC = 2$, $DCAS_{SB,0} = 1$, $DCAS_{MB,0} = 1$, $DCAS_i = 2$ and $IDcell = 0$ (Fig. 503 in [10]).

a pilot subcarrier indicates the pilot stream the pilot subcarrier corresponds to. The subcarriers marked as "X" are null sub-

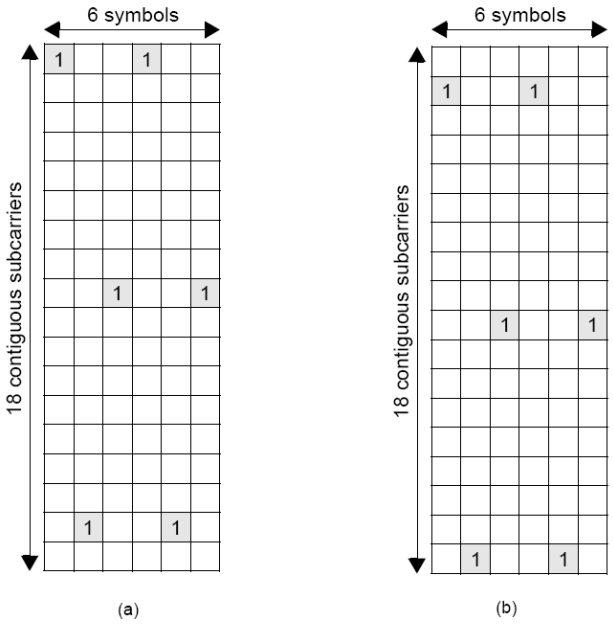

Fig. 3. Pilot patterns used for 1 DL data streams (Fig. 505 in [10]).

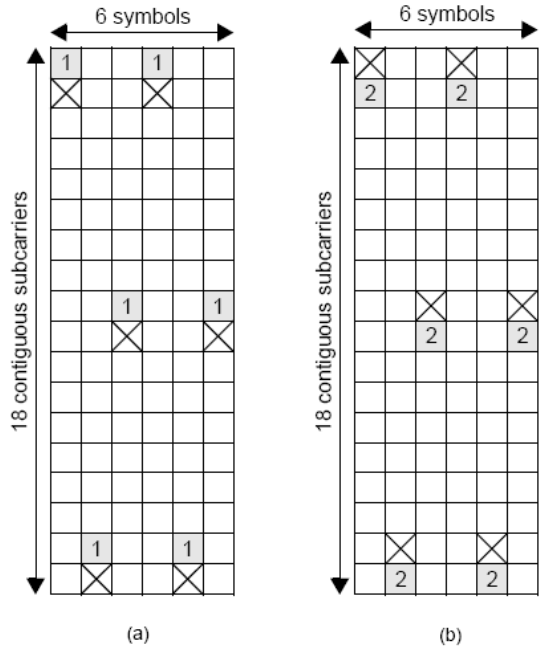

Fig. 4. Pilot patterns used for 2 DL data streams (Fig. 506 in [10]).

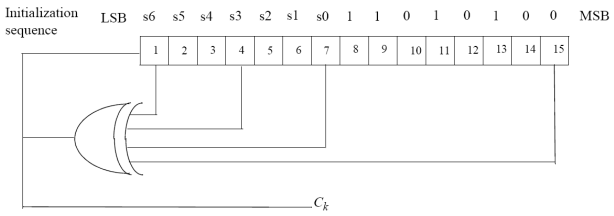

Fig. 5. PRBS generator for pilot modulation (Figure 584 in [10]).

carriers, on which no pilot or data is transmitted. In this thesis, we used the pilot structure for 2 DL data streams.

2) Pilot Modulation: Pilot subcarriers are inserted into each data burst in order to constitute the symbol. The PRBS (pseudo-random binary sequence) generator depicted in Fig. 5 is used to produce a sequence w_k. Each pilot is transmitted with a boosting of 2.5 dB over the average non-boosted power of each data tone. The pilot subcarriers is modulated according to

$$\Re\{c_k\} = \frac{8}{3}\left(\frac{1}{2} - w_k\right), \quad \Im\{c_k\} = 0. \tag{4}$$

5. Downlink MIMO Architecture and Data Processing

The architecture of downlink MIMO at the transmitter side is shown in Figure 6. The MIMO encoder block maps L MIMO layer $(L \geq 1)$ onto M_t MIMO streams $(M_t \geq L)$, which are fed to the precoder block. A MIMO layer is an information path fed to the MIMO encoder as an input. A MIMO layer represents one channel coding block. For the spatial multiplexing modes in single-user MIMO (SU-MIMO),"rank" is defined as the number of MIMO streams to be used for the user allocated to the Resource Unit (RU). For SU-MIMO,

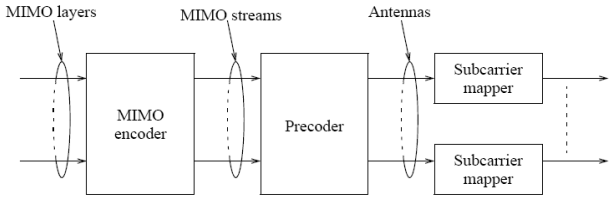

Fig. 6. DL MIMO (Figure 547 in [10]).

only one user is scheduled in one RU, and only one channel coding block exists at the input of the MIMO encoder (vertical MIMO encoding at transmit side). For MU-MIMO, multiple users can be scheduled in one RU, and multiple channel coding blocks exist at the input of the MIMO encoder. The existence of multiple channel coding blocks at the input of the MIMO encoder can be caused by either using horizontal encoding or by using vertical encoding in several MIMO layers or by using a combination of vertical and horizontal encoding in several MIMO layers at the transmit side. Using multiple MIMO layers is called multi-layer encoding.

6. MIMO Layer to MIMO Stream Mapping

MIMO layer to MIMO stream mapping is performed by the MIMO encoder. The MIMO encoder is a batch processor that operates on M input symbols at a time. The input to the MIMO encoder is represent by an $M \times 1$ vector as

$$\mathbf{s} = \begin{bmatrix} s_1 \\ s_2 \\ \vdots \\ s_M \end{bmatrix} \tag{5}$$

where s_i is the ith input symbol within a batch. In case of MU-MIMO transmissions, the M symbols belong to different MSs. Two consecutive symbols may belong to a single MIMO layer. One MS shall have at most one MIMO layer.

MIMO layer to MIMO stream mapping of the input symbols is done in the space dimension first. The output of the MIMO encoder is an $M_t \times N_F$ MIMO STC matrix as

$$\mathbf{X} = \mathbf{S}(\mathbf{s}) \tag{6}$$

where

- M_t is the number of MIMO streams,
- N_F is the number of subcarriers occupied by one MIMO block,
- $\mathbf{X}$ is the output of the MIMO encoder,
- $\mathbf{s}$ is the input MIMO layer vector,
- $\mathbf{S}()$ is a function that maps an input MIMO layer vector to an STC matrix, and
- $\mathbf{S}(\mathbf{s})$ is an STC matrix.

The STC matrix $\mathbf{X}$ can be expressed as

$$\mathbf{X} = \begin{bmatrix} x_{1,1} & x_{1,2} & \dots & x_{1,N_F} \\ x_{2,1} & x_{2,2} & \dots & x_{2,N_F} \\ \dots & \dots & \dots & \dots \\ x_{M_t,1} & x_{M_t,2} & \dots & x_{M_t,N_F}. \end{bmatrix}. \tag{7}$$

The four MIMO encoder formats (MEF) are space frequency block code (SFBC), vertical encoding (VE), multi-layer encoding (ME), and conjugate data repetition (CDR). In this paper, we only use SFBC MIMO encoder for implementation, so we just discuss about relevant SFBC technique content. For SU-MIMO transmissions, the STC rate is defined as

$$R = \frac{M}{N_F}. \tag{8}$$

For MU-MIMO transmissions, the STC rate per user (R) is equal to 1 or 2.

1) SFBC Encoding: The input to the MIMO encoder is represented by a 2×1 vector

$$\mathbf{s} = \begin{bmatrix} s_1 \\ s_2 \end{bmatrix}. \tag{9}$$

The MIMO encoder generates the SFBC matrix

$$\mathbf{X} = \begin{bmatrix} s_1 & -s_2^* \\ s_2 & s_1^* \end{bmatrix}. \tag{10}$$

where $\mathbf{X}$ is a 2×2 matrix. The SFBC matrix $\mathbf{X}$, occupies two consecutive subcarriers.

2) Signal Reception for SFBC Encoding: In this paper, we use the SFBC to MIMO stream mapping. Figure 7 shows the 2×1 SFBC structure in our system, where s_1 and s_2 are transmission signals, P_1 and P_2 are pilots, and i indicate the channel response for antenna i at subcarrier j. We encode and decode for a pair of subcarriers and use the least-square method to decode the received signal as

$$\mathbf{r} = \mathbf{H}\mathbf{s} + \mathbf{n}, \ \mathbf{s} = \begin{bmatrix} s_1 \\ s_2 \end{bmatrix}, \tag{11}$$

$$\begin{bmatrix} r_1 \\ r_2^* \end{bmatrix} = \begin{bmatrix} h_{11} & h_{21} \\ h_{22}^* & -h_{12}^* \end{bmatrix} \begin{bmatrix} s_1 \\ s_2 \end{bmatrix} + n, \tag{12}$$

$$\begin{bmatrix} \hat{s_1} \\ \hat{s_2} \end{bmatrix} = \frac{1}{h_{11}h_{12}^* + h_{21}h_{22}^*} \begin{bmatrix} r_1 h_{12}^* + r_2^* h_{21} \\ r_1 h_{22}^* - r_2^* h_{11} \end{bmatrix}. \tag{13}$$

For simplicity we use linear model, where r_i is received signal correspond to vector $\mathbf{r}$, and $\mathbf{H}$ is channel response matrix, and s_i is transmission signal corresponding to vector $\mathbf{s}$, where $\hat{s_i}$ is the estimation of s_i.

3. Basic Channel Estimation Methods

1. Least-Squares (LS) Estimator

Based on the a priori known data, we can estimate the channel responses at pilot carriers roughly by the least-squares (LS) technique. An LS estimator minimizes the squared error [11]

$$||\mathbf{y} - \mathbf{H}_{LS}\mathbf{x}||^2 \tag{14}$$

where $\mathbf{y}$ is the received signal and $\mathbf{x}$ is a priori known pilots, both in the frequency domain and both being $N \times 1$ vectors where N is the FFT size. $\mathbf{H}_{LS}$ is an $N \times N$ matrix whose values are 0 except at pilot locations m_i where $i = 0, \cdots, N_p - 1$, with N_p being the number of pilot:

$$\mathbf{H}_{LS} = \begin{bmatrix} h_{m_0,m_0} & \cdots & 0 & \cdots & 0 \\ 0 & \cdots & h_{m_1,m_1} & \cdots & 0 \\ 0 & \cdots & 0 & \cdots & 0 \\ 0 & \cdots & 0 & \cdots & h_{m_{N_p-1},m_{N_p-1}} \end{bmatrix}. \tag{15}$$

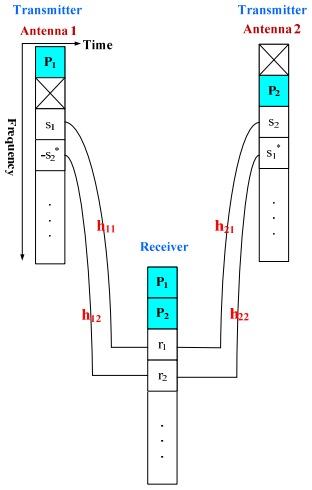

Fig. 7. SFBC structure.

Therefore, (14) can be rewritten as

$$[y(m) - x(m)h_{LS}(m)]^2, \text{ for all } m = m_i. \tag{16}$$

Then the estimate of pilot signals, based on only one observed OFDMA symbol, is given by

$$h_{LS}(m) = \frac{y(m)}{x(m)} = \frac{x(m)h(m) + n(m)}{x(m)} = h(m) + \frac{n(m)}{x(m)} \tag{17}$$

where $n(m)$ is the complex white Gaussian noise on subcarrier m. We may collect $h_{LS}(m)$ into $\mathbf{h}_{p,LS}$, an $N_p \times 1$ vector as

$$\begin{aligned} \mathbf{h}_{p,LS} &= [h_{p,LS}(0) \ h_{p,LS}(1) \ \cdots h_{p,LS}(N_p - 1)]^T \\ &= [\tfrac{y_p(0)}{x_p(0)}, \tfrac{y_p(1)}{x_p(1)}, \ldots, \tfrac{y_p(N_p-1)}{x_p(N_p-1)}]^T. \end{aligned} \tag{18}$$

where $h_{p,LS}(i)$ means the channel response uses LS method for estimation on ith pilot, and $y_p(i)$ means received signal on ith pilot and $x_p(i)$ means transmission signal on ith pilot. The LS estimator is a simplest channel estimator one can think of.

2. Linear Interpolation

After obtaining the channel response estimate at the pilot subcarriers, we use linear interpolation to obtain the responses at some other subcarriers. Exactly where apply it will be discussed later. Linear interpolation is a commonly considered scheme due to its low complexity. It does the interpolation between two known data. We use the channel estimate at two pilot subcarriers obtained by the LS estimator to estimate the channel frequency response information at the pilot subcarriers between them.

Linear interpolation may be done in frequency or in time. We only perform it in time. The channel estimate at the other pilot subcarrier for time index k, $mL < k < (m+1)L$, using linear interpolation is given by [12]

$$h_e(k) = h_e(mL+l) = [h_p(m+1) - h_p(m)]\frac{l}{L} + h_p(m) \tag{19}$$

where $h_p(k)$, $k = 0, 1, \cdots, N_p$, are the channel frequency responses at pilot subcarriers, L is the pilot subcarriers spacing, and $0 < l < L$.

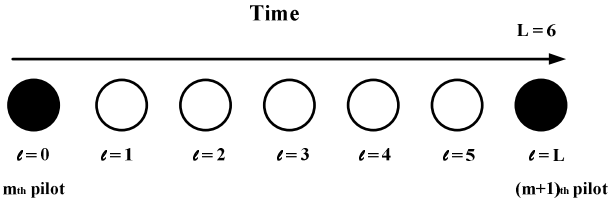

Fig. 8. Linear interpolation.

3. LMMSE Channel Estimation

We have given a brief introduction to the method in chapter 1. Now we describe it in more detail. The material in this section is mainly taken from [1], [2].

1) Channel Modeling for Channel Estimation: Consider a discrete-time equivalent lowpass channel impulse response

$$h(n) = \sum_{l=0}^{L-1} \alpha_l \delta(n-l) \tag{20}$$

where n and l are integers in units of the sampling period T_s and α_l is the complex gain of path l. The mean delay and the RMS delay spread are given by, respectively,

$$\tau_\mu = \frac{\sum_{l=0}^{L-1} E(|\alpha_l|^2) l}{\sum_{l=0}^{L-1} E(|\alpha_l|^2)} \tag{21}$$

and

$$\tau_{rms} = \sqrt{\frac{\sum_{l=0}^{L-1} E(|\alpha_l|^2)(l-\tau_\mu)^2}{\sum_{l=0}^{L-1} E(|\alpha_l|^2)}}. \tag{22}$$

One question here is how the expectation $E(|\alpha_l|^2)$ should be defined. As our purpose is channel estimation, suppose one channel estimation is performed for K OFDM symbols. Then the expectation should be an average that is taken over these symbol, note that we may let $k = 1$. In addition, we assume that the channel estimator input contains no carrier frequency error, but the PDP can have a nonzero initial delay τ_0, although conventional definition of the PDP usually zero out the initial path delays.

Fourier transforming the PDP gives the corresponding frequency autocorrelation function. For an exponential PDP with initial delay τ_0, we have

$$\frac{R_f(k)}{R_f(0)} = \frac{e^{-j2\pi\tau_0 k/N}}{1 + j2\pi\tau_{rms}k/N} \tag{23}$$

where $\tau_0 = \tau_\mu - \tau_{rms}$ and N is the DFT size used in the multicarrier system. For a uniform PDP of width T with a initial delay τ_0,

$$\frac{R_f(k)}{R_f(0)} = \frac{e^{-j2\pi\tau_0 k/N}\sin(\pi Tk/N)}{\pi Tk/N} \tag{24}$$

where $\tau_\mu = \tau_0 + T/2$ and $T = \sqrt{12\tau_{rms}}$.

2) Estimation of Channel Delay Parameters: The frequency response of the channel in (20) is given by

$$H(f) = \sum_{l=0}^{L-1} \alpha_l e^{-j2\pi lf/N} \tag{25}$$

where the division by N in the exponent normalizes the period of $H(f)$ in f to N. If we advance the channel response by τ (arbitrary) time units, then the frequency response becomes

$$H_a(f) = e^{j2\pi\tau f/N} H(f) = \sum_{l=0}^{L-1} \alpha_l e^{-j2\pi(l-\tau)f/N}. \tag{26}$$

Differentiating $H_a(f)$ with respect to f, we get

$$\frac{dH_a(f)}{df} = \frac{-j2\pi}{N} \sum_{l=0}^{L-1} \alpha_l (l-\tau) e^{-j2\pi(l-\tau)f/N}. \tag{27}$$

Applying Parsevals theorem, we get

$$J(\tau) \triangleq \left\langle |\frac{dH_a(f)}{df}|^2 \right\rangle = \frac{4\pi^2}{N^2} \sum_{l=0}^{L-1} |\alpha_l|^2 (l-\tau)^2 \tag{28}$$

where $< \cdot >$ denotes frequency averaging. Hence

$$\overline{J}(\tau) \triangleq E(\ \left\langle |\frac{dH_a(f)}{df}|^2 \right\rangle\ ) = \frac{4\pi^2}{N^2} \sum_{l=0}^{L-1} E((|\alpha_l|^2)(l-\tau)^2). \tag{29}$$

The above equations show that $\overline{J}(\tau)$ is minimized when $\tau = \tau_\mu$. In addition,

$$\tau_{rms}^2 = \frac{N^2 \min \overline{J}(\tau)}{4\pi^2 \sum_{l=0}^{L-1} E(|\alpha_l|^2)}. \tag{30}$$

For pilot-transmitting OFDM systems, the below given a way to find τ_μ and τ_{rms} from the frequency domain channel estimate.

Consider a system where one out of every F_s subcarriers is a pilot. We can approximate $dH_a(f)/df$ by the first-order difference, $[H_a(f+F_s) - H_a(f)]/F_s$ and substitute it into (29). Then, we obtain

$$\overline{J}(\tau) \approx \frac{1}{F_s^2} E\Big\langle |e^{j\phi} H(f+F_s) - H(f)|^2 \Big\rangle_p \tag{31}$$

where $\phi = 2\pi\tau F_s/N$, f takes values only over pilot frequencies, and $< \cdot >_p$ denotes averaging over pilot subcarriers. Then we modify the approximation by taking circular differencing over f rather than linear differencing. Therefore, we approximate $\overline{J}(\tau)$ by

$$\overline{J}(\tau) \approx \frac{1}{F_s^2} E\Big\langle |e^{j\phi} H\ ((f+F_s)\%N)\ - H(f)|^2 \Big\rangle_p \tag{32}$$

where $\%$ denotes modulo operation, and we have assumed that $(f + F_s)\%N$ is a pilot subcarrier. Now let R_i be the (instantaneous) frequency-domain autocorrelation of the channel response:

$$R_i = \Big\langle H((f+iF_s)\ \%N) H^*(f) \Big\rangle_p. \tag{33}$$

Then from (32) we have

$$\overline{J}(\tau) \approx \frac{2}{F_s^2} [E(R_0 - \Re\{e^{j\phi} E(R_1)\})]. \tag{34}$$

Then (34) gives an approximation of $\overline{J}(\tau)$ defined in (29). According to (34), τ_μ and τ_{rms} can be estimated in the following way:

1) estimate the channel responses at the pilot subcarriers,

2) estimate R_i $(i = 0, 1)$,
3) estimate $\overline{J}(\tau)$,
4) find the value of τ that minimizes $\overline{J}(\tau)$, and
5) substitute the result into (30) to estimate τ_{rms}^2.

Step 1 can be achieved using the LS method. For step 2, R_0 and R_1 can be estimated via

$$R_0 = \Big\langle |H(f)|^2 \Big\rangle_p - \sigma_n^2, \quad R_1 = \Big\langle H((f+F_s)\,\%N) H^*(f) \Big\rangle_p, \tag{35}$$

where we assume that σ_n^2 has been estimated in some way, such as from the received power in the null subcarriers. Thus, for step 3, $\overline{J}(\tau)$ can be estimated using

$$J_{Av}(\tau) \triangleq \frac{2}{F_s^2}\Big[Av(R_0) - R\{e^{j\phi} Av(R_1)\}\Big] \tag{36}$$

where Av denotes time averaging, i.e., averaging over OFDM symbols say k. For step 4, we may estimate the mean delay as

$$\tau_\mu \triangleq \arg\min J_{Av}(\tau) = -\frac{N \angle Av(R_1)}{2\pi F_s}, \tag{37}$$

which also yields $\min J_{Av}(\tau) = 2[Av(R_0) - |Av(R_1)|]/F_s^2$. Finally, for step 5, in view of (30) and that $R_0 =< |H(f)|^2 >_p$, we may estimate τ_{rms} as

$$\tau_{rms} = \frac{N}{2\pi F_s}\sqrt{2\Big[1 - \frac{|Av(R_1)|}{Av(R_0)}\Big]}. \tag{38}$$

3) LMMSE Filtering: To complete LMMSE channel estimation, the above estimates of delay parameters, namely, τ_μ and τ_{rms}, can be substituted into proper places in (23) or (24) depending on the choice of PDP model. Then the resulting autocorrelation function of channel frequency response can be used in LMMSE channel estimation as outlined in chapter 1.

4. Application to IEEE 802.16m

As mentioned previously, We employ the technique of [1], [2]. The LMMSE channel estimation for IEEE 802.16m proceeds as follows.

1) Do LS channel estimation at pilot subcarriers of all used PRUs.
2) Linearly interpolate in time to acquire two additional channel estimates per PRU per symbol, as shown by the arrows in Fig. 9.
3) Estimate R_0 and R_1 as explained below.
4) Estimate τ_μ and τ_{rms} as discussed below.
5) Find the autocorrelation function associated with the exponential PDP as

$$\frac{R_f(k)}{R_f(0)} = \frac{e^{-j2\pi\tau_0 k/N}}{1 + j2\pi\tau_{rms}k/N}, \tag{39}$$

where $\tau_0 = \tau_\mu - \tau_{rms}$ and N is the DFT size used in the multicarrier system.
6) Based on the above autocorrelation function, do LMMSE filtering to estimate the data subcarrier responses as

$$\mathbf{w}_d = (\mathbf{R}_{pp} + \sigma_n^2\mathbf{I})^{-1}\mathbf{r}_{dp}, \tag{40}$$

$$h_d = \mathbf{w}_d^h \mathbf{h}_p. \tag{41}$$

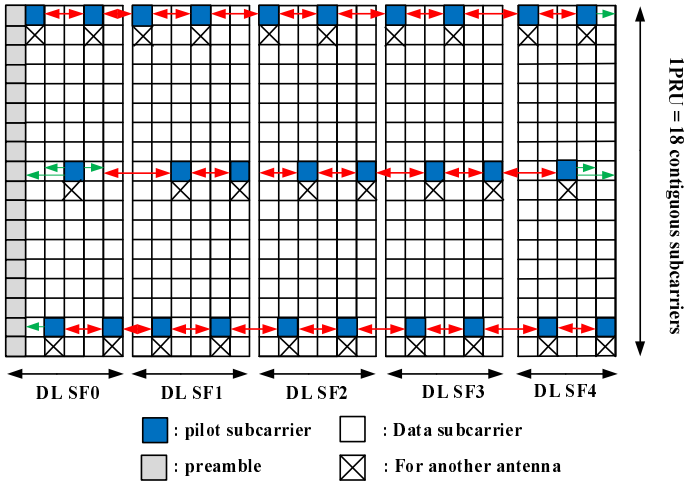

Fig. 9. Linear interpolation in time domain for 16m downlink signal.

Let $H(f)$ denote the resulting channel estimate at pilot subcarrier f from step 1. Let σ_n^2 be the variance of additive white gaussian noise (AWGN) at the pilot locations and linear interpolation from two pilots in step 2. For step 3, R_0 and R_1 can be estimated via

$$R_0 = \Big\langle |H(f)|^2 \Big\rangle_p - \sigma_n^2, \quad R_1 = \Big\langle H((f+F_s)\,\%N) H^*(f) \Big\rangle_p, \tag{42}$$

where $\Big\langle |H(f)|^2 \Big\rangle_p$ is the averaged magnitude-squares of estimation pilot subcarrier channel responses, σ_n^2 is the estimated noise variance at pilot subcarriers, and $F_s = 8$ (there is one pilot subcarrier every 8 subcarriers in IEEE 802.16m). For step 4, we may estimate the mean delay as

$$\tau_\mu = -\frac{N \angle Av(R_1)}{2\pi F_s}. \tag{43}$$

And we may estimate the RMS delay spread as

$$\tau_{rms} = \frac{N}{2\pi F_s}\sqrt{2\Big[1 - \frac{|Av(R_1)|}{Av(R_0)}\Big]}, \tag{44}$$

in our present work, we do delay estimation based on only one OFDM symbol for simplicity and for better performance in a time-varying channel. Hence we estimate R_0 and R_1 for each OFDM symbol separately.

4. Fixed-Point Implementation and Optimization Methods

In this chapter, we discuss some technique issue concerning our fixed-point implementation and some optimization methods to reduce the run time. Before the above, we first introduce the basic concepts of fixed-point and floating-point arithmetic. What is their difference? What are the advantages and disadvantage of fixed-point calculation? After these, we propose some techniques regarding C code implementation and optimization.

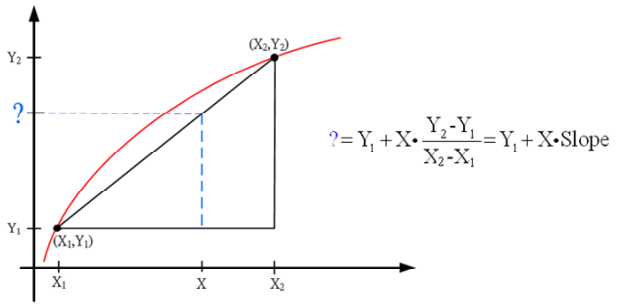

Fig. 10. Mixed method.

1. Nonlinear Function Implementation

In our implementation, we will need to carry out the computation of some function that are implemented the math library of C as subroutines. These subroutines may take many CPU cycles to execute. We can use some technique to avoid calling these subroutines and save cycles. We discuss the techniques below. Specially, the functions that we are interested in are sqrt(), sin(), cos(), and arctan().

1) Table Look-Up Method: A simplest method to implement a mathematical function is to use a look-up table. First, we build a table which contain the desired number of output values for the function. Then, we only need to enter the proper input index to get the answer from the table. But table size determines the needed memory space. If we want to have more output precision, then a larger table needs to be limit. Therefore, we have to know what range of input and output values that we need. When know there ranges, we can prevent wasting of unnecessary table space. Table look-up offer a simple method to replace calling library, but its precision depends on the table size. If the memory size is very limited, then it may not have enough space to store a table with the desired precision.

2) Mixed Method [14]: Mixed method is a trade off between table look-up and computation, which is based on table look-up but calculates the output value further by linear interpolation as shown in Figure 10. First, we have to build two tables of reduced size compared to the full-precision table, one is to record the function outputs and the other to record the slopes between pairs of input values. See Figure 10. If we want to know the corresponding output of X, we can get the answer by calculating the distance between X and X_1 and the slope between X_1 and X_2. Adopting this technique, we can use a little computation to exchange for more precision.

2. Q-Scaling Flow Chart

Figure 11 shows the flow chart of the channel estimation procedure together with the scaling factors of key variables. The channel estimation method has been introduced in chapter 4. The scaling factor have been designed based on theoretical analysis and they are determined so that a highest possible computational accuracy can be maintained without overflow.

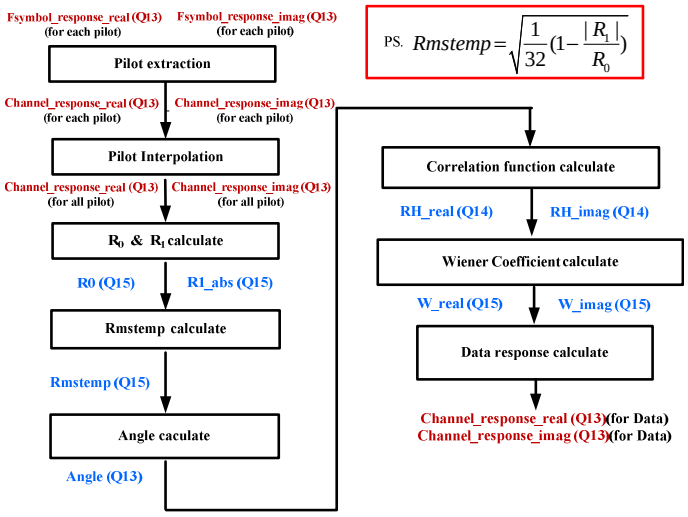

Fig. 11. Q-scaling flow chart for LMMSE channel estimation.

3. DIV_fixed Function Analysis

For fixed-point DSP implementation, we should try to avoid divisions. This is because the DSP does not have a hardware divide but call a library subroutine to carry out the division, which cost quite a few CPU cycles. If one wants to calculate x/y for some y many times, it is advisable to calculate the reciprocal of the divisor and record it first. Them we can calculate x/y for any x. This can reduce a large amount of cycles. In this work, we use divisions in several place which can reference to Fig.11: 1 division to calculate Rmstemp, 1 division for arctangent function to calculate angle, 17 divisions to calculate the correlation function, 4 divisions for Levinson-Durbin parameter calculation and 6 divisions for each data response calculation, totalling to $1+1+17+4+6\times 15$(data subcarrier number) = 113 divisions in theory for each OFDMA symbols.

But sometimes to calculate the reciprocal of the divisor would incur two problems. First is about overflow. For example, suppose we want to calculate $1/y$ and scale to Q13 and y uses Q14 scaling. Then

$$k=\frac{1}{y}\Rightarrow (Q13)(k)=\frac{(Q27)1}{(Q14)y}=\frac{2^{27}}{Y},$$
$$\text{range of } Y: 1 \text{ to } 2^{15} \text{ (assume } Y \text{ is positive)},$$
$$\text{range of } K: 2^{12} \text{ to } 2^{27}.$$

As for range of K, we have to use integer type for record K. If we want to reuse that, for example $Z/Y = Z\times K$ (however Z is short or integer type), we have to readjust the K scaling to avoid overflow. The second problem is about precision. For example, if we want to calculate $1/y$ and y is scaling to Q28, we can only get Q4 (assume y is positive) precision for result of $1/y$ at most. To avoid overflow and promote the precision of $1/y$, we design a subfunction which named DIV_fixed. Figure 12 shows the structure of that. Left branch can solve overflow problem and right branch can promote the precision of $1/y$.

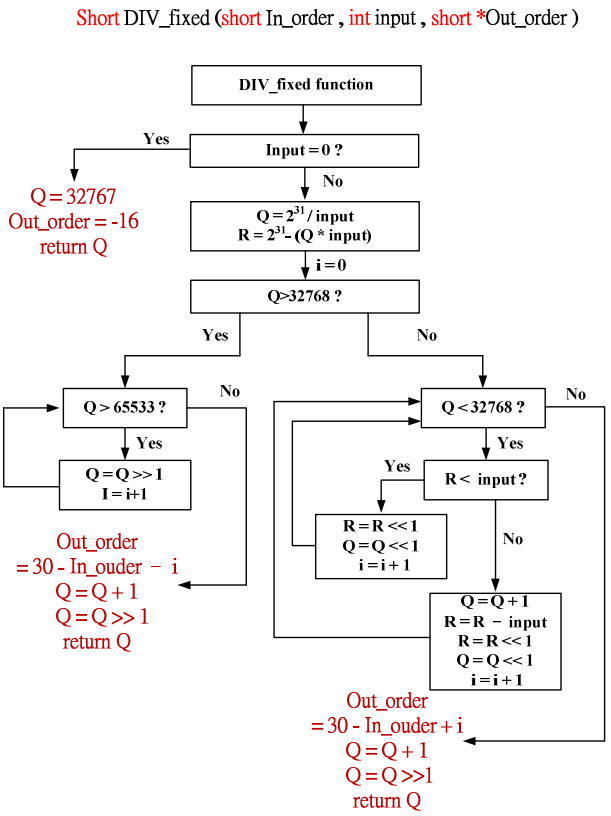

Fig. 12. DIV_fixed structure

```
void pilot_extraction ( int SymbolNumber,short *PilotPosition,short *PilotValue,
                        Q13 *Fsymbol_fixed_real        ,Q13 *Fsymbol_fixed_imag,
                        Q13 *Channel_response_fixed_real,Q13 *Channel_response_fixed_imag )
{
    short i;

    for(i=0;i<48;i++)
    {
        Channel_response_fixed_real[PilotPosition[i]]
      =3*Fsymbol_fixed_real[PilotPosition[i]] / ( 4 - (PilotValue[PilotPosition[i]]<<3) );

        Channel_response_fixed_imag[PilotPosition[i]]
      =3*Fsymbol_fixed_imag[PilotPosition[i]] / ( 4 - (PilotValue[PilotPosition[i]]<<3) );
    }
}
```

Fig. 13. C code for pilot subcarrier channel estimation before modification.

```
void pilot_extraction ( int SymbolNumber,Q13 *Fsymbol_fixed_real        ,Q13 *Fsymbol_fixed_imag,
                                         Q13 *Channel_response_fixed_real  ,Q13 *Channel_response_fixed_imag  )
{
    short i,subframe_symbolNumber;
    if(SymbolNumber%28<5)
    {
        subframe_symbolNumber = SymbolNumber % 28;
    }
    else if((4<SymbolNumber%28)  && (SymbolNumber%28<23))
    {
        subframe_symbolNumber = (SymbolNumber % 28 - 5)  % 6;
    }
    else if((22<SymbolNumber%28) && (SymbolNumber%28<28))
    {
        subframe_symbolNumber = (SymbolNumber % 28 - 23) % 5;
    }

    if     ( subframe_symbolNumber==0 || subframe_symbolNumber ==3 )
    {
        for(i=0;i<48;i++)
        {
            Channel_response_fixed_real[18*i]
          =(Q13)((int)( Fsymbol_fixed_real[18*i] * PilotValue_T1_0[i]) +2)>>2);

            Channel_response_fixed_imag[18*i]
          =(Q13)((int)( Fsymbol_fixed_imag[18*i] * PilotValue_T1_0[i]) +2)>>2);
        }
    }
    else if( subframe_symbolNumber==1 || subframe_symbolNumber ==4 )
    {
        for(i=0;i<48;i++)
        {
            Channel_response_fixed_real[16+18*i]
          =(Q13)((int)( Fsymbol_fixed_real[16+18*i] * PilotValue_T1_1[i]) +2)>>2);

            Channel_response_fixed_imag[16+18*i]
          =(Q13)((int)( Fsymbol_fixed_imag[16+18*i] * PilotValue_T1_1[i]) +2)>>2);
        }
    }
    else
    {
        for(i=0;i<48;i++)
        {
            Channel_response_fixed_real[8+18*i]
          =(Q13)((int)( Fsymbol_fixed_real[8+18*i] * PilotValue_T1_2[i]) +2)>>2);

            Channel_response_fixed_imag[8+18*i]
          =(Q13)((int)( Fsymbol_fixed_imag[8+18*i] * PilotValue_T1_2[i]) +2)>>2);
        }
    }
}
```

Fig. 14. C code for pilot subcarrier channel estimation after modification.

4. *Implementation and Optimization*

In this section we discuss the implementation and optimization of the channel estimation method whose flow chart has been given in Figure 11.

5. *Channel Estimation at pilot Subcarrier*

When we have received the signal, we first use the LS method to estimate the channel response at each pilots. Figure 13 shows the original version of pilot extraction function. In Figure 13 we observe that there are two parts that can be improved. One is about indexing. PilotPosition is an array which indicates the pilot positions of all the symbols, but using an array would result in some CPU cycles to obtain the desired values therein, so we try to avoid it. Because these pilot positions has regularity in 16m, we replace PilotPosition with the actual values, which is the first modification. The second modification is to replace division by multiplication. Figure 14 shows the final version of the same code section and Table IV shows the clock cycles for this function, where Excl.Total cycle means total number of cycles for all executions excluding function calls. The CCS can provide two different cycle data for reference, one with function aspect, and the other with loop aspect. In the former one can see the cycles for the function in the code, and in the latter, the loops we have broken the code from one loop in the original version into three loops in the modified version, but the total cycles are now less than the original version.

To evaluate the efficiency, note that there are two multipliers on C6416 chips. If the two multipliers can work in parallel without stall, the required cycles are Symbols $\times$ SNR $\times$ PRU $\times$ multiplications = $28 \times 11 \times 48 \times 1 = 14784$, so the efficiency is 14784/63509 = 23.3%. The performance is less than ideal, maybe which can improve in the future.

6. *Time-Domain Interpolation of Pilot Channel Responses*

After we get channel response for each pilot, we should do linear interpolation in time to get the channel responses as shown in Figure 9. To optimize this function, we can replace the constant divisions with multiplications. Figures 15 and 16 show a part of the original version and the modified version interpolation code, respectively. Table V shows the resulting cycle. To calculate efficiency, if the multipliers can work in parallel without stall, the require cycles are Symbols $\times$ SNR $\times$

TABLE IV
PILOT SUBCARRIER CHANNEL ESTIMATION CLOCK CYCLES COMPARISON

	Symbol Type	Excl. Total cycle	
Original	Function	579032	
	Loop	396311	
First modification	Function	465605	
	Loop (1)	91234	258246
	Loop (2)	90470	
	Loop (3)	76542	
Second modification	Function	102462	
	Loop (1)	22385	63509
	Loop (2)	22982	
	Loop (3)	18142	

TABLE V

PILOT INTERPOLATION CLOCK CYCLES COMPARISON

	Symbol Type	Excl. Total cycle
Original	Loop	485433
Modified	Loop	113784

```
else if(SymbolNumber%28==10)
        weight = 25939;//Q16(0.3958)
        for(i=0;i<48;i++)
        {
            channel_real_pre[5][i]=channel_response_real[PilotPosition[i]];
            channel_imag_pre[5][i]=channel_response_imag[PilotPosition[i]];
        }

        for(i=0;i<48;i++)
        {
            channel_response_real[PilotPosition_0[i]]
          =(channel_real_pre[0][i]-channel_real_pre[3][i])*3
           +channel_real_pre[3][i];

           channel_response_imag[PilotPosition_0[i]]
          =(channel_imag_pre[0][i]-channel_imag_pre[3][i])*3
           +channel_imag_pre[3][i];

            channel_response_real[PilotPosition_1[i]]
          =(channel_real_pre[4][i]-channel_real_pre[1][i])*3
           +channel_real_pre[1][i];

            channel_response_imag[PilotPosition_1[i]]
          =(channel_imag_pre[4][i]-channel_imag_pre[1][i])*3
           +channel_imag_pre[1][i];

            channel_response_real[PilotPosition_2[i]]=channel_real_pre[2][i];

            channel_response_imag[PilotPosition_2[i]]=channel_imag_pre[2][i];
        }
    }
```

Fig. 15. C code for pilot channel response interpolation before modification.

```
else if(SymbolNumber%28==10)
    {
        weight = 25939;//Q16(0.3958)
        for(i=0;i<48;i++)
        {
            channel_real_pre[5][i]=channel_response_real[8+18*i];
            channel_imag_pre[5][i]=channel_response_imag[8+18*i];
        }

        for(i=0;i<48;i++)
        {
            channel_response_real[18*i]
          =(Q13)((int)((channel_real_pre[0][i]-channel_real_pre[3][i])*10923 + 16384)>>15)
                    +channel_real_pre[3][i];

            channel_response_imag[18*i]
          =(Q13)((int)((channel_imag_pre[0][i]-channel_imag_pre[3][i])*10923 + 16384)>>15)
                    +channel_imag_pre[3][i];

            channel_response_real[16+18*i]
          =(Q13)((int)((channel_real_pre[4][i]-channel_real_pre[1][i])*10923 + 16384)>>15)
                    +channel_real_pre[1][i];

            channel_response_imag[16+18*i]
          =(Q13)((int)((channel_imag_pre[4][i]-channel_imag_pre[1][i])*10923 + 16384)>>15)
                    +channel_imag_pre[1][i];

            channel_response_real[8+18*i]=channel_real_pre[2][i]
            ;
            channel_response_imag[8+18*i]=channel_imag_pre[2][i];
        }
    }
```

Fig. 16. C code for pilot channel response interpolation after modification.

PRU $\times$ multiplications = $28 \times 11 \times 48 \times 4 = 59136$. Efficiency is 59136/113784 = 52%. The efficiency has exceeded fifty percent, the performance looks better.

7. Calculation of R_0 and R_1

After we calculate channel response for all pilots, we do LMMSE channel estimation for the data positions. First we should calculate the autocorrelation values R_0 and R_1. Because R_0 and R_1 are used in subsequent computation, their precision is very important. So we let them be Q15 to have maximum fractional bits allowed in 16-bit fixed-point format.

8. Rmstemp and Angle Calculation

We use the R_0 and R_1 to calculate mean delay and RMS delay spread which are combination by Rmstemp and the angle of R_1. Rmstemp is given by

$$\text{Rmstemp} = \sqrt{\frac{1}{32} \times (1 - \frac{|R_1|}{R_0})}$$

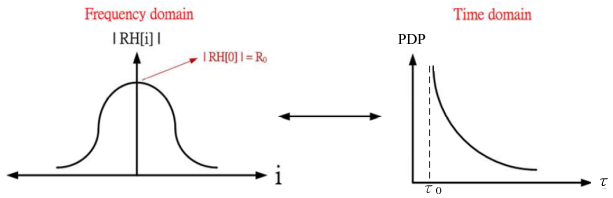

Fig. 17. Correlation function shapes in the time domain and the frequency domain.

which is a reduced parameter and which has positive proportional with RMS delay spread. The fixed-point implementation methods to calculate Rmstemp and angle has been discussed in sections 4.1.2.

9. Correlation Function Calculate

When we have the Rmstemp and the angle, we can use them to calculate the correlation function in the frequency domain. But in fixed-point implementation, because of numerical errors, some results may violate the physical meaning. Figure 17 illustrates its shapes in time and frequency. From the left plot, we see that the amplitude of $RH[0] = R_0$ is its maximum value in the frequency domain. So we set a limit as follows: if $|RH[i]|^2 > |RH[i-1]|^2$, then let $RH\_real[i] = RH\_real[i-1]$ and $RH\_imag[i] = RH\_imag[i-1]$, for $1 \leq i \leq 17$.

10. Wiener Coefficients Calculation

We use the correlation function to calculate the autocorrelation $\mathbf{R}_{pp}$ and the crosscorrelation $\mathbf{r}_{dp}$. As for the Wiener filter coefficients, we need to calculate the inverse matrix of $\mathbf{R}_{pp}$. We consider three methods: Gauss elimination, the direct formula method, and the Levinson-Durbin method. Recall that the Wiener filter coefficients as given by $\mathbf{w}_d = (\mathbf{R}_{pp} + \sigma_n^2\mathbf{I})^{-1}\mathbf{r}_{dp}$, where by the 16m signal structure, $(\mathbf{R}_{pp} + \sigma_n^2\mathbf{I})$ is a 3×3 matrix given by

$$\mathbf{R} \triangleq \mathbf{R}_{pp} + \sigma_n^2\mathbf{I} = \begin{bmatrix} RH[0]+\sigma_n^2 & RH[8] & RH[16] \\ RH[8]^* & RH[0]+\sigma_n^2 & RH[8] \\ RH[16]^* & RH[8]^* & RH[0]+\sigma_n^2 \end{bmatrix} = \begin{bmatrix} R_0 & R_8 & R_{16} \\ R_8^* & R_0 & R_8 \\ R_{16}^* & R_8^* & R_0 \end{bmatrix}.$$

1) Gauss Elimination: Figure 18 shows the process of Gauss elimination. Because $\mathbf{R}$ is a covariance matrix, it inverse has a Hermitian structure. For this reason, we only need to do the elimination six times to get the whole inverse matrix. But in this process, we can not control the numerical ranges of the values, so it is hard to give these values a proper scaling. After we complete the process, we may lose a large amount of precision in the process. So we also consider other methods to have better control over the scaling of values.

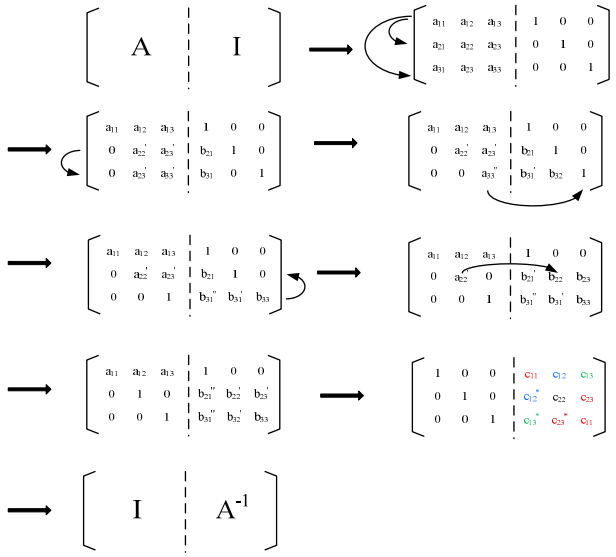

Fig. 18. Gauss elimination process.

2) Formula Method: The formula method is useful in computation of the inverse of small matrix. It is given by

$$\mathbf{R}^{-1} = \frac{1}{|det|}\begin{bmatrix} \begin{vmatrix} R_0 & R_8 \\ R_8^* & R_0 \end{vmatrix} & \begin{vmatrix} R_8^* & R_0 \\ R_8 & R_{16} \end{vmatrix} & \begin{vmatrix} R_8 & R_{16} \\ R_0 & R_8 \end{vmatrix} \\ \begin{vmatrix} R_{16}^* & R_0 \\ R_8^* & R_8 \end{vmatrix} & \begin{vmatrix} R_0 & R_{16} \\ R_8^* & R_0 \end{vmatrix} & \begin{vmatrix} R_8^* & R_8 \\ R_0 & R_{16} \end{vmatrix} \\ \begin{vmatrix} R_8^* & R_0 \\ R_{16}^* & R_8^* \end{vmatrix} & \begin{vmatrix} R_{16}^* & R_8^* \\ R_0 & R_8 \end{vmatrix} & \begin{vmatrix} R_0 & R_8 \\ R_8^* & R_0 \end{vmatrix} \end{bmatrix}. \quad (45)$$

The key issue lies in the multiplication by R_0, R_8 and R_{16}. To avoid overflow, we should downscale R_0, R_8 and R_{16} to Q9 (from the original Q14), which means significant loss in precision as result, we do not use this method in the final implementation.

3) Levinson-Durbin Method [15] : The Levinson-Durbin method is a common method for Toeplitz-shaped covariance matrix inverse calculation. Its advantages are a lower computational complexity than the Gauss elimination method in the case of large matrix and simple stability check [15]. We use *short* type and Q15 scaling for all parameters shown in Figs. 19 except $w_{1,0}$, $w_{1,1}$, P_0, P_1 and P_2. *Short* type using can accelerate the operation speed and Q15 scaling can maximize the precision. For $w_{1,0}$, $w_{1,1}$, P_0, P_1 and P_2, we let them to Q14 scaling analysis. We modify the formula in [15, pp. 377–378] to accommodate complex values and the process is shown in Figure 19. We divide the process into two functions, the upper function responsible to calculate k_1, k_2, $a_{2,1}$, P_0, P_1 and P_2. Another function $Levinson - Durbin$ calculates parameters remains. Figure 20 shows the implementation functions for Levinson-Durbin method. Because we do fixed-point implementation, we should set some limits to prevent overflow. Figure 21 shows the restrictions on Levinson-Durbin computation for fixed-point implementation.

4) Lower Bound on Noise Variance: Because of numerical errors in fixed-point calculation, when the SNR is high, too small noise variance in the covariance matrix may cause it to become singular and hamper its inversion. So we set a lower bound to noise variance therein. Assume the original noise variance is σ_1^2. Let there be a compensation noise variance is σ_2^2. Then the total noise variance is $\sigma_n^2 = \sigma_1^2 + \sigma_2^2$. The covariance matrix becomes

$$Rw = p \quad R = \begin{pmatrix} r(0) & r(1) & r(2) \\ r^*(1) & r(0) & r(1) \\ r^*(2) & r^*(1) & r(0) \end{pmatrix} \quad w = \begin{pmatrix} w_{2,0} \\ w_{2,1} \\ w_{2,2} \end{pmatrix} \quad p = \begin{pmatrix} p(0) \\ p(1) \\ p(2) \end{pmatrix}$$

$$P_0 = r(0)$$
$$c_0 = \frac{p(0)}{P_0}$$
$$w_{0,0} = c_0$$
$$k_1 = \frac{r^*(1)}{P_0}$$
$$a_{1,1} = k_1$$
$$P_1 = (1 - |k_1|^2) \times P_0$$
$$c_1 = \frac{p(1) - a_{1,1} \times p(0)}{P_1}$$
$$w_{1,0} = w_{0,0} - a_{1,1}^* \times c_1$$
$$w_{1,1} = c_1$$

$$k_2 = \frac{r^*(2) - a_{1,1} \times r^*(1)}{P_1}$$
$$a_{2,1} = a_{1,1} - k_1 \times a_{1,1}^*$$
$$a_{2,2} = k_2$$
$$P_2 = (1 - |k_2|^2) \times P_1$$
$$c_2 = \frac{p(2) - (a_{2,2} \times p(0)) - (a_{2,1} \times p(1))}{P_2}$$
$$w_{2,0} = w_{1,0} - a_{2,2}^* \times c_2$$
$$w_{2,1} = w_{1,1} - a_{2,1}^* \times c_2$$
$$w_{2,2} = c_2$$

Fig. 19. Basic Levinson-Durbin process for complex numbers.

$$P_0 = r(0)$$
$$k_1 = \frac{r^*(1)}{P_0}$$
$$a_{1,1} = k_1$$
$$P_1 = (1 - |k_1|^2) \times P_0$$
$$k_2 = \frac{r^*(2) - a_{1,1} \times r^*(1)}{P_1}$$
$$a_{2,1} = a_{1,1} - k_1 \times a_{1,1}^*$$
$$a_{2,2} = k_2$$
$$P_2 = (1 - |k_2|^2) \times P_1$$

$$Levinson\_Durbin(short * p, short * P, short * k, short * W)$$
$$\{$$
$$c_0 = \frac{p(0)}{P_0}$$
$$w_{0,0} = c_0$$
$$c_1 = \frac{p(1) - a_{1,1} \times p(0)}{P_1}$$
$$w_{1,0} = w_{0,0} - a_{1,1}^* \times c_1$$
$$w_{1,1} = c_1$$
$$c_2 = \frac{p(2) - a_{2,2} \times p(0) - a_{2,1} \times p(1)}{P_2}$$
$$w_{2,0} = w_{1,0} - a_{2,2}^* \times c_2 \quad w_{2,1} = w_{1,1} - a_{2,1}^* \times c_2 \quad w_{2,2} = c_2$$
$$\}$$
$$\}$$

Fig. 20. Implementation functions for Levinson-Durbin method.

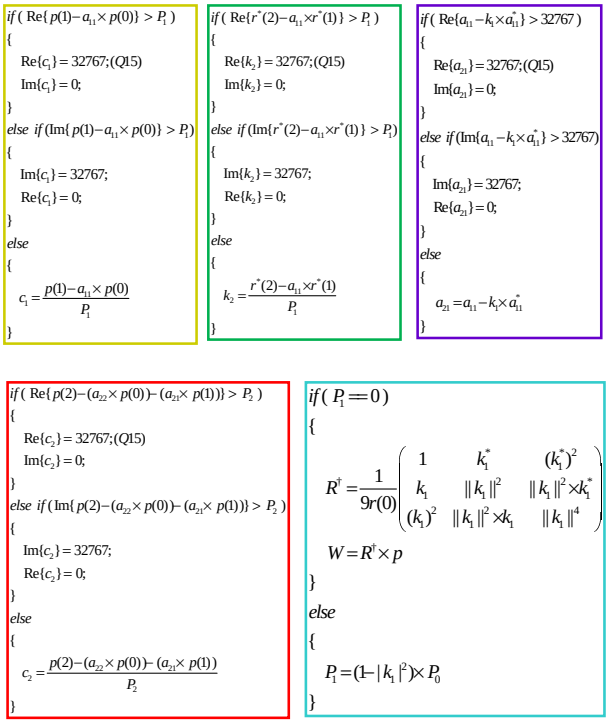

Fig. 21. Necessary precautions to maintain stability on fixed-point implementation for Levinson-Durbin method.

```
Rdp_real[0]=RH_real[15];
Rdp_real[1]=RH_real[7];
Rdp_real[2]=RH_real[1];

Rdp_imag[0]=   RH_imag[15];
Rdp_imag[1]=   RH_imag[7];
Rdp_imag[2]=-1*RH_imag[1];

Levinson_Durbin( Rdp_real, Rdp_imag, k_real, k_imag,P_MSE, W_real, W_imag);//Q15

for(i=0;i<48;i++)
{
    channel_response_real[PilotPosition_0[i]+15]
   =(Q13)(( (int)(W_real[0]*channel_response_real[PilotPosition_0[i]]
                 -W_imag[0]*channel_response_imag[PilotPosition_0[i]]
                 +W_real[1]*channel_response_real[PilotPosition_2[i]]
                 -W_imag[1]*channel_response_imag[PilotPosition_2[i]]
                 +W_real[2]*channel_response_real[PilotPosition_1[i]]
                 -W_imag[2]*channel_response_imag[PilotPosition_1[i]] ))>>15) ;

    channel_response_imag[PilotPosition_0[i]+15]
   =(Q13)(( (int)(W_real[0]*channel_response_imag[PilotPosition_0[i]]
                 +W_imag[0]*channel_response_real[PilotPosition_0[i]]
                 +W_real[1]*channel_response_imag[PilotPosition_2[i]]
                 +W_imag[1]*channel_response_real[PilotPosition_2[i]]
                 +W_real[2]*channel_response_imag[PilotPosition_1[i]]
                 +W_imag[2]*channel_response_real[PilotPosition_1[i]] ))>>15) ;
}
```

Fig. 22. C code for data subcarrier response calculation before modification.

```
Rdp_real[0]=RH_real[15];
Rdp_real[1]=RH_real[7];
Rdp_real[2]=RH_real[1];

Rdp_imag[0]=   RH_imag[15];
Rdp_imag[1]=   RH_imag[7];
Rdp_imag[2]=-1*RH_imag[1];

Levinson_Durbin( Rdp_real,Rdp_imag,k_real,k_imag,P_MSE,W_real,W_imag);

temp0_real = W_real[0];
temp0_imag = W_imag[0];
temp1_real = W_real[1];
temp1_imag = W_imag[1];
temp2_real = W_real[2];
temp2_imag = W_imag[2];

for(i=0;i<48;i++)
{
    channel_response_real[18*i+15]
   =(Q13)(( (int)(temp0_real*channel_response_real[18*i]
                 -temp0_imag*channel_response_imag[18*i]
                 +temp1_real*channel_response_real[8+18*i]
                 -temp1_imag*channel_response_imag[8+18*i]
                 +temp2_real*channel_response_real[16+18*i]
                 -temp2_imag*channel_response_imag[16+18*i] )+16384)>>15) ;

    channel_response_imag[18*i+15]
   =(Q13)(( (int)(temp0_real*channel_response_imag[18*i]
                 +temp0_imag*channel_response_real[18*i]
                 +temp1_real*channel_response_imag[8+18*i]
                 +temp1_imag*channel_response_real[8+18*i]
                 +temp2_real*channel_response_imag[16+18*i]
                 +temp2_imag*channel_response_real[16+18*i] )+16384)>>15) ;
}
```

Fig. 23. C code for data subcarrier response calculation after modification.

$$\mathbf{R} = \begin{bmatrix} RH[0]+\sigma_1^2+\sigma_2^2 & RH[8] & RH[16] \\ RH[8]^* & RH[0]+\sigma_1^2+\sigma_2^2 & RH[8] \\ RH[16]^* & RH[8]^* & RH[0]+\sigma_1^2+\sigma_2^2 \end{bmatrix} = \begin{bmatrix} RH[0]+\sigma_n^2 & RH[8] & RH[16] \\ RH[8]^* & RH[0]+\sigma_n^2 & RH[8] \\ RH[16]^* & RH[8]^* & RH[0]+\sigma_n^2 \end{bmatrix}.$$

This way of lower-boundary the noise variance, however, leads to an error floor in the channel estimation performance. In our experiments, for the downlink system, a lower bound of $\sigma_n^2 = (Q16)7000$ $(SNR \approx 9.714)$ dB would get the better performance. For uplink system, a lower bound of $\sigma_n^2 = (Q16)9000$ $(SNR \approx 8.622)$ dB is better.

At last we offer a possible solution for error floor. We can maintain the original noise variance in matrix $\mathbf{R}$ but compensate a little noise variance on c_0 and k_1, where c_0 and k_1 are parameters in Levinson-Durbin method and which has discussed in Section 4.10.3. By reducing the amount of noise variance compensation mights be possible to let error floor slightly, but we do not validate the performance are there on this way, maybe which can implement in future work.

11. Data Channel Response Calculate

After we get the Wiener filter coefficients, we use them to calculate the data subcarrier channel responses. For optimization, Figure 22 shows the original code. We can employ the method used in Section 4.5 to replace the PilotPosition. Another optimization is replacing the pointer. Because we save the Wiener filter coefficients in an array, when we call them for multiplications, we have to use an array pointer to obtain their values, which result in multilevel data loading and cost large amount of cycles. So we first place the Wiener filter coefficients into temporary registers as shown in Figure 23 and use the temporary registers for multiplication. Table VI shows the cycles and efficiency evaluation of all the modifications for data subcarrier response calculation, the field names Rounding means we consider the rounding effect in our program, we can see it would increase additional cycles. The average efficiency for fifteen data subcarrier can be calculated by : Symbols × SNR × PRU × multiplications = $28 \times 11 \times 48 \times 6 = 88704$. Efficiency is 88704/143896.8 = 61.64%. We can see good performance from the result.

12. Summary

According to the above discussion, we reduce the total clock cycle time and code size successfully. Finally, DSP C6000 compiler compile our C code and packages to a out file, which size is 273 KB. Table VII shows the clock cycles for all C code functions. Incl.Total cycle means total number of cycles for all executions including function calls. Subfunction $channel\_estimation\_fixed$ includes all the functions described in Figure 11. And subfunction $interpolation$ includes all the function described in Figure 11 except pilot subcarrier channel estimation. Subfunction $main$ deals with SNR and symbol number setting. $ParameterTable$ record the pilot value. Because of we do not write all the C code

TABLE VI

DATA SUBCARRIER CHANNEL RESPONSE CALCULATION CLOCK CYCLES COMPARISON

Method / Carrier index (0~17)	Original	PilotPosition replacement	Pointer replacement	Rounding
0				
1	425236	165841	166629	166265
2	426580	167244	165088	172172
3	426662	166937	164780	166529
4	426580	168685	163758	163720
5	428428	152192	112763	132963
6	425093	103918	106876	135828
7	423856	152460	107986	142604
8				
9	423707	152460	113960	135828
10	426844	152460	113960	136064
11	424082	152460	113960	135828
12	425275	152460	106876	135828
13	426272	152460	105028	132992
14	424580	149819	104798	132913
15	423620	149720	104296	133090
16				
17	424202	152460	113960	135828
Average	425401.133	152771.733	124314.533	143896.8
Efficiency	20.85%	58.06%	71.35%	61.64%

TABLE VII

DOWNLINK CHANNEL ESTIMATION CLOCK CYCLE TABLE FROM THE FUNCTION ASPECT

Symbol Name	Symbol Type	Access Count	cycle.Total: Incl. Total	cycle.Total: Excl. Total	
Levinson_Durbin	function	8932	5056491	3592638	37.47%
interpolation	function	308	9115806	3364697	35.10%
_divi <TI Library>	function	56634	1206137	1206137	12.58%
memcpy <TI Library>	function	11764	707276	707276	7.38%
Sin_Fix	function	5202	315037	315037	3.29%
pilot_extraction	function	308	104926	97842	1.02%
Cos_Fix	function	2601	241925	84410	0.88%
_divu <TI Library>	function	2396	53733	53733	0.56%
main	function	1	26976923	41298	0.43%
Atan_Fix	function	305	40096	31169	0.33%
channel_estimation_fixed	function	341	9262628	29917	0.31%
DIV_fixed	function	272	32249	23817	0.25%
_remi <TI Library>	function	1232	20798	20798	0.22%
Sqrt_Fix	function	350	13696	13696	0.14%
SqrtTable	function	1	2556	2556	0.03%
AtanTable	function	1	1159	1159	0.01%
SinTable	function	1	861	861	0.01%
Total required cycles				9587041	

TABLE VIII

DOWNLINK CHANNEL ESTIMATION CLOCK CYCLE PROPORTIONAL DISTRIBUTED

Function name	Percentage
Pilot subcarrier channel estimation	1.69%
Time domain interpolation of pilot channel response	4.66%
Calculation of R_0 and R_1	3.22%
Rmstemp and angle calculation	1.11%
Correlation function calculate	7.19%
Wiener coefficient calculation	29.04%
Data channel response calculate	46.64%
Remains	6.45

as functions, so we just approximate the proportion for total cycles. Table VIII shows the proportion for total cycles without considering TI library.

The original C code without any optimization needs 13340267 clock cycles for calculation, after our optimized methods as describes in this chapter, which just need 9587041 cycles. We reduced to approximate 72% cycles of the original program. We try to find the required time per OFDMA symbol, the required cycles are total cycles counts $\times$ clock cycle time $\div$ (SNR $\times$ Symbols) = $9587041 \times 10^{-9} \div (11 \times 28) = 31.13(\mu s)$, and OFDMA symbol period are (FFT size + CP length $\div$ sampling frequency = $1152 \div (11.2 \times 10^6) = 102.86(\mu s)$. In the other word, we only use 30% symbol period for channel estimation, which remains 70% symbol period for the other use, just like channel coding, synchronization, etc.

5. FIXED-POINT SIMULATION RESULTS

1. System Parameters and Channel Model

Table IX shows the parameters used in our simulation work. For the downlink, TDD frame length = 5 ms, DL subframe size = 1 preamble + 28 OFDM symbols, and 48 PRUs are used in transmission. In addition to AWGN, we use SUI-2 and SUI-5 for simulation. Their channel profiles are as shown in Tables X. Erceg *et al.* [13] published a total of 6 different radio channel models for type G2 (i.e., LOS and NLOS) MMDS BWA systems in three terrain categories. The three types in suburban area are:

- A: hilly terrain, heavy tree,
- C: flat terrain, light tree, and
- B: between A and C.

The correspondence with the so-called SUI channels is:

- C: SUI-1, SUI-2,
- B: SUI-3, SUI-4, and
- A: SUI-5, SUI-6.

In the above, SUI-1 and SUI-2 are Ricean multipath channels, whereas the other four are Rayleigh multipath channels. The Rayleigh channels are more hostile and exhibit a greater RMS delay spread. And the SUI-2 represents a worst-case link for terrain type C. We employ SUI-1 to SUI-6 model in our simulation, but we use Rayleigh fading to model all the paths in these channels.

2. Validation with AWGN Channel

We verify the correctness of the program code by simulation AWGN channel transmission. Both SISO and SFBC MIMO transmission are consider. We run 10^5 symbols in each simulation to obtain the numerical results. Figs. 24 shows the DL channel estimation performance in SISO transmission for AWGN channel. In our results, the MSE performance for fixed-point implementation is very close to floating-point result. Although we set a lower bound to noise variance, the

TABLE IX

OFDMA DOWNLINK PARAMETERS

Parameters	Values
Bandwidth	10 MHz
Central frequency	3.5 GHz
N_{used}	865
Sampling factor n	28/25
G	1/8
N_{FFT}	1024
Sampling frequency	11.2 MHz
Subcarrier spacing	10.94 kHz
Useful symbol time	91.43 μs
CP time	11.43 μs
OFDMA symbol time	102.86 μs
Sampling time	44.65 ns

TABLE X

PROFILES OF SUI-2 AND SUI-5 CHANNELS [13]

SUI – 2 Channel

	Tap 1	Tap 2	Tap 3	Units
Delay	0	0.4	1.1	µs
Power (omni ant.)	0	-12	-15	dB
90% K-fact. (omni)	2	0	0	
75% K-fact. (omni)	11	0	0	
Power (30° ant.)	0	-18	-27	dB
90% K-fact. (30°)	8	0	0	
75% K-fact. (30°)	36	0	0	
Doppler	0.2	0.15	0.25	Hz

Antenna Correlation: $\rho_{ENV} = 0.5$
Gain Reduction Factor: GRF = 2 dB
Normalization Factor: $F_{omni} = -0.3930$ dB, $F_{30°} = -0.0768$ dB

Terrain Type: C
Omni antenna: $\tau_{RMS} = 0.202$ µs,
overall K: K = 1.6 (90%); K = 5.1 (75%)
30° antenna: $\tau_{RMS} = 0.069$ µs,
overall K: K = 6.9 (90%); K = 21.8 (75%)

SUI – 5 Channel

	Tap 1	Tap 2	Tap 3	Units
Delay	0	4	10	µs
Power (omni ant.)	0	-5	-10	dB
90% K-fact. (omni)	0	0	0	
75% K-fact. (omni)	0	0	0	
50% K-fact (omni)	2	0	0	
Power (30° ant.)	0	-11	-22	dB
90% K-fact. (30°)	0	0	0	
75% K-fact. (30°)	2	0	0	
50% K-fact. (30°)	7	0	0	
Doppler	2	1.5	2.5	Hz

Antenna Correlation: $\rho_{ENV} = 0.3$
Gain Reduction Factor: GRF = 4 dB
Normalization Factor: $F_{omni} = -1.5113$ dB, $F_{30°} = -0.3573$ dB

Terrain Type: A
Omni antenna: $\tau_{RMS} = 2.842$ µs
overall K: K = 0.1 (90%); K = 0.3 (75%); K = 1.0 (50%)
30° antenna: $\tau_{RMS} = 1.276$ µs
overall K: K = 0.4 (90%); K = 1.3 (75%); K = 4.2 (50%)

error floor phenomenon is not obviously for MSE in AWGN channel.

3. SISO Transmission Results

We conduct simulation with the six SUI channels to examine the channel estimation performance. Figure 25 and Figure 26 shows the simulation results in SUI-2 channel and SUI-5 channel, respectively. In our result, because of the precise problem, the MSE performance of channel estimation different velocities become hardly distinguishably. When SNR small, the MSE curve for fixed-point is very close to floating-point, but if the SNR value is bigger than 12 dB, because we set a lower bound to avoid singular, the error floor would occurrence.

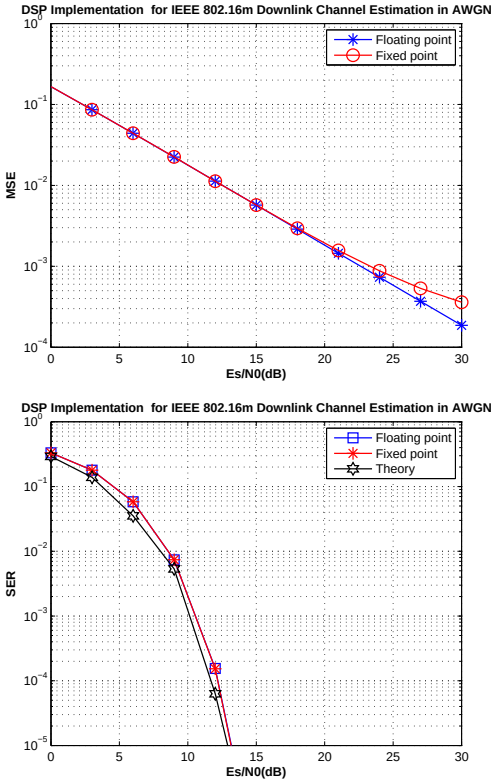

Fig. 24. Fixed-point channel estimation MSE and SER for QPSK in AWGN for IEEE 802.16m downlink.

4. SFBC Transmission Results

SFBC is a technique that uses multiple antennas to achieve better diversity effect. Figure 28 and Figure 29 shows the simulation results in SUI-2 channel and SUI-5 channel, respectively. In our simulation, we use two transmit antennas and one receive antenna. We estimate the two channel responses separately. So the MSE performance is not different by using SFBC as compared to SISO, but the SER performance is better. To check with our results, the fixed-point MSE curve is very close to floating point and which has similar SER performance to floating-point in AWGN channel.

6. CONCLUSION

In this thesis, first half of that we discussed about the LMMSE channel estimation method for OFDMA downlink and uplink for IEEE 802.16m. We summarize the process to following steps:

- First, use least-square method on pilot position to get each pilot response.
- Second, do linear interpolation in time to get all the pilot response and related equivalent to true pilot position and there referred to as pilot positions..
- Third, use pilot response to calculate mean delay and rms delay.
- Fourth, use above two parameters to calculate correlation function
- Fifth, use correlation function to calculate Wiener filter coefficient.

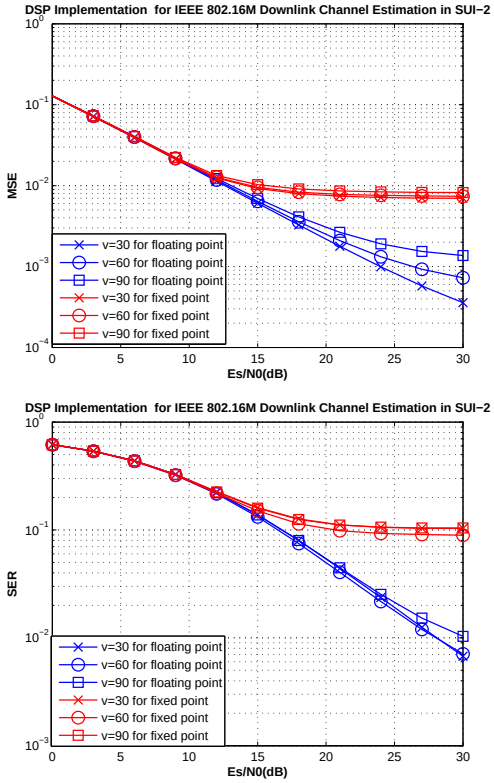

Fig. 25. Fixed-point channel estimation MSE and SER for QPSK at different velocities in SUI-2 channel for IEEE 802.16m downlink, where the speed v is km/h.

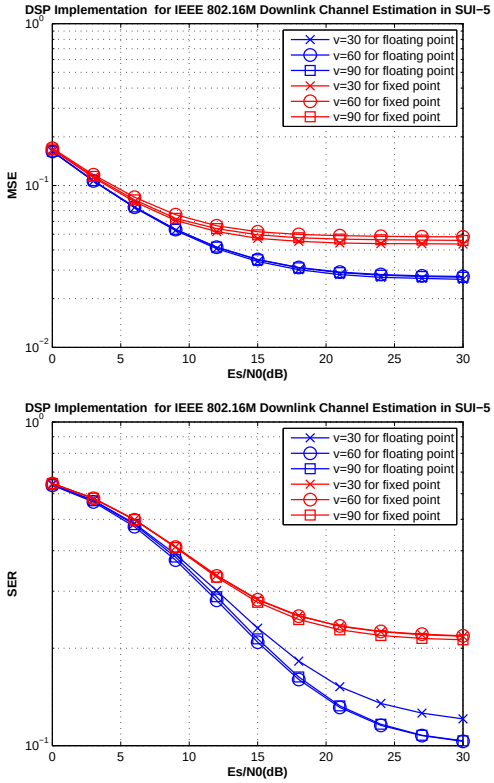

Fig. 26. Fixed-point channel estimation MSE and SER for QPSK at different velocities in SUI-5 channel for IEEE 802.16m downlink, where the speed v is km/h.

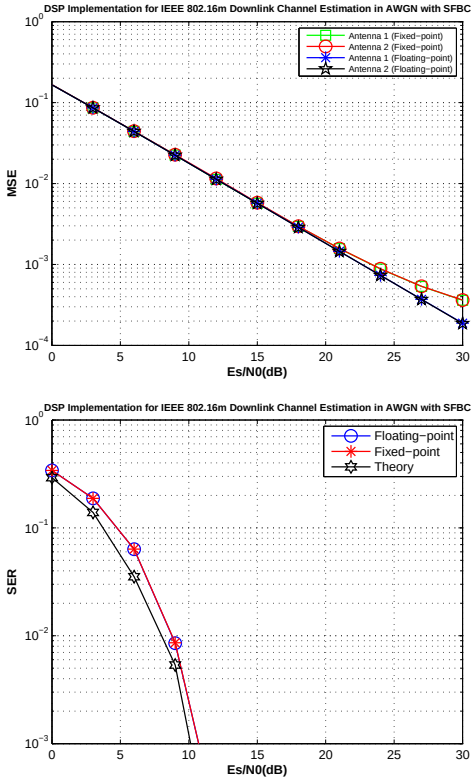

Fig. 27. Fixed-point channel estimation MSE and SER for QPSK with SFBC in AWGN channel for IEEE 802.16m downlink.

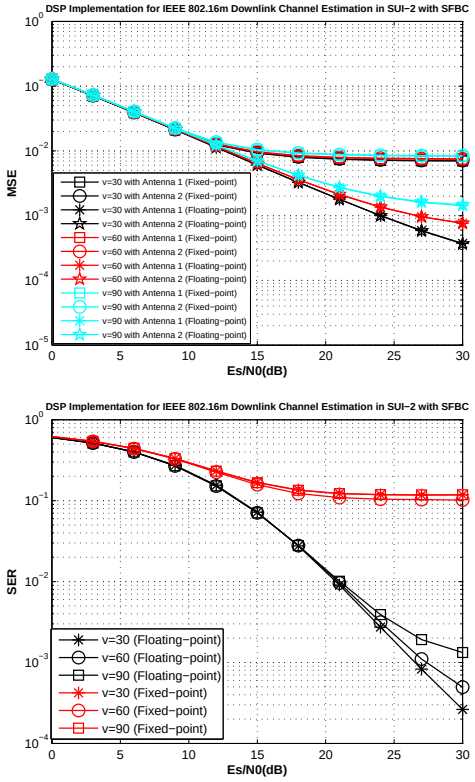

Fig. 28. Fixed-point channel estimation MSE and SER for QPSK with SFBC at different velocities in SUI-2 channel for IEEE 802.16m downlink, where the speed v is km/h.

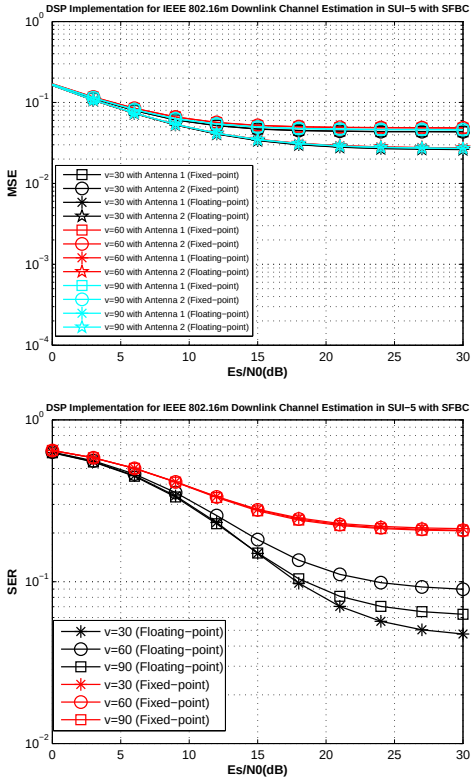

Fig. 29. Fixed-point channel estimation MSE and SER for QPSK with SFBC at different velocities in SUI-5 channel for IEEE 802.16m downlink, where the speed v is km/h.

- Sixth, calculate data response by Wiener filter calculation.

and we extended to multiple antennas with SFBC technique, we validation with C code simulation and compared the result with different channel types.

The last half of thesis we discussed about fixed-point implementation on DSP chip. We integrated the contents to following items:

- We analysis the advantages and defects of fixed-point and floating-point calculation.
- Discussed the importance of scaling factor and propose two different scaling expression for reference.
- The knack of nonlinear function implementation and summarized four steps for fixed-point implementation pre-work.
- We designed a division subfunction to prevent overflow operation and maintain the precision.
- Along the channel estimation process to analysis and optimized the C code.

REFERENCES

[1] Chih-Wei Wang, "LMMSE channel estimation for IEEE 802.16e and 802.16m OFDMA DownLink," M.S. thesis, Department of Electronics Engineering and Institute of Electronics, National Chiao Tung University, Hsinchu, Taiwan, R.O.C., June 2009.

[2] K.-C. Hung and D. W. Lin, "Pilot-based LMMSE channel estimation for OFDM systems with power-delay profile approximation," *IEEE Trans. Veh. Technology*, vol. 59, no. 1, pp. 150–159, Jan. 2010

[3] H. Stark and J. W. Woods, *Probability and Random Processes, 3rd ed.* Upper Saddle River, NJ: Prentice-Hall, 2002.

[4] P. Hoeher, S. Kaiser, and P. Robertson, "Two-dimensional pilot-symbol-aided channel estimation by Wiener filtering," in *Proc. IEEE Int. Conf Acoust. Speech Signal Processing*, vol. 3, 1997, pp. 1845–1848.

[5] O. Edfors, M. Sandell, J.-J. van de Beek, S. K. Wilson, and P. O. Borjesson, "OFDM channel estimation by singular value decomposition," *IEEE Trans. Commun.*, vol. 46, no. 7, pp. 931–939, July 1998.

[6] R. van Nee and R. Prasad, *OFDM for Wireless Multimedia Communications.* Boston: Artech House, 2000.

[7] L. Wilhelmsson, B. Bernhardsson, and L. Anderson, "Channel estimation by adaptive interpolation," U.S. patent 7,433,433, Oct. 7, 2008.

[8] Man-On Pun, Michele Morelli, and C.-C. Jay Kuo, "Maximum-likelihood synchronization and channel estimation for OFDMA uplink transmissions," *IEEE Trans. Commun.*, vol. 54, no. 4, pp. 726–736, Apr. 2006.

[9] Lior Eldar, M. R. Raghavendra, S. Bhashyam, Ron Bercovich, and K. Giridhar, "Parametric channel estimation for pseudo-random user-allocation in uplink OFDMA," in *IEEE Int. Conf. Commun.*, vol. 7, 2006, pp. 3035–3039.

[10] IEEE 802.16 Task Group m, *Part 16: Air Interface for Broadband Wireless Access Systems — Advanced Air Interface (working document).* Doc. no. IEEE 802.16m/D9, October 6, 2010.

[11] M.-H. Hsieh, "Synchronization and channel estimation techniques for OFDM systems, "Ph.D. dissertation, Department of Electronics Engineering and Institute of Electronics, National Chiao Tung University, Hsinchu, Taiwan, R.O.C., May 1998.

[12] S. Coleri, M. Ergen, A. Puri, and A. Bahai, "Channel estimation techniques based on pilot arrangement in OFDM systems," *IEEE Trans. Broadcasting,* vol. 48, no. 3, pp. 223–229, Sep. 2002.

[13] V. Erceg *et al.*, "Channel models for fixed wireless applications," IEEE standards contribution no. IEEE 802.16.3c-01/29r4, July 2001.

[14] Hsiung Wei Chang, Liang Chen and Kuang Hui Hsu, *DSP Chip: Fundamental and Application.* (In chinese) Wu Nan, 2004.

[15] B. Farhang-Boroueny, *Adaptive Filters: Theory and Applications.* Wiley, 1998.

七、參考文獻

[1] Chun-Yen Ko, “A study on precoding and equalization for the spatial multiplexing mode of IEEE 802.16m closed-loop MIMO,” M.S. thesis, Department of Electronics Engineering and Institute of Electronics, National Chiao Tung University, July 2011.

[2] Wei-Yu Chen, “Digital signal processor implementation of initial downlink synchronization for IEEE 802.16m,” M.S. thesis, Department of Electronics Engineering and Institute of Electronics, National Chiao Tung University, Sep. 2011.

[3] Po-Sen Wang, Kai-Wei Lu, D. W. Lin, and Pangan Ting, “Quasi-maximum likelihood initial downlink synchronization for IEEE 802.16m,” in *Proc. IEEE Int. Workshop Signal Processing Advances Wirel. Commun.*, June 2011, pp. 506-510.

[4] Chi-Kai Chang, “Digital signal processor implementation of LMMSE channel estimation for IEEE 802.16m,” M.S. thesis, Department of Electronics Engineering and Institute of Electronics, National Chiao Tung University, Aug. 2011.

[5] Kun-Chien Hung and D. W. Lin, “Pilot-based LMMSE channel estimation for OFDM systems with power-delay profile approximation,” *IEEE Trans. Veh. Tech.*, vol. 59, no. 1, pp. 150-159, Jan. 2010.

八、計畫成果自評

研究內容與原計畫相符程度：符合計畫方向，即第四代行動通訊技術之研究。本年度達成之成果包括：雙向中繼技術之研發、IEEE 802.16m 上行測距技術研發、IEEE 802.16m 多輸出入傳收技術研究、IEEE 802.16m 初始下行同步技術之數位訊號處理器軟體實現、以及 IEEE 802.16m 通道估計技術之數位訊號處理器軟體實現等。(補充說明：本計畫為一個二年期計畫之第二年。上一年度的研究成果包括：對 IEEE 802.16m 規範的進一步了解，對寬頻單輸出入及多輸出入無線通道特性、計算軟體、與模擬方式之進一步探討，OFDM 傳送端峰均功率比控制方法與效能之探討，中繼前送技術之研發與分析，分散式中繼系統功率分配方法之研究與效能分析，測距機制之初步設計，以及載波間干擾削減機制之設計與分析，等。兩年度之研究內容中，部份子題有區隔，另外部份則係連續。本年度部份成果係基於上年度之初步研究作進一步之研究而得。)

達成預期目標情況：本計畫達成之貢獻形式，含創新之發現、理論之推導、技術水準之提升、實驗系統之擴充、人才培育(多位碩博士生參與研究)。

成果之學術與應用價值等：

1. 學術價值方面：本計畫獲得若干創新之見，除形成學生學位論文之基礎外，並陸續投稿國際學術會議與期刊中。
2. 應用價值方面：以上成果皆可供相關產研界參考。我們也已本於歷年來在相關領域的研究成果，與國內研發機構進行技術研發與國際標準等方面的合作。此外，我們亦已將部份成果向國內外申請專利。

綜合評估：本計畫獲得不少具有學術與應用價值的成果，並達人才培育之效。成效良好。

國科會補助專題研究計畫項下出席國際學術會議心得報告

日期：99 年 10 月 11 日

計畫編號	NSC 99-2219-E-009-010		
計畫名稱	合作式多輸出入無線通訊之上行傳收器訊號處理技術研究(2/2)		
出國人員姓名	林大衛	服務機構及職稱	交通大學電子工程學系及電子研究所教授
會議時間	2010 年 9 月 26 日 至 2010 年 9 月 29 日	會議地點	土耳其伊斯坦堡(Istanbul)
會議名稱	(中文) IEEE 個人、室內、暨行動無線通訊國際研討會 (英文) IEEE International Symposium on Personal, Indoor, and Mobile Radio Communications		
發表論文題目	(中文) 多輸出入傳輸適用之分散式放大前送中繼網路設計 (英文) Design of Distributed Amplify-and-Forward Relay Network for MIMO Transmission		

一、參加會議經過

二、與會心得

三、考察參觀活動(無是項活動者略)

四、建議

五、攜回資料名稱及內容

六、其他

一、參加會議經過

IEEE 個人、室內、暨行動無線通訊國際研討會(IEEE International Symposium on Personal, Indoor, and Mobile Radio Communications，簡稱 PIMRC)本年係第 21 屆。記得此一會議於十多年前曾在台北舉辦一次，這次則是在土耳其伊斯坦堡。我此次參加該會議，係為發表本系所桑梓賢教授與本人共同指導之博士生吳俊榮與我們二人合著之論文“Design of Distributed Amplify-and-Forward Relay Network for MIMO Transmission”。

本次 PIMRC 係於 2010 年 9 月 26 日(週日)至 9 月 29 日(週三)舉行，主會期在週一至週三，前一天(週日)有幾場 tutorials 和 workshops。因為這些 tutorials 和 workshops 需要另外繳費，故我沒有參加，但到會場去看了一下，其間巧遇大會主席 Prof. Hikmet Sari，談了一會，主要是關於此次會議的一些細節以及法國 Supelec 與交大合作的事。我於多年前結識 Prof. Sari，當時他在工業界工作。他於近年來轉任法國 Supelec 研究所 Advanced Wireless Communications Systems (AWCS) program 的主管。該校最近和本校(交大)簽約合作，本校亦有少數研究生開始赴該校就學。我這次之所以會投稿此一會議，也是因為 Prof. Sari 去年十月來訪交大時，談到他擔任此一會議的主席，並邀我們投稿之故。

我參加了主會期的研討會，其中技術論文發表的部份共分 93 個一般 technical sessions 及 6 個 special sessions，每個 session 長度為 90 或 110 分鐘，視其中發表 5 篇或 6 篇論文而定，總共發表約 500 篇論文。不過主辦單位似乎沒有公布投稿篇數與論文接受率。除論文場次外，本會議還有 4 個 keynote speeches 以及 9 個 panel sessions。四個 keynote speeches 分在兩個 1.5 小時長的依序發表，為數共 108 的 technical sessions、special sessions、和 panel sessions 則分為 10 個時段，各安排 9 至 11 個平行場次同步進行。

伊斯坦堡人口千餘萬，是土耳其第一大城。(第二大城是首都安卡拉，第三是旅遊中心 Izmir。)伊城是歷史名城，不過我國航空公司均沒有飛航。由桃園機場來回伊城，往往需要中停兩次。我此次去程飛機的航線是桃園、新加坡、杜拜、伊斯坦堡，回程經過相反路徑。其中在杜拜雖有上下客，但其他乘客須留在機上進行安檢，不能下機，這和我過去搭機的經驗不同。伊城夏令時間與台灣差五小時。本次去程啟航時間是下午六時餘，在次日上午七時餘抵達伊城，也就是台灣時間過午，航程共費時十八小時左右。約於上午九時抵達旅館，但因尚未有清理好的空房，故不能提早入住，須等到過午。回程啟航時間在伊城時間下午一時半，即台灣時間下午六時半，於次日下午約一時半抵台，航程共費時約十九小時。

這是我第一次去伊斯坦堡。印象深刻的一件事是當地開車速度飛快，如拼命三郎。此外，進入旅館或會場均須經過安檢，顯然是防避恐怖攻擊的措施。會場設施摩登，但有的會議室日照較強，空調顯得不足，或許是設計建造上的疏忽。

二、與會心得

三天的主會期中，前兩天各有兩個 keynote speeches，各分在一個 1.5 小時的場次中依序發表。第一個 keynote 係由 Turkcell 的 CEO Mr. Sureyya Ciliv 先生主講，講題為 Making An Impact Through Technology。Turkcell 是土耳其第一大的行動電話公司，除土耳其本國外，營運範圍另還涵蓋中東地區和前蘇聯的八個國家。它亦是歐洲第三大行動電話公司，共有訂戶

三千餘萬，也是本次會議的主要贊助商之一。Mr. Ciliv 說到該公司深信工程和研發的重要性。他也認為在以下數年中，蜂巢式通訊系統中的尖端無線傳輸率將快速增長。且他認為行動網際網路(mobile Internet)與機對機(machine-to-machine, M2M)通訊將是發展重點，也是 Apple 公司的 iPhone 之所以如此成功的重要因素。他也預期將更針對不同客戶的需要，對不同的小客戶群設計與提供完整的解決方案(total solution)。

第二個 keynote 由 Princeton University 的 Prof. H. Vincent Poor 主講，講題是 The APP and the PHY in Wireless Networks 講，其中 APP 和 PHY 指的是七層通訊協定參考架構中的應用層和實體層。在引言中，Prof. Poor 說到他認為 cooperative communication and competition 和 cross-layer design 為目前無線通訊領域兩大研發方向。接著他就四個技術子題發表演講，基本上是他研究團隊近年的研究課題與成果。四個技術子題是：從實體層消息理論的角度來探討通訊保密與安全問題，有限長度且非零錯誤率之通道容量問題(這是另一個消息理論方面的問題)，分散式感測網路中的學習機制，以及無線網路隨意連結的周延性。總而言之，他是因應用層面需求的啟發而探討實體層的相關理論，大概是四個 keynote speeches 中最為學理性的一個演講，但在消息理論與網路理論方面相當有趣。

第三個 keynote 由 Zigbee Alliance 的 Chairman and CEO Dr. Robert F. Heile 以 Enabling the Smart Grid 為題發表演講。此一主題有關電力網與通訊，是近年來有關電力系統發展的重要議題。電力網的組成與運作包括發電(含集中型與分散型)、負載、電網安全、電力儲存、電動交通工具等議題。Zigbee 在 2008 年完成了一個可用於電力網通訊的標準。目前已有美國已佈設四千餘萬支 Zigbee 電表，跨十一家公用事業公司，成長率為每天三萬七千支，並在繼續成長中。Dr. Heile 還講了一些其他例子。總而言之，透過先進的網路通訊與監測機制，可以提升電力系統的效能與安全，是過去的電力系統所未企及的。

第四個 keynote 由 Georgia Institute of Technology 的 Prof. Ian F. Akyildiz 以 Molecular and Electromagnetic Based Wireless Nanosensor Networks 為題發表演講。此演講內容比較 futuristic。Prof. Akyildiz 表示這一主題其實不是他的核心研究(即通訊)，而是他的「寵物型研究課題(pet project)」。不過他也在主編相關刊物。展望未來，他認為資通訊(IT)時代將於 2030-2040 年左右結束，自 2020 年左右起將是分子時代，且會延續八十年。他在演講中簡速題及若干可能應用，如體內感測器以偵測氣喘、腫瘤等。他又提到若干材料，如非生物性的 carbon nanotubes 及 nanoribbons，還有生物性、分子性的材料。nanosensor 技術是較晚近的研發課題，許多技術還在發展中，仍面對許多挑戰。

學術論文發表方面，六個 special sessions 的內容和我近年的研究之關係較弱。93 個 technical sessions 分為 Fundamentals and PHY、Mobile and Wireless Networks、MAC and Cross Layer Design、及 Services, Applications and Business 四個領域系列(tracks)。我注意的是傳輸訊號處理領域的論文，此類論文集中在前兩個領域系列中。我所發表的論文，也就屬於第一個領域系列。三天會期中，此二領域系列都有多場平行場次，我自是選擇最適者參加，場次主題包括合作式通訊、通訊訊號處理、LTE 標準相關之訊號處理、多輸出入傳輸、同步、天線波束成型等。技術性細節在此不談。我也參加了兩個 panel sessions，一個題目是 IMT-Advanced: Candidate Technologies, Evaluation and Further Steps，另一個題目是 Deployment of Femto and Small Cells，兩個場次都是除主席外有四個 panelists。第一個場次除一位 panelist 比較著重 IEEE

802.16m(這也難怪，因為他是 IEEE 802.16 Working Group 的 ITU-R Liaison Group Chair)，其他人都著重 LTE。兩者氣勢上的差異，或許由此可見。可惜的是，兩場 panel sessions 的演講內容似乎都偏重概念性的介紹，缺少深入的量化數據呈現與分析或是深入的技術評析，不免令我有點遺憾。

三、考察參觀活動：無

四、建議：無

五、攜回資料名稱及內容

會議議程(紙本)一冊，論文集(光碟)一張。

Prof. D. W. Lin

寄件者: EDAS Conference Manager [help@edas-help.com] 代理 Hakan Delic [delic@boun.edu.tr]
寄件日期: 2010年5月24日星期一 上午 4:33
收件者: Chun-Jung Wu
副本: David Lin; Tzu-Hsien Sang
主旨: [PIMRC 2010 Track 1] Your paper #1569307207 has been accepted

類別: accepted

Dear Mr. Chun-Jung Wu:

Congratulations - your paper #1569307207 ('Design of Distributed Amplify-and-Forward Relay Network for MIMO Transmission') for PIMRC 2010 Track 1 has been accepted and will be presented in the session titled .

The reviews are below or can be found at http://edas.info/showPaper.php?m=1569307207.

======= Review 1 =======

> *** Relevance and timeliness: Rate the importance and timeliness of the topic addressed in the paper within its area of research.
Excellent (5)

> *** Technical content and scientific rigour: Rate the technical
> content of the paper (e.g.: completeness of the
analysis or simulation study, thoroughness of the treatise, accuracy of the models, etc.), its soundness and scientific rigour.
Valid work but limited contribution. (3)

> *** Novelty and originality: Rate the novelty and originality of the ideas or results presented in the paper.
Some interesting ideas and results on a subject well investigated. (3)

> *** Quality of presentation: Rate the paper organization, the clearness of text and figures, the completeness and accuracy of references.
Readable, but revision is needed in some parts. (3)

> *** Submission Policy: Does the paper list the same author(s), title and abstract in its PDF file and EDAS registration?

Same authors.

> *** Strong aspects: Comments to the author: what are the strong aspects of the paper?

The work investigates ergodic capacity of MIMO systems aided by multiple relays. Previous work concentrated on single relay.

> *** Weak aspects: Comments to the author: what are the weak aspects of the paper?

The authors considered only extreme cases i)source-relays channels dominating, or ii)relay-destination channels dominating. Not a typical case in between, which is more crucial in my opinion.

> *** Recommended changes: Recommended changes. Please indicate any changes that should be made to the paper if accepted.

In first sentence of the second paragraph of the section II "that" should be removed. One of the lines of equation 1 should be removed.

======= Review 2 =======

> *** Relevance and timeliness: Rate the importance and timeliness of the topic addressed in the paper within its area of research.
Good (4)

> *** Technical content and scientific rigour: Rate the technical
> content of the paper (e.g.: completeness of the
analysis or simulation study, thoroughness of the treatise, accuracy of the models, etc.), its soundness and scientific rigour.
Valid work but limited contribution. (3)

> *** Novelty and originality: Rate the novelty and originality of the ideas or results presented in the paper.
Some interesting ideas and results on a subject well investigated. (3)

> *** Quality of presentation: Rate the paper organization, the clearness of text and figures, the completeness and accuracy of references.
Well written. (4)

> *** Submission Policy: Does the paper list the same author(s), title and abstract in its PDF file and EDAS registration?

Yes

> *** Strong aspects: Comments to the author: what are the strong aspects of the paper?

A distributed relay-enhanced MIMO transmission scheme is designed to maximize the system capacity. An upper bound of the capacity is derived and used as the optimization target. Besides, suboptimal solutions are proposed combining relay selection with optimal setting of relay gains. The simulation results show that the proposed scheme performs better in terms of capacity and diversity order.

> *** Weak aspects: Comments to the author: what are the weak aspects of the paper?

1. In a distributed relay network, how to ensure the synchronization among relays geographically isolated?
2. The authors assume the relays know the relevant channel coefficients, but do not clarify the specific kind of coefficient and why this assumption is reasonable.
3. The authors claim the diversity order of the proposed scheme is similar to that of a single-hop MIMO antenna-selection system, but there is no relevant analysis and illustration.
4. In Theorem 1 and 2, the authours prove that C(sR) > C(R) for norm(s)> 1 and C(sR) is upper-bounded when norm(s)->inf. However, the montonicity is not proved, and the prove is insufficient.
5. In Appendix A, there is a mistake in Eq. (28).
6. In Appdedix A, why the last part on the right hand of Eq. (29) is nonnegative?

> *** Recommended changes: Recommended changes. Please indicate any changes that should be made to the paper if accepted.

1. In a distributed relay network, how to ensure the synchronization among relays geographically isolated?
2. The authors assume the relays know the relevant channel coefficients, but do not clarify the specific kind of coefficient and why this assumption is reasonable.
3. The authors claim the diversity order of the proposed scheme is similar to that of a single-hop MIMO antenna-selection system, but there is no relevant analysis and illustration.
4. In Theorem 1 and 2, the authours prove that C(sR) > C(R) for norm(s)> 1 and C(sR) is upper-bounded when norm(s)->inf. However, the montonicity is not proved, and the prove is insufficient.
5. In Appendix A, there is a mistake in Eq. (28).
6. In Appdedix A, why the last part on the right hand of Eq. (29) is nonnegative?

======= Review 3 =======

> *** Relevance and timeliness: Rate the importance and timeliness of the topic addressed in the paper within its area of research.
Good (4)

> *** Technical content and scientific rigour: Rate the technical
> content of the paper (e.g.: completeness of the
analysis or simulation study, thoroughness of the treatise, accuracy of the models, etc.), its soundness and scientific rigour.
Solid work of notable importance. (4)

> *** Novelty and originality: Rate the novelty and originality of the ideas or results presented in the paper.
Some interesting ideas and results on a subject well investigated. (3)

> *** Quality of presentation: Rate the paper organization, the clearness of text and figures, the completeness and accuracy of references.
Readable, but revision is needed in some parts. (3)

> *** Submission Policy: Does the paper list the same author(s), title and abstract in its PDF file and EDAS registration?

Yes, it is.

> *** Strong aspects: Comments to the author: what are the strong aspects of the paper?

The authors performed a design of distributed AF relay network for MIMO transmission which is quite interesting. They presented suboptimal solution for that.
The results were compared with antenna selection counterpart.

> *** Weak aspects: Comments to the author: what are the weak aspects of the paper?

1. The authors stated that the contribution has never been considered and they did not cite new references. The newest one is in 2008.

2. It is worth to consider a distributed antenna array in one side of the transmission (TX or Rx) too.

3. Could you please rewrite Eq. (5), you have to mention the left side of the equation, what is the arg which maximizes C(R)??

4. The authors considered two types of noise domination, what about same properties (power)?

5. It is better to reformulate the introduction where a contribution section should be underlined.

> *** Recommended changes: Recommended changes. Please indicate any changes that should be made to the paper if accepted.

See Weak aspects.

======== Review 4 ========

> *** Relevance and timeliness: Rate the importance and timeliness of the topic addressed in the paper within its area of research.
Good (4)

> *** Technical content and scientific rigour: Rate the technical
> content of the paper (e.g.: completeness of the
analysis or simulation study, thoroughness of the treatise, accuracy of the models, etc.), its soundness and scientific rigour.
Marginal work and simple contribution. Some flaws. (2)

> *** Novelty and originality: Rate the novelty and originality of the ideas or results presented in the paper.
Minor variations on a well investigated subject. (2)

> *** Quality of presentation: Rate the paper organization, the clearness of text and figures, the completeness and accuracy of references.
Substantial revision work is needed. (2)

> *** Submission Policy: Does the paper list the same author(s), title and abstract in its PDF file and EDAS registration?

Yes

> *** Strong aspects: Comments to the author: what are the strong aspects of the paper?

The paper deals with design and analysis of a 2-hop system with multiple relays. In particular, optimization of relay gains are investigated for maximization of the capacity. Some analytical and numerical results are presented.

> *** Weak aspects: Comments to the author: what are the weak aspects of the paper?

According to me, the paper is not written well and misses a pointed structure. For example, an important part of the analysis is based on the relay-selection, but there is not enough emphasis on this point in the Abstract and in the Introduction. Furthermore, the motivation for using the relay-selection is not explained well.

The literature review should be improved.

> *** Recommended changes: Recommended changes. Please indicate any changes that should be made to the paper if accepted.

The first line of Eq.(1) should be removed. Eq.(2) cannot be followed by the reader. Also, Eq.(2) is the same as Eq.(6).

Regards,
Stefan Kaiser, Mutlu Koca, Geert Leus, Heidi Steendam PIMRC 2010 Track 1 Co-Chairs

Design of Distributed Amplify-and-Forward Relay Network for MIMO Transmission

Chun-Jung Wu, David W. Lin, and Tzu-Hsien Sang
Department of Electronics Engineering and Institute of Electronics
National Chiao Tung University, Hsinchu, Taiwan 30010, ROC
E-mails: cjwu.ee91g@nctu.edu.tw, dwlin@mail.nctu.edu.tw, tzuhsien54120@faculty.nctu.edu.tw

***Abstract*—We consider the design of a multi-input multi-output (MIMO) transmission system equipped with distributed, single-antenna amplify-and-forward relays. In particular, we consider how to optimize the complex forwarding coefficients of the relays to maximize the system capacity. Existing studies on MIMO relay network designs mostly concentrate on the case of single relay with multiple antennas, whose results are not applicable to distributed networks. We first analyze how the system capacity relates to the relay transmission powers and the channel coefficients. An upper bound on the asymptotic capacity at high relay powers is derived. Aided by the capacity results, we consider the optimization of relay coefficients under two noise conditions: that where the destination noise dominates the total noise and that where the relay noise dominates the total noise. It turns out that no simple analytic solutions can be found for all relay network sizes. Therefore, we propose suboptimal solutions that involve computation of optimal relay coefficients with optimal selection of relays for network sizes that can be solved analytically. The results on diversity order are found to show resemblance to that for single-hop MIMO systems employing antenna selection. Simulation results also verify the superior performance of the proposed technique.**

I. Introduction

There is a recent surge in studies of relay-aided multi-input multi-output (MIMO) transmission due to its potentials in answering to the ever-rising quest for higher mobile data speed. The primary uses of relays, as envisioned by many, are to enhance coverage and capacity. To preserve the degree of freedom available in a MIMO system, in such relay-aided MIMO transmission it is natural to consider using a relay with multiple antennas or using a relay network.

For the case of single relay equipped with multiple antennas, both single-input single-output (SISO) [1] and MIMO [2], [3] end-to-end transmissions have been considered. To fully exploit the advantage that may be offered by the relay, suitable beamforming over the multiple relay antennas is needed for both the backward and the forward MIMO channels. One disadvantage of the single-relay architecture is its lack of spatial or system diversity. When the single relay is in an outage condition due to fading or other reasons, the relaying link breaks. A reasonable alternative, therefore, is to employ geographically scattered multiple single-antenna relays for better diversity. However, the advantage in diversity comes at the cost of greater difficulty in beamforming compared to using a single multi-antenna relay, as subsequent discussion will further demonstrate.

For the case of multiple single-antenna relays, i.e., the case of a distributed single-antenna relay network, the most straightforward design conceivable of the relay gains (i.e., relay coefficients) is to assign identical gains to all relays subject to some power limit. This has been termed the *all-pass* scheme [4]. Some have studied the ergodic characteristics of capacity under simple designs like the all-pass [5]. But how to effect good designs of the relay gains remains a problem to be further looked into.

In this work, we consider the design of distributed single-antenna amplify-and-forward (AF) relay networks. In particular, we consider the optimization of the relay forwarding coefficients for maximization of the Shannon capacity of the system. We aim at an analytical solution of the problem, although it will be seen later that there are limits to what can be achieved by analysis. We assume that the relays know the relevant channel coefficients (or channel state information, CSI).

First, we examine the dependence of capacity on the relay transmission powers and the channel coefficients. Due to the use of AF, both the signal power and the relay noise are scaled by the relay forwarding coefficients. We show that the capacity increases with the relay output powers, but there is an upper bound to its asymptotic value at the limit of very high relay powers. The analysis also helps to guide the subsequent relay network design. In relay network design, we note that there are two noise terms that impact the system performance, namely, the relay noise and the destination noise. We find that an analytical characterization of the optimal solution and the performance bound can be obtained when either noise dominates the total noise and when the number of relays are of certain particular values. Based on these observations, we thus propose suboptimal designs that optimize the relay forwarding coefficients with proper relay section.

The resulting performance of the proposed designs shows close resemblance to that of MIMO systems with antenna selection [6], [7], which have been developed to reduce the complexity of the MIMO transceiver without sacrificing the diversity order by activating only a subset of the transmitter or the receiver antennas. In [7], the outage diversity with

This study was conducted under the Wireless Broadband Communications Technology and Application Project of the Institute for Information Industry, which has been subsidized by the Ministry of Economic Affairs of the Republic of China, and under Grant NSC 98-2219-E-009-012 of the National Science Council of the Republic of China.

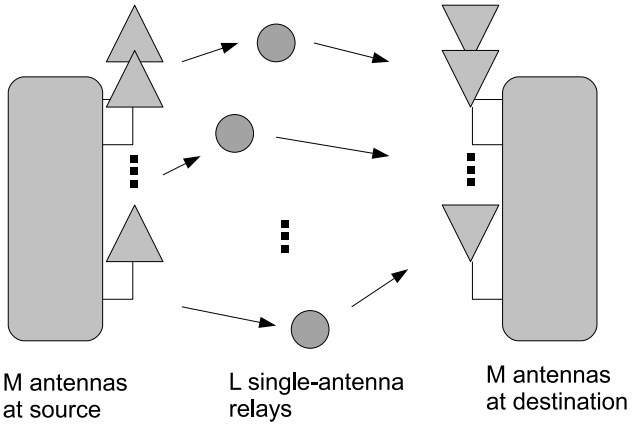

Fig. 1. MIMO system with distributed relays.

antenna selection is shown to be similar to a full-complexity MIMO system (i.e., without antenna selection). Further approximations to capacity distribution and performance loss of antenna selection have been conducted in [8] and [6]. Thanks to this analogy we may predict that a relay-selection system with optimal setting of relay forwarding coefficients would have similar performance characteristics to the better-studied MIMO antenna-selection systems.

In what follows, Sec. II describes the system model and considers its Shannon capacity. Sec. III discusses the optimization of relay coefficients. Sec. IV presents and elaborates on some numerical results. And Sec. V is the conclusion.

II. System Model and Capacity Analysis

We consider a distributed MIMO relay system composed of one source terminal, one destination terminal, and L single-antenna relays. The source and the destination terminals are both equipped with M antennas. The relays simply amplify the received signals from the source (with possibly different complex gain coefficients) and transmit the amplified signals to the destination. Hence the destination terminal would receive both the amplified signals and the amplified relay noises. To preserve the degree of freedom provided by the source and the destination terminals, we assume $L \geq M$. Fig. 1 illustrates the system model.

Let $\boldsymbol{x} \in \mathbb{C}^M$ and $\boldsymbol{y} \in \mathbb{C}^M$ denote the signals transmitted from the source terminal and received by the destination terminal, respectively, where $\mathbb{C}$ denotes the set of complex numbers. Let $\boldsymbol{G}^H \in \mathbb{C}^{L\times M}$ be the matrix of MIMO channel coefficients between the source terminal antennas and the relays, where superscript H denotes Hermitian transpose. Similarly, let $\boldsymbol{F} \in \mathbb{C}^{M\times L}$ be the channel matrix between the relays and the destination terminal antennas. The received signals at the relays are assumed to be subject to additive complex circular white Gaussian noise (AWGN) $\boldsymbol{n}_R \sim \mathcal{CN}(0, \sigma_R^2 \boldsymbol{I}_L)$, where $\boldsymbol{I}_L$ denotes the $L \times L$ identity matrix. Likewise, the received signals at the destination are interfered by AWGN $\boldsymbol{n}_D \sim \mathcal{CN}(0, \sigma_D^2 \boldsymbol{I}_M)$.

Upon receiving the (composite) signal from the source, the ith relay applies a complex gain $r(i) \in \mathbb{C}$. Let $\boldsymbol{r} = [r(i), \cdots, r(L)]^T$ represent the gain vector of the relay network, where superscript T stands for matrix transpose. Assume that no direct link exists between the source and the destination. The end-to-end transmission behavior can be written as

$$\boldsymbol{y} \;=\; \boldsymbol{FRG}^H\boldsymbol{x} + \boldsymbol{FRn}_R + \boldsymbol{n}_D \tag{1}$$

where $\boldsymbol{R} = \mathrm{diag}(\boldsymbol{r})$ with $\mathrm{diag}(\boldsymbol{r})$ denoting a diagonal matrix formed of the elements of vector $\boldsymbol{r}$.

In any practical design, the transmission powers of the source terminal and the relays are limited. Therefore, we assume that the source transmits independent streams over its M antennas with equal power σ_x^2. On the other hand, assume that the relay network is subject to a total power limit P_R. Hence we have

$$\begin{aligned} P_R \;&\geq\; \mathrm{tr}(\mathrm{E}\{(\boldsymbol{RG}^H\boldsymbol{x} + \boldsymbol{Rn}_R)(\boldsymbol{RG}^H\boldsymbol{x} + \boldsymbol{Rn}_R)^H\}) \\ &=\; \sum_{i=1}^{L}(\sigma_R^2 + \sigma_x^2\|\boldsymbol{g}_i\|^2)|r(i)|^2, \end{aligned}$$

where $\|\cdot\|$ denotes the 2-norm of a vector and $\boldsymbol{g}_i$ represents the ith column of $\boldsymbol{G}$, which is a vector of the complex conjugates of the channel coefficients between the source antennas and the ith relay.

A. System Capacity

The noise vector $\boldsymbol{FRn}_R + \boldsymbol{n}_D$ in (1) received at the destination is in general spatially correlated. To find the system capacity, consider using a noise whitening filter $\boldsymbol{W}^{-1/2}$ at the destination, where $\boldsymbol{W}$ is the autocorrelation matrix of the noise given by

$$\begin{aligned} \boldsymbol{W} \;&=\; \mathrm{E}\{(\boldsymbol{FRn}_R + \boldsymbol{n}_D)(\boldsymbol{FRn}_R + \boldsymbol{n}_D)^H\} \\ &=\; \sigma_D^2\boldsymbol{I}_M + \sigma_R^2(\boldsymbol{FR})(\boldsymbol{FR})^H. \end{aligned} \tag{2}$$

Let $\boldsymbol{H} \triangleq \boldsymbol{FRG}^H$ denote the noise-free equivalent end-to-end channel matrix. The system capacity is then a function of $\boldsymbol{R}$ as [9]

$$\mathrm{C}(\boldsymbol{R}) \triangleq \log\det(\boldsymbol{I}_M + \sigma_x^2\boldsymbol{H}^H\boldsymbol{W}^{-1}\boldsymbol{H}) \tag{3}$$

where $\det(\cdot)$ denotes the matrix determinant and $\log$ stands for base-2 logarithm. The optimization problem can be stated as

$$\boldsymbol{R}_{opt} = \arg\max_{\boldsymbol{R}} \mathrm{C}(\boldsymbol{R}) \tag{4}$$

subject to

$$P_R \geq \sum_{i=1}^{L}(\sigma_R^2 + \sigma_x^2\|\boldsymbol{g}_i\|^2)|r(i)|^2. \tag{5}$$

B. Power Scaling and Capacity

The inequality power constraint (5) naturally prompts one to think: is it possible to simplify the constraint by considering only the equality therein without impacting the optimality of the solution? Or, alternatively, given a certain $\boldsymbol{r}$ that satisfies (5) with inequality, will the system capacity be increased by scaling $\boldsymbol{r}$ to reach equality in (5)? Intuitively, the answer may

seem to be a no-brainer as increasing the transmission power should be beneficial to the signal-to-noise ratio (SNR) and thus the capacity. But mathematically, due to the presence of some matrices in (3) and (1), a solid proof nevertheless requires a little work. We give the proof in Appendix A. (Some intermediate results in the proof will also have use later in system design.) For convenience, we state the result as a theorem.

Theorem 1 (Capacity scaling): When the (complex) relay gains $\boldsymbol{R}$ are scaled by $s \in \mathbb{C}$ with $|s| > 1$, $\mathrm{C}(s\boldsymbol{R}) > \mathrm{C}(\boldsymbol{R})$.

Therefore, we confirm that scaling up of the relay gains can increase system capacity. Hence we may simplify the optimization constraint to

$$P_R = \sum_{i=1}^{L} (\sigma_R^2 + \sigma_x^2 \|\boldsymbol{g}_i\|^2) |r(i)|^2. \tag{6}$$

That is, the relays should transmit at the maximum allowed total power.

Next, one may wonder if the capacity could increase without bound if the total relay transmission power tends to infinity. Intuitively, the answer may appear to be another no-brainer because, from (1), the quality of the source-to-relay links should place a cap on the amount of information rate that the system can support, however much the relay transmission power can be. But again, a solid mathematical proof requires a few lines of reasoning. Again for convenience, we state the result as a theorem below and prove it in Appendix B.

Theorem 2 (Asymptotic capacity with high relay power): As $|s| \to \infty$, $\mathrm{C}(s\boldsymbol{R})$ is upper-bounded by

$$\log\det[\boldsymbol{I}_M + (\frac{\sigma_x}{\sigma_R})^2 \boldsymbol{G}\boldsymbol{G}^H]$$

and it approaches the upper bound if and only if $\boldsymbol{G}$ and $\boldsymbol{F}\boldsymbol{R}$ span the same row space.

With Theorem 2, it is verified that $\mathrm{C}(\boldsymbol{R})$ is upper-bounded irrespective of the power level of the relays.

III. Relay Network Design for Two Types of Noise Domination

We now consider how to design the relay coefficients for maximization of the system capacity. Directly solving (4) seems difficult because the diagonal nature of matrix $\boldsymbol{R}$ rules out conventional beamforming-based solutions [2]. While algorithms can always be developed to facilitate a solution of the problem via computation, an analytical solution may give more insights to the nature of the optimizing solutions. The latter is the approach taken in this work. For this, note first that the system performance depends on two noise terms, namely, the relay noise vector $\boldsymbol{n}_R$ and the destination noise vector $\boldsymbol{n}_D$. The problem becomes much more tractable when one of them dominates. In what follows we concentrate on these two simplified scenarios and attempt at the corresponding solutions of optimal relay gains.

A. Destination Noise-Dominating: Relay Selection and Power Allocation

When $\sigma_D \gg \sigma_R$, from (2) we have $\boldsymbol{W} \approx \sigma_D^2 \boldsymbol{I}$. Thus from (3) we get

$$\begin{aligned} \mathrm{C}(\boldsymbol{R}) &\approx \log\det[\boldsymbol{I}_M + (\frac{\sigma_x}{\sigma_D})^2 \boldsymbol{H}^H \boldsymbol{H}] \\ &\triangleq \mathrm{C}_D(\boldsymbol{R}). \end{aligned} \tag{7}$$

Hence the capacity is nearly that of an $M \times M$ MIMO system with an end-to-end channel matrix $\boldsymbol{H}$ at SNR $= (\sigma_x/\sigma_D)^2$. Even in this simplified condition, a simple general solution that maximizes $\mathrm{C}_D(\boldsymbol{R})$ for $L > M$ is, to the best of our knowledge, not available. Nor is the efficient technique for maximization of matrix determinant through convex optimization under linear matrix inequality constraints [11] applicable. However, we find that an analytical solution can be obtained for $L = M$ under high SNR. To proceed, therefore, we first develop the solution for this condition. The solution can be applied to the condition $L > M$ to select good relays.

Let $\rho_i(\boldsymbol{H}^H \boldsymbol{H})$ denote the ith largest eigenvalue of $\boldsymbol{H}^H \boldsymbol{H}$. With $L = M$ and under a high end-to-end SNR, we have

$$\begin{aligned} \mathrm{C}_D(\boldsymbol{R}) &\approx \log\det[(\frac{\sigma_x}{\sigma_D})^2 \boldsymbol{H}^H \boldsymbol{H}] \\ &= \log[(\frac{\sigma_x}{\sigma_D})^2 \det(\boldsymbol{F}\boldsymbol{F}^H) \det(\boldsymbol{G}\boldsymbol{G}^H) \det(\boldsymbol{R}\boldsymbol{R}^H)]. \end{aligned} \tag{8}$$

So we need to find $\boldsymbol{R}$ to maximize $\det(\boldsymbol{R})$ subject to the power constraint (6). Equivalently we may do

$$\max_{\boldsymbol{r}} \prod_i |r(i)|^2 \tag{9}$$

subject to

$$P_R = \sum_{i=1}^{L} (\sigma_R^2 + \sigma_x^2 \|\boldsymbol{g}_i\|^2) |r(i)|^2 \approx \sigma_x^2 \sum_i \|\boldsymbol{g}_i\|^2 |r(i)|^2. \tag{10}$$

Employing the Lagrange multiplier technique leads to the relay power allocation

$$|r_{opt}(i)| = \sqrt{\frac{P_R}{M\sigma_x^2 \|\boldsymbol{g}_i\|^2}}. \tag{11}$$

When $L > M$, we can do relay selection by choosing M relays out of the L such that (8) is maximized.

It is of interest to note that, under the above solution, the product of the last two determinant terms in the right-hand-side (RHS) of (8) is upper-bounded as

$$\begin{aligned} \det(\boldsymbol{G}\boldsymbol{G}^H) \det(\boldsymbol{R}\boldsymbol{R}^H) &= \frac{\det(\boldsymbol{G}\boldsymbol{G}^H)}{\prod_i \|\boldsymbol{g}_i\|^2} (\frac{P_R}{M\sigma_x^2})^M \\ &\le (\frac{P_R}{M\sigma_x^2})^M. \end{aligned} \tag{12}$$

The last inequality can be shown by considering QR decomposition of $\boldsymbol{G}$. Let $\boldsymbol{R}_G$ denote the triangular matrix in the decomposition. Then $\det(\boldsymbol{G}\boldsymbol{G}^H) = \prod_i |\boldsymbol{R}_G(i,i)|^2$ where $\boldsymbol{R}_G(i,i)$ is the ith diagonal element of $\boldsymbol{R}_G$. Apparently, $|\boldsymbol{R}_G(i,i)|^2 \le \|\boldsymbol{r}_{G_i}\|^2$ where $\boldsymbol{r}_{G_i}$ denotes the ith column of

$\boldsymbol{R}_G$. But $\|\boldsymbol{r}_{G_i}\|^2 = \|\boldsymbol{g}_i\|^2$ because $\boldsymbol{R}_G$ and $\boldsymbol{G}$ are related by a unitary transform. Thus the result. For convenience, define loss factor

$$L_F = \prod_i \frac{|\boldsymbol{R}_G(i,i)|^2}{\|\boldsymbol{g}_i\|^2}. \tag{13}$$

We have $L_F \leq 1$, with equality if $\boldsymbol{G}^H\boldsymbol{G}$ is diagonal.

B. Relay Noise-Dominating: Relay Selection and Distributed Beamforming

If $\sigma_R \gg \sigma_D$, then from (19) and (21) in Appendix A we have

$$\begin{aligned} \mathrm{C}(\boldsymbol{R}) &\approx \log\det\{\boldsymbol{I}_M + (\frac{\sigma_x}{\sigma_R})^2 \boldsymbol{G}\boldsymbol{V}\boldsymbol{V}^H\boldsymbol{G}^H\} \\ &\triangleq \mathrm{C}_R(\boldsymbol{R}) \end{aligned} \tag{14}$$

where $\boldsymbol{V} \in \mathbb{C}^{L\times M}$ is the matrix of right singular vectors of $\boldsymbol{F}\boldsymbol{R}$ with its ith column corresponding to the ith largest singular value of $\boldsymbol{F}\boldsymbol{R}$. Comparing with (30) in Appendix B, we see that the situation is similar to that with very high relay transmission power. Hence by Theorem 2, $\mathrm{C}_R(\boldsymbol{R})$ is maximized if the relay setting can be such that $\boldsymbol{F}\boldsymbol{R}$ spans the same row space as $\boldsymbol{G}$. Note that, contrary to the case where $\sigma_D \gg \sigma_R$, in the present case the relay power distribution is not critical to the performance; only the row space of $\boldsymbol{F}\boldsymbol{R}$ matters. In other words, we have a problem of beamforming under a distributed relay network that should try to align the row space of $\boldsymbol{F}\boldsymbol{R}$ with that of $\boldsymbol{G}$.

To proceed, let $\boldsymbol{f}_i^H$ denote the ith row of $\boldsymbol{F}$. Let $\boldsymbol{V}_N \in \mathbb{C}^{L\times(L-M)}$ be a matrix of basis vectors for the orthogonal complement of the row space of $\boldsymbol{G}$; that is, $\boldsymbol{G}\boldsymbol{V}_N^H = 0$. And let $\boldsymbol{\Phi}_i = \mathrm{diag}(\boldsymbol{f}_i^H)\boldsymbol{V}_N$. Immediately we have

$$\begin{aligned} \boldsymbol{j}_i(\boldsymbol{r}) &\triangleq \boldsymbol{f}_i^H\boldsymbol{R}\boldsymbol{V}_N \\ &= \boldsymbol{r}^T\,\mathrm{diag}(\boldsymbol{f}_i)\boldsymbol{V}_N = \boldsymbol{r}^T\boldsymbol{\Phi}_i,\ i \in \{1,\ldots,M\}. \end{aligned} \tag{15}$$

To make the row space of $\boldsymbol{F}\boldsymbol{R}$ equal to that of $\boldsymbol{G}$, we should make $\boldsymbol{j}_i(\boldsymbol{r}) = 0\ \forall i$. For this, collect $\boldsymbol{\Phi}_i\ \forall i$ to form

$$\boldsymbol{\Phi} \triangleq [\boldsymbol{\Phi}_1\ \boldsymbol{\Phi}_2\ \cdots\ \boldsymbol{\Phi}_M] \in \mathbb{C}^{L\times M(L-M)}. \tag{16}$$

Then $\boldsymbol{r}$ is an optimal solution that maximizes $\mathrm{C}_R(\boldsymbol{R})$ if $\boldsymbol{r}^T\boldsymbol{\Phi} = 0$. The existence of such a solution would require $M(L-M) < L$ if $\boldsymbol{\Phi}$ is of full rank.

Recall that we have assumed $L \geq M$. When $L = M+1$, the inequality $M(L-M) < L$ holds and the existence of a maximizing solution $\boldsymbol{r}$ is guaranteed. There is more than one way to solve for the optimal $\boldsymbol{r}$, which we will not elaborate here. When $L > M+1$, the upper bound on $\mathrm{C}_R(\boldsymbol{R})$ (as indicated in Theorem 2) is unreachable. But there still exists an optimal $\boldsymbol{r}$ that maximizes $\mathrm{C}_R(\boldsymbol{R})$, only that a closed-form solution is not available. A suboptimal design is to consider all possible combinations of $M+1$ relays and pick the combination with the best performance. Note that the determination of the best relay combination does not require solution of the optimal $\boldsymbol{r}$ in each case. It can be achieved by comparing the performance upper bounds given in (31). Then the optimal $\boldsymbol{r}$ for the best relay selection can be derived based on the above-discussed methods for $L = M+1$.

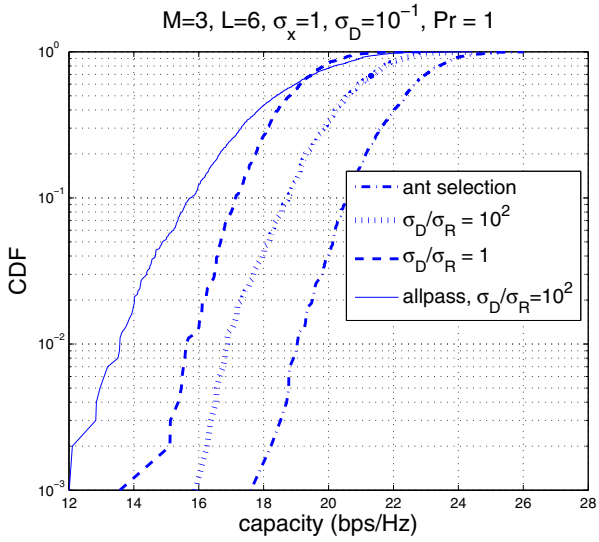

Fig. 2. MIMO system with distributed relays in destination noise-dominating condition.

IV. Numerical Results

To verify and further analyze the performance of the proposed technique, we simulate relay-aided MIMO transmission. The channel matrices $\boldsymbol{F}$ and $\boldsymbol{G}$ are both $M \times L$ complex Gaussian matrices with i.i.d. entries distributed according to $\mathcal{CN}(0,1)$. Besides the relay-selection systems proposed in Sec. III, for benchmarking purpose we also consider the all-pass systems as a conceivable example of simple network designs. In addition, a single-hop MIMO system based on antenna selection is also simulated for comparison of the associated diversity orders. We illustrate the performance of different schemes in terms of the cumulative distributions functions (CDFs) of their capacities.

Figs. 2 and 3 show the system performance in the destination noise-dominating condition. In Fig. 2, we see that as the relay noise increases, the capacity drops (i.e., the CDF curve shifts to the left). As expected, the all-pass design results in much worse performance than the proposed design. Examining the slopes of the CDF curves, we see that the system with distributed relays shows the same diversity order as the single-hop system with antenna selection. Fig. 3 shows the performance under different numbers of relay. We see that the diversity order grows with the size of the relay network, as can also be appreciated by comparing the slopes of the corresponding CDF curves with that for single-hop antenna-selection systems. In both Figs. 2 and 3, there are capacity gaps between relay systems and corresponding antenna-selection systems, which arise due to the loss factor L_F.

Now consider the performance under the relay noise-dominating condition. Fig. 4 shows how the performance varies with different relative noise levels. A characteristical difference between the system performance in this condition and that shown in Fig. 2 is the apparent loss of diversity order as the destination noise becomes large. This should be the

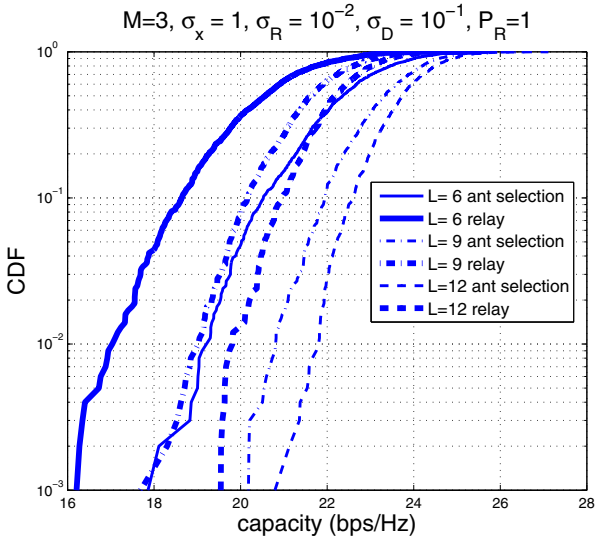

Fig. 3. MIMO system with distributed relays in destination noise-dominating condition: performance with different relay network sizes.

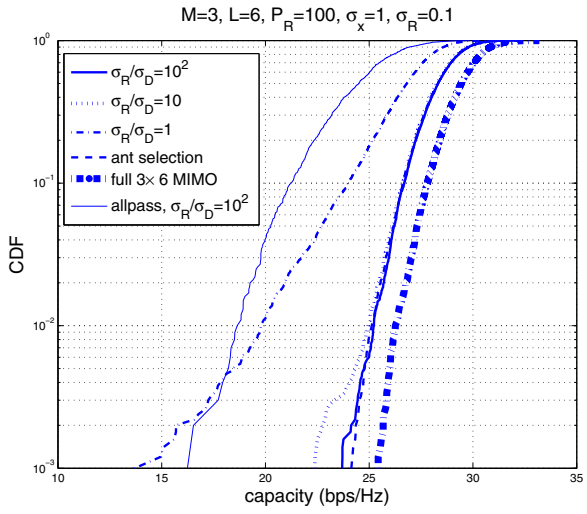

Fig. 4. MIMO system with distributed relays in relay noise-dominating condition.

consequence of mismatch between the actual noise condition (that the relay noise is not dominating) and the assumed condition (that the relay noise dominates) under which the solution is obtained. Nevertheless, with sufficiently dominating relay noise (such as when $\sigma_R/\sigma_D = 10$ or 100), the diversity performance becomes close to that of an antenna-selection system, which in turn has a similar performance in diversity order as a full MIMO system (the "full 3×6 MIMO" curve in the plot), only a lower beamforming gain. In addition, the capacity of the all-pass design still falls significantly below that of the proposed design mostly. In Fig. 5, we see that the performance of the proposed design is tightly upper-bounded by the corresponding antenna-selection system (assuming equal number of antennas to select from as there are relays), and the diversity order again grows with the size of the relay network in a similar way to an antenna-selection system.

V. Conclusion

We considered the design of distributed relay networks to aid MIMO transmission, where a major point in considering a distributed relay network instead of a single multi-antenna relay was the potential to effect a better diversity performance. An analytical solution was attempted, though it turned out that such analytical solutions could only be obtained for a limited number of conditions. Nevertheless, these analytical results facilitated suboptimal designs that could exploit the diversity order afforded by the relay network to a similar degree to that of a single-hop MIMO antenna-selection system. The proposed suboptimal designs employed relay selection with optimal setting of relay gains. Simulation results were presented which demonstrated the diversity order performance of the proposed designs and its superior performance compared to the simple all-pass design.

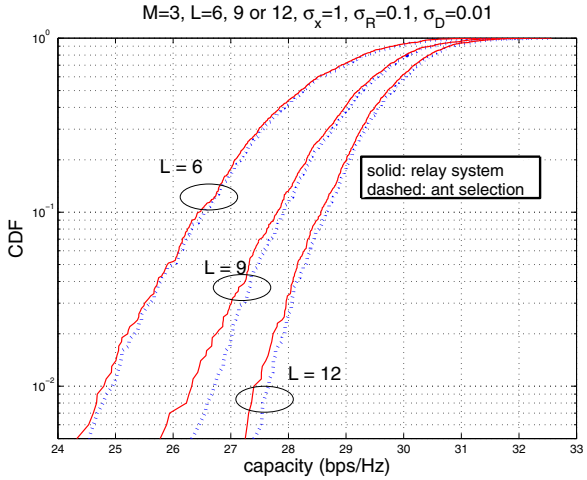

Fig. 5. MIMO system with distributed relays in relay noise-dominating condition: performance with different relay network sizes.

Appendix A
Proof of Theorem 1

First, it is clear in (3) that $\mathrm{C}(s\boldsymbol{R}) = \mathrm{C}(|s|\boldsymbol{R})$. Without loss of generality we assume $s \in \mathbb{R}^+$ (the set of positive real numbers) hereafter.

Consider a singular value decomposition of $\boldsymbol{FR}$ given by

$$\boldsymbol{FR} = \boldsymbol{U}\boldsymbol{\Lambda}\boldsymbol{V}^{\boldsymbol{H}} \tag{17}$$

where for convenience we let $\boldsymbol{\Lambda}$ be $M \times M$. Thus $\boldsymbol{U} \in \mathbb{C}^{M\times M}$ is the matrix of left singular vectors as usual, but the matrix of right singular vectors $\boldsymbol{V}$ becomes $L \times M$, that is, $\boldsymbol{V} \in \mathbb{C}^{L\times M}$. Further, let the singular values along the diagonal of $\boldsymbol{\Lambda}$ be arranged in descending numerical order. Let λ_i denote the ith diagonal element in $\boldsymbol{\Lambda}$. Substituting the above into (2) and (3),

we get

$$\boldsymbol{W} = \boldsymbol{U}\boldsymbol{\Sigma}\boldsymbol{U}^H, \tag{18}$$

$$\begin{aligned} \mathrm{C}(\boldsymbol{R}) &= \log\det\{\boldsymbol{I}_M + \sigma_x^2\boldsymbol{G}[(\boldsymbol{F}\boldsymbol{R})^H\boldsymbol{W}^{-1}(\boldsymbol{F}\boldsymbol{R})]\boldsymbol{G}^H\} \\ &= \log\det\{\boldsymbol{I}_M + \sigma_x^2\boldsymbol{G}[\boldsymbol{V}\overline{\boldsymbol{\Sigma}}\boldsymbol{V}^H]\boldsymbol{G}^H\}, \end{aligned} \tag{19}$$

where $\boldsymbol{\Sigma}$ and $\overline{\boldsymbol{\Sigma}}$ are diagonal matrices with their ith diagonal terms given by

$$\boldsymbol{\Sigma}(i,i) = \sigma_D^2 + (\sigma_R|\lambda_i|)^2, \tag{20}$$

$$\overline{\boldsymbol{\Sigma}}(i,i) = \frac{|\lambda_i|^2}{\sigma_D^2 + (\sigma_R|\lambda_i|)^2} = \frac{|\lambda_i|^2}{\boldsymbol{\Sigma}(i,i)}. \tag{21}$$

By scaling $\boldsymbol{R}$ to $s\boldsymbol{R}$ and using $\boldsymbol{W}_s$ to denote the resulting noise correlation matrix at the destination (in place of $\boldsymbol{W}$), we find

$$\boldsymbol{W}_s = \sigma_D^2\boldsymbol{I} + (s\sigma_R)^2(\boldsymbol{F}\boldsymbol{R})(\boldsymbol{F}\boldsymbol{R})^H = \boldsymbol{U}\boldsymbol{\Sigma}_s\boldsymbol{U}^H, \tag{22}$$

$$\begin{aligned} \mathrm{C}(s\boldsymbol{R}) &= \log\det\{\boldsymbol{I}_M + \sigma_x^2\boldsymbol{G}[s^2(\boldsymbol{F}\boldsymbol{R})^H\boldsymbol{W}_s^{-1}(\boldsymbol{F}\boldsymbol{R})]\boldsymbol{G}^H\} \\ &= \log\det\{\boldsymbol{I}_M + \sigma_x^2\boldsymbol{G}[\boldsymbol{V}\overline{\boldsymbol{\Sigma}}_s\boldsymbol{V}^H]\boldsymbol{G}^H\}, \end{aligned} \tag{23}$$

where $\boldsymbol{\Sigma}_s$ and $\overline{\boldsymbol{\Sigma}}_s$ are diagonal matrices with their ith diagonal terms given by

$$\boldsymbol{\Sigma}_s(i,i) = \sigma_D^2 + (s\sigma_R|\lambda_i|)^2, \tag{24}$$

$$\overline{\boldsymbol{\Sigma}}_s(i,i) = \frac{s|\lambda_i|^2}{\sigma_D^2 + (s\sigma_R|\lambda_i|)^2} \triangleq a_i\overline{\boldsymbol{\Sigma}}(i,i), \tag{25}$$

$$\tag{26}$$

with a_i defined as

$$a_i = \frac{s^2[\sigma_D^2 + (\sigma_R|\lambda_i|)]^2}{\sigma_D^2 + s^2(\sigma_R^2|\lambda_i|)^2}. \tag{27}$$

Note that $a_i > 1$ and $a_i \le a_j$ for $i \le j$.

From (23) and (25), $\overline{\boldsymbol{\Sigma}}_s$ can be expressed as the sum of two diagonal matrices as

$$\overline{\boldsymbol{\Sigma}}_s = a_1\overline{\boldsymbol{\Sigma}} + \overline{\boldsymbol{\Sigma}}_\Delta, \tag{28}$$

where $\overline{\boldsymbol{\Sigma}}_\Delta$ is some nonnegative diagonal matrix. Then, based on the eigenvalue inequalities concerning the sum of two nonnegative-definite matrices [10, Sec. 6.4], we have

$$\begin{aligned} \mathrm{C}(s\boldsymbol{R}) &\ge \log\det\{\boldsymbol{I}_M + a_1\sigma_x^2\boldsymbol{G}[\boldsymbol{V}\overline{\boldsymbol{\Sigma}}\boldsymbol{V}^H]\boldsymbol{G}^H\} \\ &> \mathrm{C}(\boldsymbol{R}). \end{aligned} \tag{29}$$

Appendix B
Proof of Theorem 2

From (25), as $|s| \to \infty$ the significance of σ_D vanishes, so that $\overline{\boldsymbol{\Sigma}}_s(i,i) \approx \sigma_R^{-2}$ and

$$\mathrm{C}(s\boldsymbol{R}) \approx \log\det[\boldsymbol{I}_M + (\sigma_x/\sigma_R)^2\boldsymbol{G}\boldsymbol{V}\boldsymbol{V}^H\boldsymbol{G}^H] \tag{30}$$

where $\boldsymbol{V}$ is the matrix of right singular vectors of $\boldsymbol{F}\boldsymbol{R}$ as given in (17). To obtain the result, the key is to grasp the eigenvalue structure of $\boldsymbol{G}\boldsymbol{V}\boldsymbol{V}^H\boldsymbol{G}^H$, or equivalently that of $\boldsymbol{G}^H\boldsymbol{G}\boldsymbol{V}\boldsymbol{V}^H$. For this, let $\rho_i(\boldsymbol{M})$ denote the ith largest eigenvalue of a matrix $\boldsymbol{M}$ that has real eigenvalues. We have

$$\begin{aligned} &\rho_1(\boldsymbol{G}^H\boldsymbol{G}) \ge \rho_2(\boldsymbol{G}^H\boldsymbol{G}) \ge \cdots \ge \rho_M(\boldsymbol{G}^H\boldsymbol{G}) > 0, \\ &\rho_i(\boldsymbol{V}\boldsymbol{V}^H) = 1,\ 1 \le i \le M, \\ &\rho_i(\boldsymbol{G}^H\boldsymbol{G}) = \rho_i(\boldsymbol{V}\boldsymbol{V}^H) = 0,\ M+1 \le i \le L. \end{aligned}$$

Therefore, based on the eigenvalue properties concerning matrix products [10, Sec. 6.6], we have

$$\begin{aligned} \rho_i(\boldsymbol{G}^H\boldsymbol{G}\boldsymbol{V}\boldsymbol{V}^H) &\le \rho_i(\boldsymbol{G}^H\boldsymbol{G})\rho_1(\boldsymbol{V}\boldsymbol{V}^H) \\ &= \rho_i(\boldsymbol{G}^H\boldsymbol{G}). \end{aligned} \tag{31}$$

The equality in the first line of the above equation holds if and only if $\boldsymbol{G}$ and $\boldsymbol{V}$ span the same row space, or equivalently, if and only if $\boldsymbol{G}$ and $\boldsymbol{F}\boldsymbol{R}$ span the same row space. In conclusion, as $|s| \to \infty$,

$$\mathrm{C}(s\boldsymbol{R}) \le \log\det[\boldsymbol{I}_M + (\sigma_x/\sigma_R)^2\boldsymbol{G}\boldsymbol{G}^H], \tag{32}$$

where the equality holds if and only if $\boldsymbol{F}\boldsymbol{R}$ and $\boldsymbol{G}$ span the same row space.

References

[1] E. Zeng, S. Zhu, X. Liao, Z. Zhong, and Z. Feng, "On the performance of amplify-and-forward relay systems with limited feedback beamforming," *IEICE Trans. Commun.*, vol. 91, no. 6, pp. 2053–2057, 2008.

[2] X. Tang and Y. Hua, "Optimal design of non-regenerative MIMO wireless relays," *IEEE Trans. Wireless Commun.*, vol. 6, no. 4, pp. 1398–1407, Apr. 2007.

[3] I. Hammerstrom and A. Wittneben, "Power allocation schemes for amplify-and-forward MIMO-OFDM relay links," *IEEE Trans. Wireless Commun.*, vol. 6, no. 8, pp. 2798–2802, 2007.

[4] C. B. Chae, T. Tang, R. W. Heath, Jr., and S. Cho, "MIMO Relaying With Linear Processing for Multiuser Transmission in Fixed Relay Networks," *IEEE Trans. Signal Process.*, vol. 56, no. 2, pp. 727–738, Feb. 2008.

[5] S. Jin, M. R. McKay, C. Zhong, and K. K. Wong, "Ergodic capacity analysis of amplify-and-forward MIMO dual-hop systems," in *IEEE Int. Symp. Info. Theory*, 2008, pp. 1903–1907.

[6] Z. Chen, J. Yuan, and B. Vucetic, "Analysis of transmit antenna selection/maximal-ratio combining in Rayleigh fading channels," *IEEE Trans. Veh. Technol.*, vol. 54, no. 4, pp. 1312–1321, 2005.

[7] A. Gorokhov, D. Gore, and A. Paulraj, "Performance bounds for antenna selection in MIMO systems," in *Conf. Rec., IEEE Int. Conf. Commun.*, vol. 5, 2003, pp. 3021–3025.

[8] ——, "Receive antenna selection for MIMO flat-fading channels: theory and algorithms," *IEEE Inf. Theory*, vol. 49, no. 10, pp. 2687–2696, Oct. 2003.

[9] I. E. Telatar, "Capacity of multi-antenna gaussian channels," *Europ. Trans. Telecommun.*, vol. 10, pp. 585–595, Nov. 1999.

[10] G. A. F. Seber, *A Matrix Handbook for Statisticians*. Wiley-Interscience, 2007.

[11] L. Vandenberghe, S. Boyd, and S. P. Wu, "Determinant maximization with linear matrix inequality constraints," *SIAM J. Matrix Anal. Appl.*, vol. 19, pp. 499–533, 1998.

國科會補助計畫衍生研發成果推廣資料表

日期:2011/10/13

國科會補助計畫	計畫名稱: 子計畫三：合作式多輸出入無線通訊之上行傳收器訊號處理技術研究(2/2)
	計畫主持人: 林大衛
	計畫編號: 99-2219-E-009-010- 學門領域: 接取技術(網通國家型)

無研發成果推廣資料

99 年度專題研究計畫研究成果彙整表

計畫主持人：林大衛	計畫編號：99-2219-E-009-010-
計畫名稱：寬頻合作式無線多輸出入通訊系統--子計畫三：合作式多輸出入無線通訊之上行傳收器訊號處理技術研究(2/2)	

成果項目			量化			單位	備註（質化說明：如數個計畫共同成果、成果列為該期刊之封面故事...等）
			實際已達成數（被接受或已發表）	預期總達成數(含實際已達成數)	本計畫實際貢獻百分比		
國內	論文著作	期刊論文	0	0	100%	篇	
		研究報告/技術報告	0	0	100%		
		研討會論文	0	0	100%		
		專書	0	0	100%		
	專利	申請中件數	1	0	100%	件	
		已獲得件數	0	0	100%		
	技術移轉	件數	0	0	100%	件	
		權利金	0	0	100%	千元	
	參與計畫人力（本國籍）	碩士生	8	0	100%	人次	
		博士生	2	0	100%		
		博士後研究員	0	0	100%		
		專任助理	0	0	100%		
國外	論文著作	期刊論文	1	0	100%	篇	
		研究報告/技術報告	0	0	100%		
		研討會論文	2	0	100%		其中一篇係與本總計畫另一個子計畫之主持人合作之成果。
		專書	0	0	100%	章/本	
	專利	申請中件數	1	0	100%	件	
		已獲得件數	0	0	100%		
	技術移轉	件數	0	0	100%	件	
		權利金	0	0	100%	千元	
	參與計畫人力（外國籍）	碩士生	0	0	100%	人次	
		博士生	0	0	100%		
		博士後研究員	0	0	100%		
		專任助理	0	0	100%		

其他成果 (無法以量化表達之成果如辦理學術活動、獲得獎項、重要國際合作、研究成果國際影響力及其他協助產業技術發展之具體效益事項等，請以文字敘述填列。)	無。

	成果項目	量化	名稱或內容性質簡述
科教處計畫加填項目	測驗工具(含質性與量性)	0	
	課程/模組	0	
	電腦及網路系統或工具	0	
	教材	0	
	舉辦之活動/競賽	0	
	研討會/工作坊	0	
	電子報、網站	0	
	計畫成果推廣之參與（閱聽）人數	0	

國科會補助專題研究計畫成果報告自評表

請就研究內容與原計畫相符程度、達成預期目標情況、研究成果之學術或應用價值（簡要敘述成果所代表之意義、價值、影響或進一步發展之可能性）、是否適合在學術期刊發表或申請專利、主要發現或其他有關價值等，作一綜合評估。

1. 請就研究內容與原計畫相符程度、達成預期目標情況作一綜合評估

■達成目標

□未達成目標（請說明，以 100 字為限）

□實驗失敗

□因故實驗中斷

□其他原因

說明：

2. 研究成果在學術期刊發表或申請專利等情形：

論文：■已發表 □未發表之文稿 □撰寫中 □無

專利：□已獲得 ■申請中 □無

技轉：□已技轉 □洽談中 ■無

其他：（以 100 字為限）

3. 請依學術成就、技術創新、社會影響等方面，評估研究成果之學術或應用價值（簡要敘述成果所代表之意義、價值、影響或進一步發展之可能性）（以 500 字為限）

學術成就及進一步發展之可能：本計畫就下世代行動通訊傳輸訊號處理技術進行研究，獲得若干創新之見，除形成學生學位論文之基礎外，並陸續投稿國際學術會議與期刊中。我們也在基於這些研究成果作進一步之研究，預期可在行動通訊傳輸訊號處理學術方面作出更多貢獻。

技術創新與應用價值等方面：本計畫之研究成果，涵蓋雙向中繼技術、上行測距技術、多輸出入傳收技術、初始下行同步技術之數位訊號處理器軟體實現、通道估計技術之數位訊號處理器軟體實現、等等課題。除可供相關產研界參考外，我們也已本於歷年來在相關領域的研究成果，與國內研發機構進行技術研發與國際標準等方面的合作。此外，我們亦已將部份成果向國內外申請專利。